ADVANCED COMPUTATIONAL MODELING OF WAVE ENERGY CONVERTERS AND FLUID-STRUCTURE INTERACTION: A SMOOTHED PARTICLE HYDRODYNAMICS APPROACH

By
SHAYAN RAMEZANZADEH

Submitted to the Graduate Faculty of Engineering and Natural Sciences
in partial fulfilment of
the requirements for the degree of Doctor of Philosophy

Sabancı University
July 2023

ABSTRACT

ADVANCED COMPUTATIONAL MODELING OF WAVE ENERGY CONVERTERS AND FLUID-STRUCTURE INTERACTION: A SMOOTHED PARTICLE HYDRODYNAMICS APPROACH

SHAYAN RAMEZANZADEH

MANUFACTURING ENGINEERING Ph.D DISSERTATION, JULY 2023

Dissertation Supervisor: Prof. Dr. Mehmet Yildiz

Dissertation Co-Supervisor: Asst. Prof. Dr. Murat Ozbulut

Keywords: Weakly Compressible Smoothed Particle Hydrodynamics; Fluid-Structure Interaction; Free-Surface Hydrodynamics; Wave Energy; Oscillating Wave Energy Converter; Point-Absorber Wave Energy Converter

Computational fluid dynamics (CFD) has emerged as a powerful tool for analyzing and simulating complex fluid flow phenomena in various real-life and industrial applications. This thesis focuses on advancing the computational modeling of wave energy converters (WECs) and fluid-structure interaction (FSI) problems using the smoothed particle hydrodynamics (SPH) method, a mesh-free numerical approach renowned for its ability to address the inherent complexities and non-linearities of such physical processes.

The primary objective of this research is to enhance the capabilities of the SPH method in modeling and simulating three distinct types of energy converters: Oscillating Wave Energy Converters (OWECs), Overtopping-type Wave Energy Converter devices, and Point Absorber Converter systems. By harnessing the accuracy and flexibility of the SPH method, this study aims to achieve a comprehensive understanding of the hydrodynamic behavior of these devices, providing valuable insights into their performance and optimization.

To initiate the investigation, a crucial step involves modeling regular and irregular

waves in a numerical wave flume, serving as the foundation for generating realistic wave conditions for subsequent WEC modeling. By meticulously reproducing wave characteristics, including height, period, and wave orbital velocities, the reliability and fidelity of the numerical simulations are ensured.

Subsequently, the SPH method is employed to model the wave energy converter devices, enabling the precise capture of the intricate interactions between the devices and the waves. Through this modeling approach, a rigorous analysis and evaluation of the hydrodynamic performance and energy conversion efficiency of the converters can be conducted.

Furthermore, this thesis delves into the investigation of fluid-structure interaction (FSI) problems utilizing the SPH method. This entails the modeling and simulation of the dynamic interaction between fluid flows and various structures, accounting for significant factors such as fluid-induced forces and the resulting motion of solid objects. By examining FSI problems, this research aims to deepen the understanding of the behavior and performance of structures operating within dynamic fluid environments.

The research methodology involves the implementation and refinement of the SPH method to ensure the accurate simulation of wave energy converter systems and fluid-structure interaction problems. The credibility and validity of the developed numerical models and simulations will be assessed through rigorous comparisons with experimental data and existing theoretical results documented in the literature.

The outcomes of this research are anticipated to make substantial contributions to the field of computational modeling in wave energy converters and fluid-structure interaction. By leveraging the SPH method, this study will offer valuable insights into the performance and optimization of oscillating wave energy converters, overtopping wave energy converters, and point absorber converter systems. Additionally, the investigation of fluid-structure interaction problems will enhance the understanding of the dynamic behavior and response of structures subjected to fluid flows. Ultimately, this research endeavors to drive advancements in the design and operation of wave energy converters, promoting the sustainable utilization of wave energy resources.

ÖZET

Hesaplamalı akışkanlar dinamiği (CFD), çeşitli gerçek hayat ve endüstriyel uygulamalarda karmaşık akışkan hareketi olaylarını analiz etmek ve simüle etmek için güçlü bir araç olarak ortaya çıkmıştır. Bu tez, dalgalı enerji dönüştürücülerinin (WEC'ler) ve akış-yapı etkileşimi (FSI) sorunlarının hesaplamalı modellemesini geliştirmeye odaklanmaktadır. Bu amaçla, smoothed particle hydrodynamics (SPH) yöntemi kullanılarak, bu fiziksel süreçlerin doğasında yer alan karmaşıklıkları ve doğrusal olmayanlıkları ele alma kabiliyetiyle tanınan bir ağsız sayısal yaklaşım kullanılmaktadır.

Bu araştırmanın temel amacı, SPH yönteminin salınan dalga enerjisi dönüştürücüleri (OWEC'ler), taşma tipi dalga enerjisi dönüştürücü cihazlar ve nokta emici dönüştürücü sistemleri gibi üç farklı enerji dönüştürücüyü modelleme ve simülasyon yeteneklerini geliştirmektir. SPH yönteminin hassasiyeti ve esnekliği kullanılarak, bu çalışma bu cihazların hidrodinamik davranışını kapsamlı bir şekilde anlamayı, performanslarını ve optimizasyonlarını değerlendirmeyi hedeflemektedir.

Araştırmaya başlamak için, sayısal bir dalga kanalında düzenli ve düzensiz dalgaların modellemesi önemli bir adımdır ve ardışık WEC modellemesi için gerçekçi dalga koşullarının oluşturulmasında temel bir rol oynamaktadır. Dalga yüksekliği, periyot ve dalga yörüngesel hızları gibi dalga özelliklerinin dikkatlice yeniden üretilmesiyle, sayısal simülasyonların güvenilirliği ve sadakati sağlanmaktadır.

Daha sonra, SPH yöntemi kullanılarak dalga enerji dönüştürücü cihazlarının modellemesi yapılmakta ve cihazlar ile dalgalar arasındaki karmaşık etkileşimlerin kesin bir şekilde yakalanması sağlanmaktadır. Bu modelleme yaklaşımı sayesinde, dönüştürücülerin hidrodinamik performansı ve enerji dönüşüm verimliliği titizlikle analiz edilebilmektedir.

Ayrıca, bu tez, SPH yöntemini kullanarak akış-yapı etkileşimi (FSI) sorunlarının incelenmesine de odaklanmaktadır. Bu, akışkan akımları ile çeşitli yapılar arasındaki dinamik etkileşimin modellemesi ve simülasyonunu içermektedir. Akışkan kaynaklı kuvvetler ve katı cisimlerin hareketi gibi önemli faktörler dikkate alınmaktadır. FSI sorunlarının incelenmesi, dinamik akışkan ortamlarda çalışan yapıların davranışını ve performansını daha derinlemesine anlamayı hedeflemektedir.

Araştırma yöntemi, dalga enerji dönüştürücü sistemlerinin ve akış-yapı etkileşimi sorunlarının doğru bir şekilde simülasyonunu sağlamak için SPH yönteminin uygulanması ve geliştirilmesini içermektedir. Geliştirilen sayısal modellerin ve simülasyonların güvenilirliği ve geçerliliği, deneysel verilerle ve literatürdeki mevcut teorik sonuçlarla kapsamlı karşılaştırmalar yaparak değerlendirilecektir.

Bu araştırmanın sonuçları, dalga enerji dönüştürücüler ve akış-yapı etkileşimi alanında hesaplamalı modellemeye önemli katkılarda bulunması beklenmektedir.

SPH yönteminden yararlanarak, bu çalışma salınan dalga enerjisi dönüştürücüleri (OWEC'ler), taşma tipi dalga enerjisi dönüştürücü cihazlar ve nokta emici dönüştürücü sistemlerinin performansını ve optimizasyonunu sağlamak için değerli içgörüler sunacaktır. Ayrıca, akış-yapı etkileşimi sorunlarının incelenmesi, akışkan akımlarına maruz kalan yapıların dinamik davranışını ve tepkisini daha iyi anlamamıza yardımcı olacaktır. Sonuç olarak, bu araştırma, dalga enerji dönüştürücülerinin tasarımı ve işletilmesinde ilerlemeler sağlamayı ve dalga enerjisi kaynaklarının sürdürülebilir kullanımını teşvik etmeyi amaçlamaktadır.

ACKNOWLEDGEMENTS

First and foremost, I would like to express my sincere gratitude to Professor Mehmet Yildiz, my supervisor, for warmly welcoming me into his research group and for providing unwavering support, guidance, and constructive criticism throughout this journey. I am truly grateful for the numerous opportunities he has given me, allowing me to explore and cultivate my own research interests and aiding in my growth as a researcher.

I would also like to extend my heartfelt appreciation to Assistant Professor Murat Ozbulut, my co-supervisor, for his invaluable support, profound insights, and countless ideas that have played a pivotal role in shaping the trajectory of my research. I am truly grateful for his unwavering dedication and the invaluable mentorship he has provided throughout this journey.

Furthermore, I would like to acknowledge the exceptional research environment and financial assistance provided by Sabanci University and the SU-IMC team.

I would like to express my gratitude to my friends at Sabanci and the SU-IMC, as well as my family, for their unwavering support and constant motivation.

Lastly, but certainly not least, I want to express my deepest gratitude to my beloved wife for her boundless love, endless patience, and unwavering emotional support.

Dedicated to:
To my father, whose determination is as strong as the mountain,
To my mother, whose heart is as vast as the ocean,
To my endless love and lovely wife, Aida

TABLE OF CONTENTS

LIST OF TABLES ..... **xii**

LIST OF FIGURES ..... **xiii**

1. General Introduction **1**
1.1. Introduction and Statement of Problem 1
1.2. Description of Remaining Chapters 2

2. Methodology **5**
2.1. Governing Equations and SPH Modeling 5
2.1.1. Governing Equations of Motion 5
2.1.2. SPH Discretization through Weakly Compressible Approach 6
2.2. Mathematical Formulas for Modeling and Absorbing Waves 10
2.2.1. Equations for the Moving Boundary Wave-Maker Systems 10
2.2.1.1. Passive Wave Absorbtion 11

3. Modelling of Wave Generation in a Numerical Tank by SPH Method **13**
3.1. Introduction 14
3.2. Determination of Wave Characteristics and Numerical Results 16
3.2.1. Definition of Problem Geometry 17
3.2.2. Results of Regular Wave Simulations 19
3.2.3. Results of Irregular Wave Simulations 26
3.3. Conclusion 29

4. A Preliminary Investigation on the Modelling of Overtopping Wave Energy Converter Systems by SPH Method **31**
4.1. Introduction 31
4.2. Problem definition 32
4.2.1. Overtopping prediction formulations 33
4.3. Results and Discussion 34

4.4. Conclusions 35

5. A Numerical Investigation on the Energy Efficiency Enhancement of Oscillating Water Column Wave Energy Converter Systems ... 36
5.1. Introduction 36
5.2. Problem definition 41
5.2.1. OWC hydrodynamic efficiency 43
5.3. Results and Discussion 45
5.3.1. Validation and Verification Studies for the OWC Simulations . 45
5.3.2. Performance Assessment of Chamber Length and Front Wall Draft Configurations 47
5.3.3. Effect of the Corner Chamfering on the Energy Effeciency 49
5.4. Conclusions 55

6. Comprehensive Numerical Study on the Behavior of Floating Structures under Challenging Ocean Conditions using WCSPH .. 57
6.1. Introduction 57
6.1.1. Modeling of Dynamic Floating Body Motion 60
6.1.2. Equations for Determining the Hydrodynamic Performance of Point-Absorber Wave Energy Converter 63
6.2. Results and Discussion 64
6.2.1. Modelling of Regular Ocean Waves 64
6.2.2. Investigating the Behaviour of Point Absorber Wave Energy Converter in the Presence of Regular Waves 68
6.2.3. Analysis of Rolling Motion for a Floating Box in Calm Water Conditions 72
6.2.4. Investigating the Rolling Motion of a Floating Box in the Presence of Regullar Ocean Waves 78
6.2.5. Investigating the Interaction of Regular Ocean Waves with a Freely Floating Box 82
6.3. Conclusions 86

7. GENERAL CONCLUSIONS 88

BIBLIOGRAPHY 91

LIST OF TABLES

Table 3.1. The comparison of SPH results with expected theoretical wave frequencies (ω_T), wave heights (H_T) and energy densities (E_T). 24
Table 3.2. The problem parameters of irregular wave simulation cases 26

Table 4.1. Overview of the prediction formula with their range of utilization for slope angle and relative crest freeboard [121]. 33

Table 5.1. RMSE comparison between the free surface elevation measured in the experiment and calculated by the SPH simulations. 47
Table 5.2. Obtained EEI values for each OWC geometries and wave periods 48
Table 5.3. OWC geometry variations and measured hydrodynamic efficiency for each of them (Base model, $T = 8s$, $y = 3.0m$, and $w = 3.3m$). 50
Table 5.4. Comparison of EEI values for the base geometry and the best performance geometry configuration (case 3) at each wave period..... 54

Table 6.1. Comparison of RMSE values between the theoretical 2$^{\text{nd}}$ order stokes and SPH simulated free surface elevation. 67
Table 6.2. Comparison of RMSE Values between experimental [126] and SPH simulation results for heave displacement and vertical velocity at a damping coefficient of 240 Ns/m. 69
Table 6.3. Comparison of Average Power and Efficiency for different values of b_{PTO} (Ns/m) 72
Table 6.4. Comparison of RMSE values for experimental [48] and SPH simulation results of the box roll angle during damped rolling oscillation, for dx values of 0.020 m, 0.014 m, and 0.010 m. 74
Table 6.5. Comparison of Roll Motion Dynamics 78
Table 6.6. Selected wave scenarios. 78

LIST OF FIGURES

Figure 3.1. Wave conditions on [56] abacus 16

Figure 3.2. The schematic view of wave tank geometries for (a) flap (b) piston type wave-makers. 18

Figure 3.3. Comparison of wave profiles for the test case $\lambda = 1.00m$ and $H/\lambda = 1/20$ at a fully developed wave regime. 20

Figure 3.4. SPH time series of the wave elevations at $x = 2\lambda$ (a) and its frequency domain representation (b) for $\lambda = 1.00m$ and $H/\lambda = 1/20$. 21

Figure 3.5. Time series (left) and FFT analyses (right) for the wavelengths 0.25 [m], 0.50 [m], and 1.00 [m]. 22

Figure 3.6. Time series of the wave elevations (left) and their frequency domain representation right at $\lambda = 0.50[m]$ test case with variable wave steepness ratios. 25

Figure 3.7. Time series of the wave elevations (Theoretical: Airy wave theory) for the first (a) and second (b) test cases in Table 3.2. 27

Figure 3.8. Frequency domain analyses of the wave energies (Theoretical: Airy wave theory) for the first (a) and second (b) test cases in Table 3.2. 28

Figure 3.9. Time series of the wave elevations (Theoretical: Airy wave theory) for the third (a) and fourth (b) test cases in Table 3.2. 28

Figure 3.10. Frequency domain analyses of the wave energies (Theoretical: Airy wave theory) for the third (a) and fourth (b) test cases in Table 3.2. 29

Figure 4.1. Schematic representation of the computational domain for the OWEC devices. 32

Figure 4.2. The comparison of SPH and Prediction formula average wave overtopping flow rate results in different slope angles. 35

Figure 5.1. Wave characteristics of simulations with ($d = 10m$ and $H = 2.5m$) for different wave periods on Le Méhauté [57] abacus. 41

Figure 5.2. Schematic representation of the computational domain for the validation case wave tank (top) and the baseline OWC devices (bottom). 42
Figure 5.3. Schematic representation of the chamber region details utilized in the OWC geometry modification test cases (the blue color area represents the calculation region of vorticity magnitude). 42
Figure 5.4. Comparison of free surface elevation time series of the present SPH results with those of time-domain and experimental findings of [47]. 46
Figure 5.5. Comparison of SPH numerical and theoretical (2^{nd} order Stokes) wave surface elevation and orbital velocities with ($T = 10s$, $H = 2.4m$ and $d = 10m$) at $x = 55m$ and $z = -3m$. 47
Figure 5.6. Time series of water surface elevation (top), velocity (center), and air pressure drop (bottom) within the OWC chamber for a propagating wave with $T = 8s$. 49
Figure 5.7. Comparison between efficiency and amount of vorticity recorded within the OWC chamber for different sloping wall configurations ($T = 8s$, $y = 3.0m$, and $w = 3.3m$). 51
Figure 5.8. Instantaneous vorticity field and velocity vector representations of test cases with maximum (case 3, left) and minimum (case 4, right) EEI values for a full period of motion. 52
Figure 5.9. Time series of free-surface elevation (top), velocity (center), and air pressure drop (bottom) within the OWC chamber for different chamfer configurations ($T = 8s$, $y = 3.0m$ and, $w = 3.3m$). 53
Figure 5.10. Time series of free-surface elevation (top), velocity (center), and air pressure drop (bottom) inside the OWC chamber for the best performance geometry configuration (case 3) at each wave period..... 54

Figure 6.1. Schematic visualization of the computational domain for the verification model. 65
Figure 6.2. Comparison of numerical and theoretical (2^{nd} order Stokes) wave surface elevation and orbital velocities for SPH at $T = 1.5$ s, $H = 0.16$ m, and $d = 1.1$ m, at location $x = 3.4$ m and depth $z = -0.2$ m. 67
Figure 6.3. Schematic visualization of the computational domain for the point-absorber wave energy converter device. 68
Figure 6.4. Comparison between experimental [126] and numerical time-series of heave displacement and vertical velocity for the point-absorber device with a PTO damping coefficient of 240 Ns/m. 69

Figure 6.5. Comparison of experimental [126] and numerical time-series of heave displacement for the point-absorber with PTO damping coefficients of 0 Ns/m, 240 Ns/m, and 1100 Ns/m. 70
Figure 6.6. Comparison of numerical and experimental [126] time-series of vertical velocity for the point-absorber device with PTO damping coefficients of 0 Ns/m, 240 Ns/m, and 1100 Ns/m. 71
Figure 6.7. Schematic representation of the numerical tank for damped roll motion. 73
Figure 6.8. Comparison of the time history of box roll angle during damped rolling oscillation for dx values of 0.020 m, 0.014 m, and 0.010 m with experimental results from Jung et al. [48]. 74
Figure 6.9. Spectrum analysis of the roll free decay test. 75
Figure 6.10. Rolling extinction curve for dx=0.010 m. 77
Figure 6.11. Sketch of numerical wave tank for damped roll motion. 79
Figure 6.12. Comparison between experimental measurements [48] and SPH simulations for the free surface elevation and roll angle of the structure. The comparison is conducted for two sets of wave conditions: a) $T = 0.93$ s, $H = 0.027$ m and b) $T = 1.2$ s, $H = 0.060$ m. 80
Figure 6.13. Magnification factors (RAOs) for roll motion. 81
Figure 6.14. Spectrum of Roll motion for different wave conditions. 82
Figure 6.15. Numerical setup for the experiment by Ren et al. [96] for modeling a freely floating box. 83
Figure 6.16. Comparison between experimental and numerical time-series of heave (a) and surge (b) motion of a freely floating box, as well as the pitch angles (c) under the influence of regular waves. 85
Figure 6.17. Centroid trajectories of the floating box. 86

1. General Introduction

1.1 Introduction and Statement of Problem

Computational fluid dynamics (CFD) has emerged as a powerful tool for analyzing and simulating complex fluid flow phenomena in various real-life and industrial applications. To address the inherent complexities and non-linearities of these physical processes, different numerical methods, including mesh-based and mesh-free approaches, have been developed. In this thesis, our focus is on the smoothed particle hydrodynamics (SPH) method, a specific mesh-free technique, to tackle the challenges associated with wave energy converters (WECs) and fluid-structure interaction (FSI) problems.

The main objective of this research is to advance the computational modeling of WECs and FSI using the SPH method. Specifically, we aim to model and simulate three types of energy converters: Oscillating Wave Energy Converters (OWECs), Overtopping-type Wave Energy Converter devices, and Point Absorber Converter systems. By employing the SPH method, we can accurately capture the hydrodynamic behavior of these devices and gain valuable insights into their performance.

To commence our investigation, we will first focus on modeling regular and irregular waves in a numerical wave flume. This step is crucial for generating realistic wave conditions that will serve as inputs for the subsequent modeling of the WEC devices. By accurately reproducing wave characteristics, such as height, period, and wave orbital velocities, we can ensure the reliability and accuracy of our numerical simulations.

Subsequently, we will proceed with the modeling of the aforementioned wave energy converter devices using the SPH method. By capturing the complex interactions between the devices and the waves, we can analyze their hydrodynamic performance and assess their energy conversion efficiency.

Additionally, this thesis addresses the investigation of fluid-structure interaction (FSI) problems using the SPH method. We will model and simulate the dynamic interaction between fluid flows and various structures, taking into account factors such as fluid-induced forces and solid object motions. Through the analysis of FSI problems, we aim to deepen our understanding of the behavior and performance of structures in dynamic fluid environments.

The research methodology involves the implementation and refinement of the SPH method to accurately simulate wave energy converter systems and fluid-structure interaction problems. We will validate our numerical models and simulations by comparing them against experimental data and existing theoretical results reported in the literature.

The outcomes of this research will contribute to the advancement of computational modeling in the field of wave energy converters and fluid-structure interaction. By utilizing the SPH method, we aim to provide valuable insights into the performance and optimization of oscillating wave energy converters, overtopping wave energy converters, and point absorber converter systems. Moreover, through the investigation of fluid-structure interaction problems, we seek to enhance our understanding of the dynamic behavior and response of structures subjected to fluid flows.

In summary, this thesis focuses on the advanced computational modeling of wave energy converters and fluid-structure interaction using the smoothed particle hydrodynamics (SPH) method. By modeling regular and irregular waves and subsequently simulating various wave energy converter devices and fluid-structure interaction problems, we aim to contribute to the design, optimization, and understanding of these complex systems. Ultimately, this research strives to advance the utilization of wave energy as a sustainable and renewable energy source while enhancing our knowledge of fluid-structure interaction in dynamic fluid environments.

1.2 Description of Remaining Chapters

Chapter 2 provides a comprehensive description of the methodology employed in this thesis, focusing on the governing equations and SPH modeling formulations. It presents the mathematical formulas utilized for modeling and absorbing waves, ensuring an accurate representation of wave characteristics. Through a detailed exploration of these subjects, Chapter 2 establishes the foundation for the subsequent analyses and simulations conducted in the thesis. The overall methodology of this study is detailed in [90, 83, 91], which is presented in Chapter 2 of the dissertation.

Chapter 3 of the study focuses on the utilization of the SPH technique to model a numerical wave tank. By implementing a moving boundary at the tank's inlet and incorporating a dissipative beach for natural damping, both regular and irregular waves are generated. The chapter examines various test cases involving regular waves, which unveil the nonlinear behavior of the free surface, validated through FFT analyses. Comparisons are made between the SPH results and linear theory expectations. To further validate the SPH scheme, the JONSWAP irregular wave spectrum is employed, showcasing the scheme's robustness and accuracy in capturing nonlinear characteristics, including wave-breaking phenomena. The results of this study were published as part of the research described in this thesis (Chapter 3), by Ozbulut et al. [83].

In Chapter 4 of the thesis, the numerical performance of the proposed Smoothed Particle Hydrodynamics (SPH) scheme is assessed for predicting the average overtopping rate of an Overtopping Wave Energy Converter (OWEC) device with varying slope angles. The study involves computing the non-dimensional average wave overtopping flow rate for a range of slope angles from 25° to 60° using two different particle resolutions within the flow domain. The obtained numerical results are then compared with predictions obtained from existing formulas, and the outcomes of this comparative analysis are presented in the chapter.

Chapter 5 of the PhD thesis focuses on investigating the effects of geometry on the performance of OWC-type wave energy converter systems. A two-step geometry modification procedure is employed to enhance energy efficiency. The study validates the accuracy of free-surface elevation and orbital velocity time histories and constructs a simulation matrix to evaluate different geometrical design parameters. The optimized geometry is further improved by chamfering the back wall of the OWC chamber. The analysis establishes a relationship between the time-averaged vorticity within the chamber and energy efficiency. These objectives are achieved and discussed in the research conducted by Ramezanzadeh et al. [91], as part of the content covered in Chapter 5 of this thesis.

Chapter 6 of this PhD thesis presents a comprehensive study utilizing SPH simulations to analyze the behavior of floating structures under specific wave conditions. The chapter consists of five key sub-steps that have been successfully accomplished. The reliability and accuracy of the SPH model are extensively validated through comparisons with experimental and theoretical data, affirming the robustness of the findings. The sub-steps include ensuring accurate wave characteristics, validating the modeling of rigid body motion for a point-absorber wave energy converter, examining the free roll motion of a rectangular floating body, simulating the roll motion of a fixed floating structure under various wave systems, and thoroughly examining the free body motion of a floating structure. This study contributes to understanding the dynamics of floating structures and their response to wave excitation, demonstrating the effectiveness of the SPH approach in accurately representing their behavior.

Finally, Chapter 7 provides a concise summary of the main findings and concludes with insightful remarks.

2. Methodology

This chapter presents a thorough explanation of the methodology used in this thesis, centering on the governing equations and SPH modeling formulations. It also covers the mathematical formulas employed for wave modeling and absorption. By extensively exploring these topics, Chapter 2 establishes the groundwork for the subsequent analyses and simulations carried out in the thesis.

2.1 Governing Equations and SPH Modeling

2.1.1 Governing Equations of Motion

The equations of continuity and conservation of linear momentum are used in this study to model the motion of a barotropic and isothermal fluid domain.

$$\frac{D\rho}{Dt} = -\rho\nabla\cdot\mathbf{u}, \tag{2.1}$$

$$\rho\frac{D\mathbf{u}}{Dt} = -\nabla p + \mu\nabla^2\mathbf{u} + \rho\mathbf{g}. \tag{2.2}$$

where $\frac{D}{Dt}$ operator indicates the material time derivative indicating the change in physical property of the in time. The particle velocity is represented by $\mathbf{u}$, its density is denoted by ρ, and its pressure is represented by p. The equation also includes the dynamic viscosity of the material as μ and gravitational acceleration as $\mathbf{g}$.

To discretize the governing equations, the WCSPH method [76] is used, which is a well-known technique for modeling hydrodynamic phenomena involving free surfaces [98, 122, 23, 69]. To close the equation system, the WCSPH method employs an equation of state that relates density and pressure variations:

$$p_{\mathbf{i}} = \frac{\rho_0 c_0^2}{\gamma}\left[\left(\frac{\rho_{\mathbf{i}}}{\rho_0}\right)^{\gamma} - 1\right]. \tag{2.3}$$

In this study, the reference speed of sound, c_0, is chosen such that the Mach number is kept far below 0.1, thereby ensuring that density variations are limited to less than 1% [75]. The reference density for water is set to 1000 kg/m^3. The specific heat ratio of water is taken as 7. To ensure the mentioned density variation limitations and provide a standard approach for all cases that involve wave generation, the value of c_0 is set 25 times the maximum wave group velocity. This choice of c_0 not only ensures that the incompressibility condition is satisfied, but it also minimizes any potential leads to admissible levels of computational costs. Specifically, assigning a physical value to the speed of sound in water may result in an undesirably small time step values, which would significantly increase the wall-time duration of the simulations.

2.1.2 SPH Discretization through Weakly Compressible Approach

The SPH method models the fluid domain as an assembly of individual free particles, each containing data on properties like density, velocity, and pressure. This technique is founded on the integral representation of a function, approximated through the use of particle distributions [58]. For a specific particle, represented by $\mathbf{i}$, the values of a field variable, either a scalar $f_{\mathbf{i}}$ or a vector $f_{\mathbf{i}}^s$, are calculated through the interpolation of neighboring particle values, denoted as $f_{\mathbf{j}}$ or $f_{\mathbf{j}}^s$. This article employs a mixed notation that incorporates both direct and index notations for representing vector or tensor fields. Direct notation utilizes bold lowercase letters for vectors and bold uppercase letters for tensor fields, while index notation uses italic Latin indices to indicate components, which are always superscripted unless otherwise specified. The Einstein summation convention is applied, signifying that repeated indices imply summation. The SPH method determines the value of any field function through the subsequent process:

$$f_{\mathbf{i}}^{s} = \sum_{\mathbf{j}=1}^{N} V_{\mathbf{j}} f_{\mathbf{j}}^{s} W_{\mathbf{ij}}, \tag{2.4}$$

where a piecewise quintic spline kernel function is employed in the simulations of this study:

$$W_{\mathbf{ij}} = \alpha_d \begin{cases} (3-q)^5 - 6(2-q)^5 + 15(1-q)^5, & 0 \leq q < 1, \\ (3-q)^5 - 6(2-q)^5, & 1 \leq q < 2, \\ (3-q)^5, & 2 \leq q < 3, \\ 0, & 3 \leq q, \end{cases} \tag{2.5}$$

In this representation, the indices $\mathbf{i}$ and $\mathbf{j}$ are used to denote individual particles and N represents the total count of neighboring particles associated with particle $\mathbf{i}$. The kernel function relies on the dimensionless parameter $q = ||\mathbf{r}_{\mathbf{i}} - \mathbf{r}_{\mathbf{j}}||^2/h$, where h represents the smoothing length set to 1.33 times the initial particle distance (δx). The coefficient α_d, which is dependent on the dimensions of the problem domain, is calculated as $7/(478\pi h^2)$ for two-dimensional domains. Additionally, the particle volume, denoted as $V_{\mathbf{j}}$, is computed as $V_{\mathbf{j}} = 1/\sum_{\mathbf{j}=1}^{N} W_{\mathbf{ij}}$.

In order to improve the accuracy of gradient and divergence operations for scalar and vector-valued field variables, a corrective SPH (CSPH) formulation [55, 103] is incorporated into the numerical scheme employed as follows:

$$\frac{\partial f_{\mathbf{i}}^{s}}{\partial x_{\mathbf{i}}^{k}} \alpha_{\mathbf{i}}^{kl} = \sum_{\mathbf{j}=1}^{N} V_{\mathbf{j}} \left(f_{\mathbf{j}}^{s} - f_{\mathbf{i}}^{s} \right) \frac{\partial W_{\mathbf{ij}}}{\partial x_{\mathbf{i}}^{l}}, \tag{2.6}$$

$$\frac{\partial}{\partial x_{\mathbf{i}}^{k}} \left(\frac{\partial f_{\mathbf{i}}^{s}}{\partial x_{\mathbf{i}}^{k}} \right) \alpha_{\mathbf{i}}^{sl} = 8 \sum_{\mathbf{j}=1}^{N} V_{\mathbf{j}} \left(f_{\mathbf{i}}^{s} - f_{\mathbf{j}}^{s} \right) \frac{r_{\mathbf{ij}}^{s}}{r_{\mathbf{ij}}^{2}} \frac{\partial W_{\mathbf{ij}}}{\partial x_{\mathbf{i}}^{l}}, \tag{2.7}$$

$$\alpha_{\mathbf{i}}^{sl} = \sum_{\mathbf{j}=1}^{N} r_{\mathbf{ji}}^{s} V_{\mathbf{j}} \frac{\partial W_{\mathbf{ij}}}{\partial x_{\mathbf{i}}^{l}}. \tag{2.8}$$

In Equation 2.8, the second-rank correction tensor $\alpha_{\mathbf{i}}^{sl}$ plays a crucial role in avoiding inaccuracies like particle clustering and truncated support regions near boundaries.

By denoting the inverse of $\alpha_{\mathbf{i}}^{sl}$ as $B_{\mathbf{i}}^{pl}$, and multiplying both sides of Equation 2.8 by $B_{\mathbf{i}}^{pl}$ allows us to find the gradient correction of the kernel matrix. This term can be expressed as $B_{\mathbf{i}}^{pl}\partial W_{\mathbf{ij}}/\partial x_{\mathbf{i}}^{l}$, or in direct notation, $\mathbf{B_i} \cdot \nabla_{\mathbf{i}} W_{\mathbf{ij}}$.

By incorporating these CSPH treatments into the equations, the governing equations can be discretization as given below:

$$\frac{D\rho_{\mathbf{i}}}{Dt} = \rho_{\mathbf{i}} \sum_{\mathbf{j}=1}^{N} V_{\mathbf{j}} \left(\mathbf{u_i} - \mathbf{u_j}\right) \cdot \left(\mathbf{B_i} \cdot \nabla_{\mathbf{i}} W_{\mathbf{ij}}\right), \tag{2.9}$$

$$\begin{gathered} \frac{D\mathbf{u_i}}{Dt} = -\rho_{\mathbf{i}} \sum_{\mathbf{j}=1}^{N} V_{\mathbf{j}} \left(\frac{p_{\mathbf{i}}}{\rho_{\mathbf{i}}^2} + \frac{p_{\mathbf{j}}}{\rho_{\mathbf{j}}^2}\right) (\mathbf{B_i} \cdot \nabla_{\mathbf{i}} W_{\mathbf{ij}}) + \\ K\nu \frac{\rho_0}{\rho_{\mathbf{i}}} \sum_{\mathbf{j}=1}^{N} V_{\mathbf{j}} \frac{\left(\mathbf{u_i} - \mathbf{u_j}\right) \cdot \left(\mathbf{r_i} - \mathbf{r_j}\right)}{\left\|\mathbf{r_i} - \mathbf{r_j}\right\|^2} (\mathbf{B_i} \cdot \nabla_{\mathbf{i}} W_{\mathbf{ij}}) + \mathbf{g_i}, \end{gathered} \tag{2.10}$$

In Eq.2.10, $\nabla_{\mathbf{i}}$ represents the differentiation concerning the location of particle $\mathbf{i}$. The constant K in the equation is equal to $2(n+2)$, where n is the dimension of the problem domain as specified in [13]. The kinematic viscosity of water, ν, is taken as $10^{-6}[\mathrm{m}^2/\mathrm{s}]$.

In the weakly compressible SPH method, the calculation of accurate density values is crucial as the pressure values are dependent on the density values through the equation of state. Any small inaccuracies in the density calculation may result in significant fluctuations in the pressure field, reducing the overall accuracy of the numerical results [84]. To mitigate these problems, this study incorporates the density smoothing treatment that is commonly used in SPH literature [61, 94]. This smoothing treatment aims to eliminate the adverse effects of oscillations in the pressure field during the evolution of fluid flow. The corrected density, denoted as $\widehat{\rho}_{\mathbf{i}}$, is calculated by interpolating the density values of nearby particles:

$$\widehat{\rho}_{\mathbf{i}} = \rho_{\mathbf{i}} - \frac{\sum_{\mathbf{j}=1}^{N} \left(\rho_{\mathbf{i}} - \rho_{\mathbf{j}}\right) W_{\mathbf{ij}}}{\sum_{\mathbf{j}=1}^{N} W_{\mathbf{ij}}}, \tag{2.11}$$

As a final numerical treatment, this work utilizes a combination of the Velocity-Variance based Free Surface (VFS) and Artificial Particle Displacement (APD) approaches in the simulations. The VFS method is used exclusively for the free surface particles to maintain a uniform velocity and reduce excessive scattering on the free surface. Free surface particles are identified as those having a neighboring particle count that is less than 65% of the average number of neighboring particles in the problem domain. The velocities of the free surface particles are computed using a weighted average of their velocities and those of their neighboring particles. This helps to ensure a smooth transition between the free surface and the interior of the fluid. The velocities of the particles at the free surface are determined using the following method:

$$\delta \mathbf{u_i} = \frac{\sum_{\mathbf{j}=1}^{N}\left(\mathbf{u_i} - \mathbf{u_j}\right) W_{\mathbf{ij}}}{\sum_{\mathbf{j}=1}^{N} W_{\mathbf{ij}}}, \qquad \widehat{\mathbf{u_i}} = \mathbf{u_i} - \epsilon \delta \mathbf{u_i}, \tag{2.12}$$

The corrected particle velocity is denoted by $\hat{\mathbf{u}}_\mathbf{i}$, and the dimensionless constant ϵ is used to obtain the corrected velocity. Our previous studies [83, 90, 84] have suggested that a value of 0.05-0.1 times the initial particle distance (δx) is appropriate for ϵ parameter. Therefore, we use $0.075\delta x$ for all simulations of this study. On the other hand, the APD algorithm is employed in fully populated regions of the fluid domain (where the number of neighboring particles are higher than 65% of the average number of neighboring particles in the problem domain) to improve the accuracy of the interpolation process through providing more uniform and homogeneous distribution of particles during the flow evolution. The formulation of the APD algorithm is described as follows [103]

$$\delta \mathbf{r_i} = \sum_{\mathbf{j}=1}^{N} \frac{\mathbf{r_{ij}}}{\mathbf{r_{ij}^3}} r_\mathbf{0}{}^2 u_v \Delta t, \qquad r_\mathbf{0} = \frac{1}{N}\sum_{\mathbf{j}=1}^{N} \mathbf{r_{ij}}\ , \quad u_v = |\delta u_\mathbf{i}|, \qquad \widehat{\mathbf{r_i}} = \mathbf{r_i} + \delta \mathbf{r_i}, \tag{2.13}$$

The wall boundary conditions are enforced through utilizing four layers of solid particles having the velocity of associated boundary. The SPH approach inherently captures the kinematic and dynamic free-surface boundary conditions without the need for additional treatments.

The process of time integration is performed using a predictor-corrector approach, which was elaborated thoroughly in our prior research [86]. The size of the time step is established by satisfying the Courant-Friedrichs-Lewy (CFL) criterion expressed as follows:

$$\Delta t = C_{CFL} \frac{h}{c_0 + c_w}. \tag{2.14}$$

In all simulations of the present work, the CFL number is set to 0.4, where c_w represents the celerity of the generated wave system [83], where applicable.

2.2 Mathematical Formulas for Modeling and Absorbing Waves

2.2.1 Equations for the Moving Boundary Wave-Maker Systems

In the regular wave simulations of the present study, a flap-type wave-maker is utilized where the relationship between the stroke of the flap (s), and tank depth (d) and wave amplitude ($\xi_a = H/2$) is obtained from the linearized theory of [43]:

$$s = \frac{\xi_a kd[\sinh(kd)\cosh(kd) + kd]}{2[kd\sinh(kd) - \cosh(kd) + 1]\sinh(kd)}, \quad \theta_0 = \arctan\frac{s}{d} \tag{2.15}$$

where k is the wave number calculated as $2\pi/\lambda$. To prevent the instantaneous loads at the initial movement of the flap, a gradually increasing motion has been defined as follows:

$$\theta(t) = \theta_0\cos(\omega t), \quad x(t) = x_0 + z_0\sin[\theta(t)]\tanh(\omega t) \tag{2.16}$$

In equation 2.16 ω represents the angular wave frequency. The wavemaker particles' initial positions are denoted by z_0 and x_0. The alterations in their vertical positions are deemed negligible and, as a result, are not modified.

The irregular wave systems can be considered as a linear superposition of a series of linear sinusoidal waves with arbitrary phase angles which is called Airy wave theory. The superposition of a series of linear wave components gives the irregular wave system:

$$\zeta_t(x,t) = \sum_{i=1}^{n}\frac{H_i}{2}\cos(k_i x - \omega_i t + \epsilon_i) \tag{2.17}$$

where k_i and ω_i are the wave number and circular frequency of the i^th wave, respectively. The algorithm used for irregular wave generation simulations starts by decomposing the intended wave energy spectrum into n equal components within the frequency domain. Amplitude of each wave component is obtained from the spectrum as:

$$\frac{H_i}{2} = \sqrt{2S_\zeta(f_i)\triangle f} \tag{2.18}$$

where $S_\zeta(f_i)$ denotes the wave energy spectrum as a function of frequency and $\triangle f$ is the differential frequency interval. The full-stroke of the wave-maker (given in (2.19) and (2.20) as $s_i = 2s$) in terms of the characteristics of the generated waves is obtained by [21] - following Biesel transfer function - and by [5] for flap and piston type paddles, respectively:

$$\frac{H_i}{s_i} = \frac{4\sinh(k_i d)}{k_i d}\frac{k_i d\sinh(k_i d) - \cosh(k_i d) + 1}{\sinh(2k_i d) + 2k_i d} \tag{2.19}$$

$$\frac{H_i}{s_i} = \frac{2\sinh^2(k_i d)}{\sinh(k_i d)\cosh(k_i d) + k_i d} \tag{2.20}$$

The time series of the wave-maker displacements for the flap and piston type moving boundaries which can also be derived from Eq. 2.19 and 2.20 are given as, respectively:

$$x(t) = \sum_{i=1}^{n} \frac{H_i k_i d[\sinh(2k_i d) + 2k_i d]}{8\sinh(k_i d)[k_i d\sinh(k_i d) - \cosh(k_i d) + 1]} \sin(\omega_i t + \epsilon_i) \tag{2.21}$$

$$x(t) = \sum_{i=1}^{n} \frac{H_i[\sinh(k_i d)\cosh(k_i d) + k_i d]}{4\sinh^2(k_i d)} \sin(\omega_i t + \epsilon_i) \tag{2.22}$$

where ϵ_i is the primary phase which is a random number between 0 and 2π.

2.2.1.1 Passive Wave Absorbtion

To fade out the energy of the generated waves and prevent reflected waves, a numerical damping is applied at the rear part of the numerical wave tank. This damping mechanism gradually reduces the velocity of a fluid particle within the damping zone, starting from its initial velocity $\mathbf{u_{i,0}}$ and reaching to its final velocity $\mathbf{u_i}$ using a quadratic decay function $f_r(x_\mathbf{i}, \Delta t)$, as described in Altomare et al. [7]:

$$\mathbf{u_{i,d}} = \mathbf{u_{i,0}} \cdot f_r(x_\mathbf{i}, \Delta t), \tag{2.23}$$

$$f_r(x_\mathbf{i}, \Delta t) = 1 - \Delta t \cdot \beta \cdot \left(\frac{x_\mathbf{i} - x_0}{x_1 - x_0} \right)^2, \tag{2.24}$$

where, $\mathbf{u_{i,d}}$ is the dampened velocity and ($\mathbf{u_{i,0}}$) is the current time step velocity calculated through governing equations. x_0 and x_1 denote the starting and ending points of the damping zone along the x-axis, respectively. The coefficient β, is fixed at $\beta = 10$ for all simulations [7].

3. Modelling of Wave Generation in a Numerical Tank by SPH Method

There have been many mathematical and physical modelling strategies to represent a numerical wave tank that can generate the desired wave spectrums. Presently, one of the recent methodologies that have certain intrinsic capabilities for the investigation of free-surface hydrodynamic problems, namely, Smoothed-Particle-Hydrodynamics (SPH) technique has been utilized for the modelling of a numerical wave tank. The Navier-Stokes and continuity equations are utilized for governing the fluid motion through Weakly Compressible SPH (WCSPH) approach which couples pressure and density by an equation of state. As one of the major numerical treatments; kernel gradient normalization is included into the present SPH method together with the numerical treatments, namely, well-known density smoothing algorithm, hybrid velocity variance-based free surface (VFS) and artificial particle displacement (APD) algorithms. The generation of regular and irregular waves is performed by a moving boundary at the inlet where natural damping is targeted by utilizing a dissipative beach at the end of numerical wave tank. A wide range of test cases in terms of wave-lengths and steepness ratios have been investigated for the regular wave simulations. Although the wave-maker is forced linearly to oscillate sinusoidally at the inlet of the tank, due to the relatively high wave steepness ratios applied, the non-linear character of the free-surface has been clearly observed with the performed Fast Fourier Transform analyses. Wave energy densities of the SPH results have also been compared with the linear theory expectations per unit wave-length. To scrutinize the conditions for the wave-breaking inception, three additional wave steepness values have been simulated at a single wave-length value. As a further examination of the proposed SPH scheme, JONSWAP irregular wave spectrum has been utilized with both flap and piston type moving boundaries. In the light of performed simulations, the proposed SPH numerical scheme can provide robust and consistent results while generating regular and irregular wave systems in deep water conditions. Furthermore, it is observed that it has the capability of capturing the non-linear characteristics of generated waves with high sensitivity, including the wave-breaking phenomenon.

3.1 Introduction

Theoretical treatments, for a long time, and numerical solutions, recently, for the wave-maker problem have played a vital role in grasping the physical facts in wave generation technologies from hydrodynamics point of view as well as from control engineering's view. Even if the wave-maker is forced linearly to oscillate sinusoidally, the non-linear nature of the medium generates inherently higher-harmonics, preferred to be unmasked to have sound experimental comparisons. The present study, en route to establishing a numerical tank by Smoothed Particle Hydrodynamics (SPH), investigates the nonlinearities in the wave system generated by a flap-type wave-maker.

Starting with [39] followed by [12]'s analysis which was extended by [43] to include both the inertial and damping terms in the pressure, linear wave-maker theories have already reached a certain maturity. The same can be said true for the second-order theories, essentially owing to the works of [30] - a comprehensive study based on Lagrangian description, and of [42] with Eulerian description. Meantime, [117], together with a linear theory, provided also experimental data for a piston-type wave-maker. Among control-related studies; [101]'s work, by employing Stokes' perturbation series through the second-order, presents a full second-order theory, which includes super-harmonics and sub-harmonics in irregular waves as well, supported by experimental data for regular and irregular waves generated by piston-type wave-maker. The need for suppressing second-order free waves due to the second-order wave potential concerns rather control people who take them as spurious signals in controlling the behavior of wave-makers to have a homogeneous and permanent wave field ([70, 112]).

SPH, on the other hand, as a mesh-free numerical method based on a Lagrangian description is capable of modelling the flows with large deformations. The method indeed introduced simultaneously by [74] and [65], and initial studies on the investigation of free-surface hydrodynamics problems by SPH technique goes back to mid-90s [73]. Recently and gradually, SPH is becoming an effective computational tool in analyzing challenging free-surface problems ([113, 41]) including the modelling of non-linear and irregular wave generation ([60, 8, 123]).

In modelling the wave-makers numerically, researchers try to classify the wave generation techniques in various ways. The first group of techniques comprises the representation of wave generation physically as in a towing tank (moving boundary technique) and as a second to the former; a pure numerical approach (source function and other techniques) which are discussed in detail in [123], who employed a Weakly Compressible SPH (WCSPH) scheme to model non-linear wave motion with the inclusion of Smagorinsky approach for the determination of turbulence eddy viscosity. Smagorinsky model has been stated as having a minor contribution to the modelling of wave break occurrence in shallow water regions of the problem domain ([111]). Their WCSPH scheme involves a diffusion term in continuity equation adopted from [72] to prevent spurious numerical noise arise due to the explicit solution of the fluid pressure by the equation of state. As for the tank geometry and wave generation system, they have utilized two sponge layers at the ends of the channel to absorb unwanted reflected waves where a numerical momentum source term is utilized for the wave-maker algorithm.

[8] mostly focused on the passive and active absorption techniques while adopting the WCSPH method in their analyses depending on an open source code which allows only the implementation of piston-type wave-maker according to the authors. Their explanations on the techniques and algorithms employed in SPH modelling are limited and it is understood from their previous works [5] and [18], that usual basic techniques are employed such as quintic kernel, artificial viscosity in momentum equation, density correction and XSPH velocity variant algorithm.

The present study, as a subsequent treatment of wave generation problem, takes into account a flap-type wave-maker with a special attention to the implementation of SPH techniques developed and/or adapted recently by the authors. There are a plenty of approaches on the determination of pressure like Incompressible SPH (ISPH) as recently reviewed by [68] which determine pressure through solving Poisson's equation and recently introduced Augmented Lagrangian SPH technique by [29] in the SPH literature. WCSPH approach, which is commonly employed while modeling free-surface flows ([16, 41]), is used for the calculation of pressure where density is coupled with pressure through an equation of state. As one of the major numerical treatment; kernel gradient normalization defined by [93] is included into the present SPH method together with the numerical treatments, namely, well-known density smoothing algorithm, hybrid velocity variance based free surface (VFS) and artificial particle displacement (APD) algorithms which were successfully implemented for the modelling of violent sloshing motion ([85]). The details of numerical approaches are given and the results of regular and irregular wave generation with their non-linear characteristics are presented in the paper. The results show the robustness of the SPH procedure presented here.

3.2 Determination of Wave Characteristics and Numerical Results

The present study aims to model wave generation in a numerical tank for deep water conditions. When considering the number of particles distributed over the problem domain, there may occur limitations due to the drastic computational cost to capture the wave profiles on the free-surface. Within this context, the determination of wave steepness ratio then becomes a crucial issue that directly affects the number of particles per wave height; which in turn affects the accuracy of the wave elevations obtained. Secondly, attention should also be paid to the implementation of an active dissipative beach at the rear part of the tank to eliminate any numerical interference with the generated waves. Therefore, the generated waves may fade out after a short distance from the wave-maker for the wave patterns with small steepness ratios. As a final issue that should be considered is the requirement of long-term simulations to have sufficient wave data samplings for the FFT analyses.

Following the above mentioned discussions together with outputs of the initial verification test case where the wave steepness ratio is set to 1/20, a minimum wave steepness ratio of 1/10 (which gives $H/gT^2 \approx 0.016$) is chosen to be appropriate for the investigation of the physical properties of the generated wave patterns. This wave steepness value corresponds to the Stokes 3^{rd} order region of the wave abacus provided by [56] (see Fig.3.1).

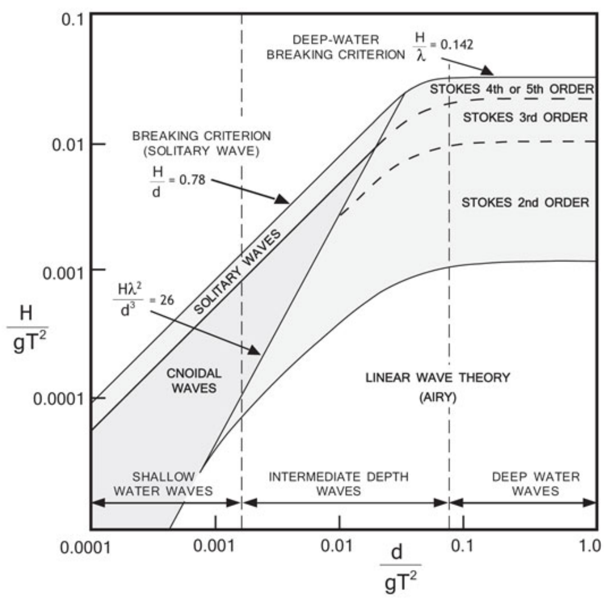

Figure 3.1 Wave conditions on [56] abacus

The geometrical parameters of the simulation cases and the equations of motion of the flap and piston type moving boundary wave-makers for the generation of regular and irregular wave trains will be defined in the following. Then, numerical results obtained in terms of time series of the free-surface elevations, frequency domain analyses and wave energies are given in a comparative manner with the theoretical solutions.

3.2.1 Definition of Problem Geometry

The schematic description of the geometrical parameters are displayed in Fig.3.2. The main dimensions of the wave tank are varied according to the wave-length in the regular wave simulations while the tank dimensions are kept as constant for the irregular wave test cases. To examine the capability of the proposed numerical scheme on capturing different moving boundary conditions, irregular wave simulations are conducted with both flap and piston type wave-makers.

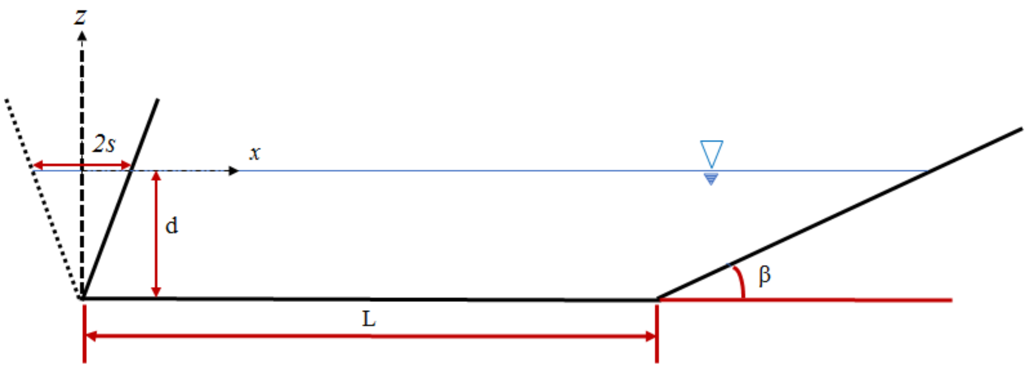

(a)

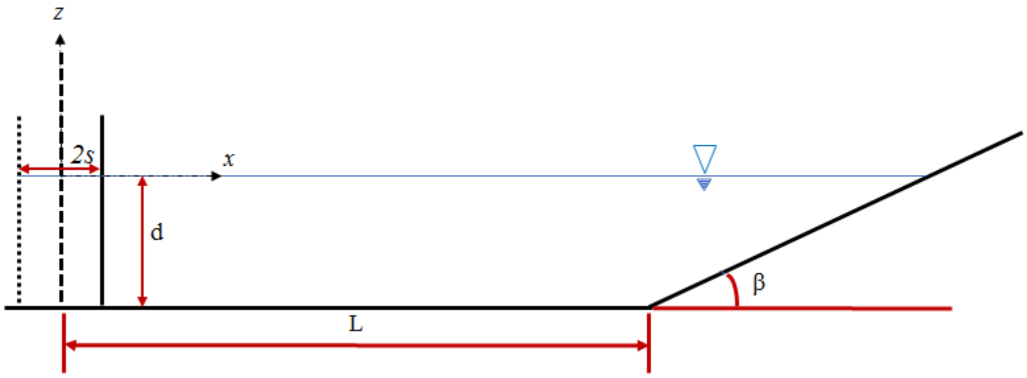

(b)

Figure 3.2 The schematic view of wave tank geometries for (a) flap (b) piston type wave-makers.

In regular wave generation simulations, the problem geometry is scaled with the expected theoretical wave-length in order to keep the number of particles to be the same in all test cases. The scaling procedure is implemented as follows: The depth of the tank is taken as $d = \lambda$ which satisfies the deep water assumption, the tank length is taken as $L = 5\lambda$ to generate sufficient number of waves in the problem domain, and initial particle spacing is set to $\delta x = \lambda/100$. In order to prevent any damping effect and stay sufficiently away from the wave maker, the time series of the wave elevations are recorded at $x_{rec} = 2\lambda$. As the present study aims to model a wave tank without any numerical damping or sponge layers, the generated waves are forced to fade out naturally by the help of a beach region at the end of tank with an inclination of $\beta = 21.8°$.

Additionally, H/λ ratios of 1/6, 1/7 and 1/8 for the wave-length of $\lambda = 0.5$ [m] are considered for the test cases, which are simulated to investigate the effect of wave steepness on the formation of higher order modes in frequency domain analyses.

To test the capabilities of the present SPH scheme, a further investigation is performed on the modelling of irregular wave spectra. For the simulations of irregular wave cases, the length and depth of the channel are set to $L = 5.0[m]$ and $d = 1.0[m]$, respectively, while the wave elevations are recorded at $x_{rec} = 2.0[m]$. To examine the accuracy of the simulation results, a well-known Joint North Sea Wave Project (JONSWAP) ([38]) wave spectrum is studied. In the present study, the following JONSWAP wave spectrum for limited fetch conditions recommended by the [46] is implemented:

$$\begin{aligned} S(f) &= \alpha g^2 (2\pi)^{-4} f^{-5} exp[1.25(f/f_p)^{-4}]\gamma^{exp[-\frac{(f-f_p)^2}{2\tau^2 f_p^2}]} \\ \tau &= 0.07, f \leq f_p \\ \tau &= 0.09, f > f_p \\ \alpha &= 0.0081 \end{aligned} \tag{3.1}$$

where g is gravitational acceleration, f is the instantaneous frequency [Hz], f_p is the peak frequency value [Hz] and $\gamma = 3.3$ is the wave peak enhancement factor.

3.2.2 Results of Regular Wave Simulations

An initial verification study is performed using the simulation results of [10] at deep water conditions (d/λ=1) and wave steepness value of $H/\lambda = 1/20$. The wave characteristics of this case remains within the Stokes 2^{nd} order region of the [56] wave abacus and was considered to be an assessment case to determine required particle resolution of the problem domain. The generated wave profiles before the starting point of the beach is compared in Fig.3.3. It can be seen from the figure that the particle size is in comparable order with the generated wave amplitude due to the relatively lower steepness ratio of the case. As a second consequence, the dissipative beach is effective especially after $x/\lambda = 3$ which is expected from theoretical point of view because of the lower energy level of generated waves. On the other hand, according to the graphs of wave elevations at $x/\lambda = 2$ and the corresponding FFT analysis which are displayed in Fig.3.4, the damping effects of the dissipative beach are not encountered at the given probe location. Additionally, the FFT analyses shows a consistent manner with the Stokes 2^{nd} order region of the wave abacus, where the minor second harmonic mode appears after the dominant frequency mode. Regarding to the simulation results of the test case with $H/\lambda = 1/20$, it is decided to increase wave steepness ratio to $H/\lambda = 1/10$ for non-breaking wave simulations to ensure the elimination of damping effects at probe location, $x/\lambda = 2$ together with keeping the ratio of particle size to wave amplitude in a lower level. The determination of generated wave characteristics along this direction makes it possible to maintain long-term wave data recordings at the probing location which is sufficiently far away from the active damping region together with having higher particle resolution at single wave height.

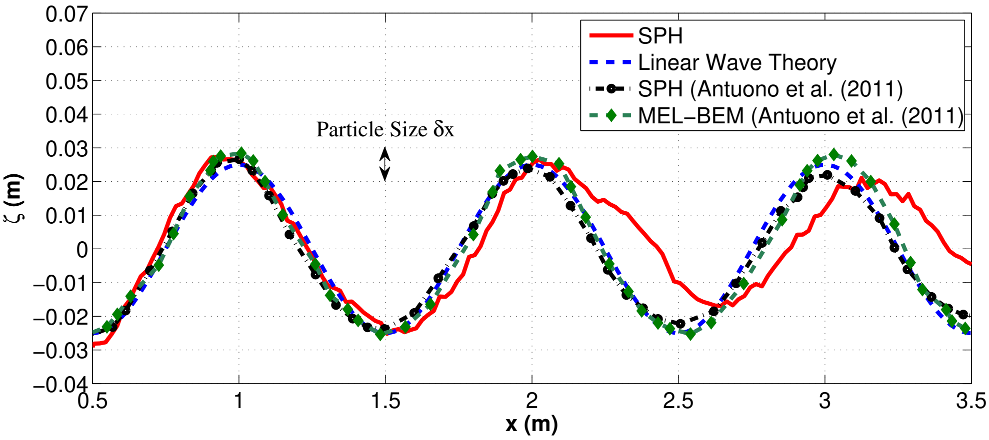

Figure 3.3 Comparison of wave profiles for the test case $\lambda = 1.00m$ and $H/\lambda = 1/20$ at a fully developed wave regime.

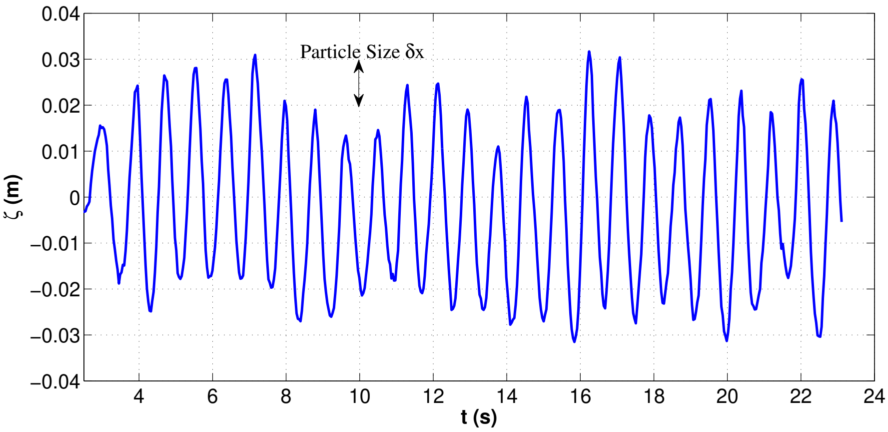

(a)

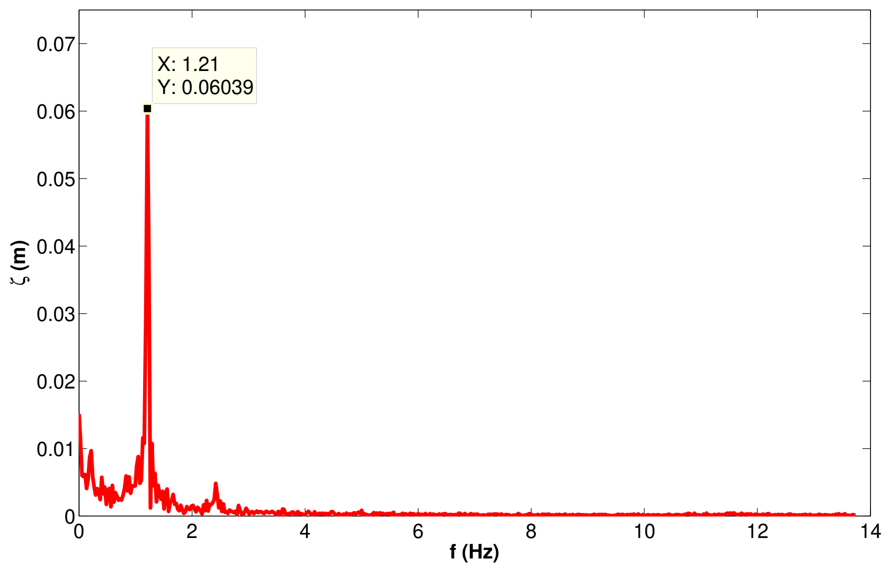

(b)

Figure 3.4 SPH time series of the wave elevations at $x = 2\lambda$ (a) and its frequency domain representation (b) for $\lambda = 1.00m$ and $H/\lambda = 1/20$.

Further regular wave generation test cases of the present work may be classified in two groups: The first group has ten different wave-length cases which aims to examine the accuracy of the generated wave trains in terms of wave heights, wave frequencies and wave energy densities for the wave steepness ratio of 1/10. The remaining group of test cases focuses on the higher steepness ratios to scrutinize the conditions for wave-breaking and to investigate the existence of higher order frequency modes by means of FFT analysis.

To avoid redundancy in the text, only three representative results of the test cases with wave-lengths 0.25 [m], 0.50 [m] and 1.00 [m] are presented in Fig.3.5. Here, ζ

denotes the wave elevation from the initial free surface level in the time history plots. As can be seen from the figures, three frequency peaks occurs in all FFT graphs in compliance with the Stokes 3^{nd} order region of [56]. The FFT analyses also points out that the calculated wave heights and the dominant frequencies obtained at the probe location are in match with the linear wave theory which indicates the high capability of presented SPH scheme on the generation of desired wave characteristics.

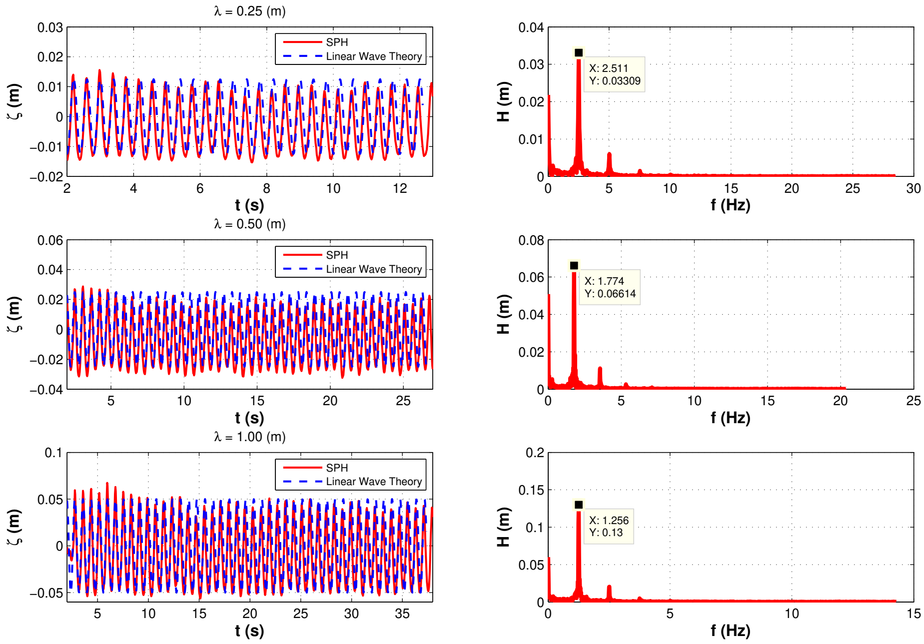

Figure 3.5 Time series (left) and FFT analyses (right) for the wave-lengths 0.25 [m], 0.50 [m], and 1.00 [m].

Table 3.1 provides an extended summary of the given wave elevation time histories and the FFT analyses where the SPH results are compared with the expected theoretical (linear) wave frequencies (ω_T), wave heights H_T and wave energy densities (E_T). In the table, theoretical wave frequencies are calculated as $\omega_T = \sqrt{2\pi g/\lambda}$ under the assumption of deep water condition. The wave frequencies of the presented SPH scheme are derived through a FFT analysis and the first frequency modes are provided in the table. The total mean wave energy through a period is calculated by; $E_T = \frac{1}{8}\rho g H_T^2$ per wave-length per unit width ([11]) for all test cases. As to the SPH calculations of wave energy densities, the particles that are within the half wave-length distance forth and back from the wave probe location are considered. The total mechanical energy of the particles inside this region are obtained as follows:

$$E_{SPH} = \frac{1}{T}\sum_{i=1}^{N_\lambda}[\frac{1}{2}m_i v_i^2 + m_i g z_i - (m_i g z_i)^{(0)}] \qquad (3.2)$$

where N_λ is the number of particles inside the defined unit wave-length region, v_i is the particle velocity magnitude, m_i is the particle mass calculated by $m_i = \rho(i)V(i)$, and $(m_i g z_i)^{(0)}$ is the potential energy of the particles at $t = 0$.

It can be seen from Table 3.1 that the dominant wave frequency values of the SPH results are in match with at least an accuracy of 99.5% with the expected theoretical wave frequency value. The higher frequency modes in FFT analyses occur in all test cases which lead to a limited variation in wave height levels. As the higher frequency modes are significantly lower than the dominant frequencies, they play a minor role to dampen the wave elevations and the wave heights at the dominant frequencies show good agreement with the expected linear wave theory values. It should be noted here that both H_T and E_T values are extracted from the linear theory and the discrepancy on the wave heights found between the dominant frequency values of SPH and linear theory is around $20-25\%$. One should also bear in mind here that the SPH method inherently demonstrates the non-linear character of the flow.

To further examine the stability, robustness and accuracy of the proposed SPH scheme, wave energy densities are calculated according to Eq. 3.2 where all of the mechanical energy values of the particles inside the defined region are taken into account. The results shows excellent compatibility with the theoretical wave energy densities based on the wave height values especially for the wave-length values below 0.90 [m]. The existence of higher order of accuracies on the wave energy results of shorter wave-length simulations should be attributed to the decreasing of particle resolution in the problem domain in longer wave-length cases to keep the total particle number equal in all test cases.

Table 3.1 The comparison of SPH results with expected theoretical wave frequencies (ω_T), wave heights (H_T) and energy densities (E_T).

$\lambda[m]$	$\omega_{SPH}[Hz]$	$\omega_T[Hz]$	$H_{SPH}[m]$	$H_T[m]$	E_{SPH}	E_T
0.25	2.511	2.499	0.0330	0.0250	0.7536	0.7664
0.30	2.283	2.281	0.0387	0.0300	1.1908	1.1040
0.40	1.975	1.976	0.0511	0.0400	1.9384	1.9620
0.50	1.774	1.767	0.0662	0.0500	2.9486	3.0654
0.60	1.604	1.613	0.0694	0.0600	4.1741	4.4140
0.70	1.510	1.493	0.0875	0.0700	6.3916	6.0100
0.75	1.444	1.443	0.0993	0.0750	7.2834	6.8980
0.80	1.395	1.397	0.1006	0.0800	7.4475	7.8480
0.90	1.322	1.317	0.1199	0.0900	9.3568	9.9330
1.00	1.256	1.250	0.1301	0.1000	13.662	12.260

To investigate the effect of wave steepness, a further study has been performed with increasing H/λ ratios of $1/8, 1/7$ and $1/6$ at $\lambda = 0.50$ [m]. It is known by means of Stokes' perturbation expansion that the breaking limit of the deep water waves is $H/\lambda \sim 1/7$ ([102]). Similar to the previous test cases, the wave elevation time series and their FFT analyses are given in Fig.3.6. It can be deduced from the figure that higher frequency modes exhibit themselves increasingly with increasing value of wave steepness. The occurrence of high frequency modes yields damping effects which can be observed in free-surface elevation at wave steepness of $1/6$ and $1/7$ where the inception of wave-breaking phenomena starts. Another remarkable point in all three cases, the dominant frequency value appears at exactly the same frequency of 1.754 [Hz] which reveals the robustness in the predictability of the proposed SPH numerical scheme.

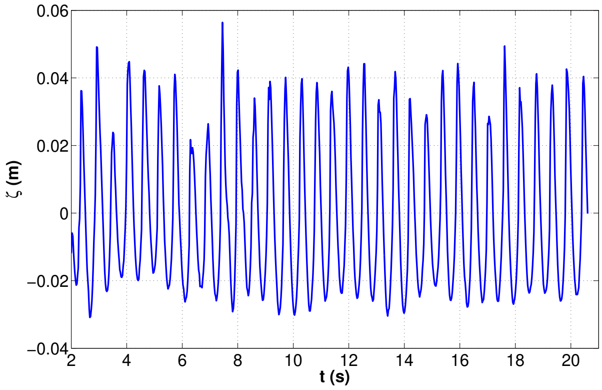

(a) Time series of $H/\lambda = 1/6$

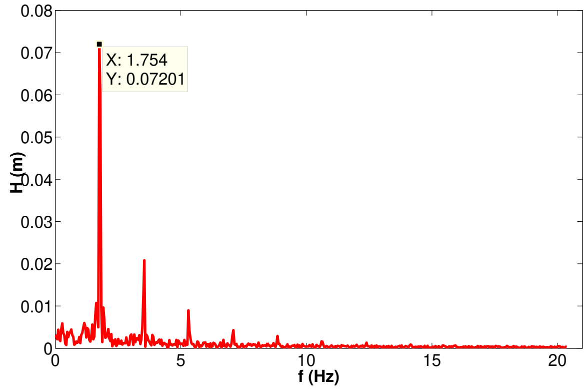

(b) FFT analysis of $H/\lambda = 1/6$

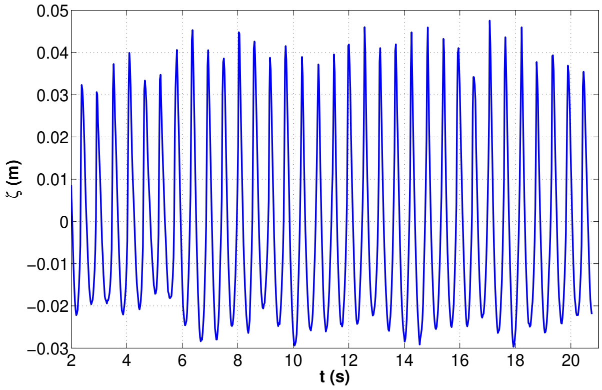

(c) Time series of $H/\lambda = 1/7$

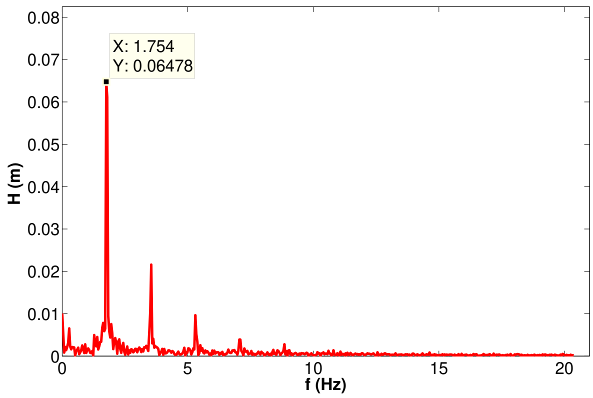

(d) FFT analysis of $H/\lambda = 1/7$

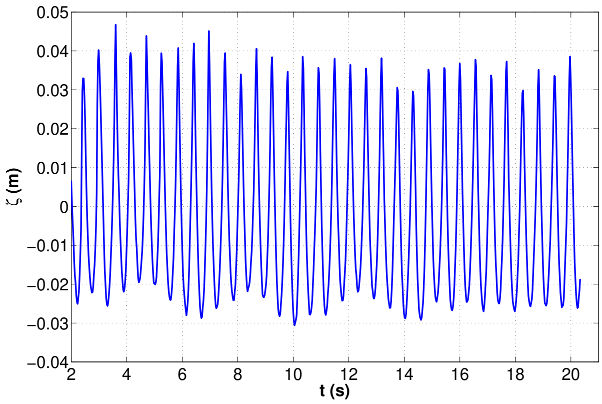

(e) Time series of $H/\lambda = 1/8$

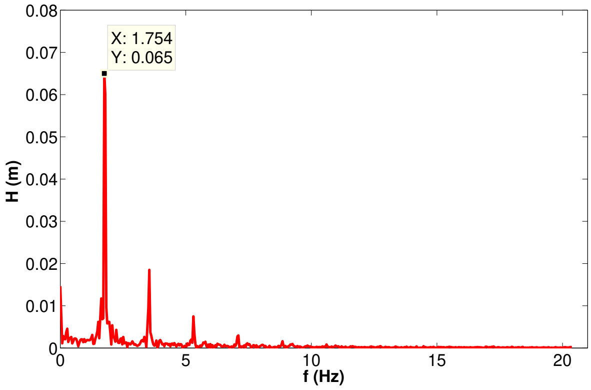

(f) FFT analysis of $H/\lambda = 1/8$

Figure 3.6 Time series of the wave elevations (left) and their frequency domain representation right at $\lambda = 0.50[m]$ test case with variable wave steepness ratios.

3.2.3 Results of Irregular Wave Simulations

Additionally, we also include irregular wave simulations, although sea spectra or wave energy spectrums are known to be based on linear wave theory paving a way to superposition. For this purpose, the presented SPH methodology is tested to see its capability on modelling irregular wave trains. Both the flap and piston type wave-makers are considered. JONSWAP wave spectrum with four different peak frequency test cases are modeled for which the details of the simulation parameters are given in Table 3.2.

The assignment of peak frequency value is a critical choice that needs to be considered carefully to overcome the problem of computational cost in irregular wave simulations. The first difficulty on the determination of peak frequency value is directly related to the main dimensions of the wave tank because the peak frequency defines the value of possible maximum wave-length of the wave spectrum. As the longer wave-lengths require a longer tank length (L), it results with the utilization of more particles in the problem domain. Secondly, the wave amplitude values are determined through the equations 2.18-2.22 and in the end they are also connected to the choice of peak wave frequency where having higher peak frequency values will lead to the generation of lower wave amplitudes. In order to capture these small wave amplitudes with a high order of accuracy, one should utilize higher number of particles inside the domain. Along with this framework, it has been decided to keep the peak frequency values between the range of 0.5 - 0.8 which provides reasonable computational costs for the simulations with an admissible order of accuracy.

Table 3.2 The problem parameters of irregular wave simulation cases

Case No	Wave-maker Type	$\delta x[m]$	Frequency Range [Hz]	Peak Frequency [Hz]
1	Flap	0.01	0.35-2.00	0.60
2	Flap	0.01	0.40-2.50	0.80
3	Piston	0.025	0.30-2.00	0.50
4	Piston	0.025	0.30-2.00	0.60

The irregular wave simulations have two main branches: The first two test cases are performed by a flap-type wave-maker with higher particle resolution, in shorter simulation time while long-term simulations with less particle resolution are carried out by a piston-type wave-maker system in the last two test cases. The theoretical results (Airy wave theory) and the computed free surface elevations are compared in Figures 3.7 and 3.9 for flap and piston types, respectively, where the wave elevations obtained by the present study are in a good match with the theoretical results. It is as well understood from Figures 3.7 and 3.9 that the degree of agreement increases with the increase of peak frequency. It should be noted here that the theoretical results come from the linear approach (JONSWAP spectrum) whereas SPH results inherently include non-linear effects. Thus, for this reason, one may expect a deviation to some extend between the theoretical and SPH results. As a second consequence related with the energy densities given in Figures 3.8 and 3.10; in the last two cases where the total simulation times are longer with respect to the initial two test cases, the noise in the wave energy density are reduced and the distribution of wave energy over the frequency becomes more consistent with the theoretical wave energy spectrum. To summarize the outcomes of the test cases, we can conclude that the proposed SPH scheme has the capability of modelling the generation of irregular wave spectrum with different types of moving boundaries where higher order of accuracies can be achieved with the consideration of larger peak frequencies and longer simulation times.

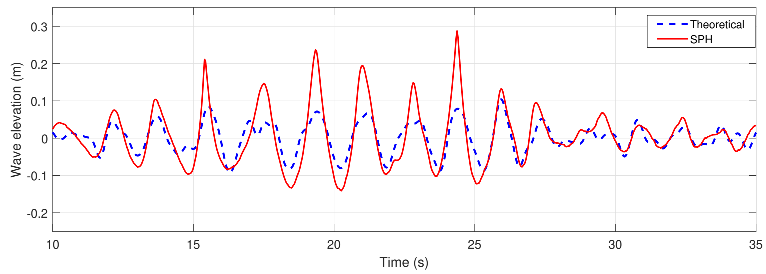

(a)

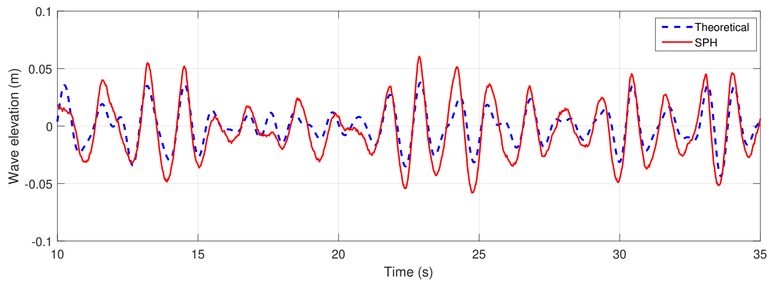

(b)

Figure 3.7 Time series of the wave elevations (Theoretical: Airy wave theory) for the first (a) and second (b) test cases in Table 3.2.

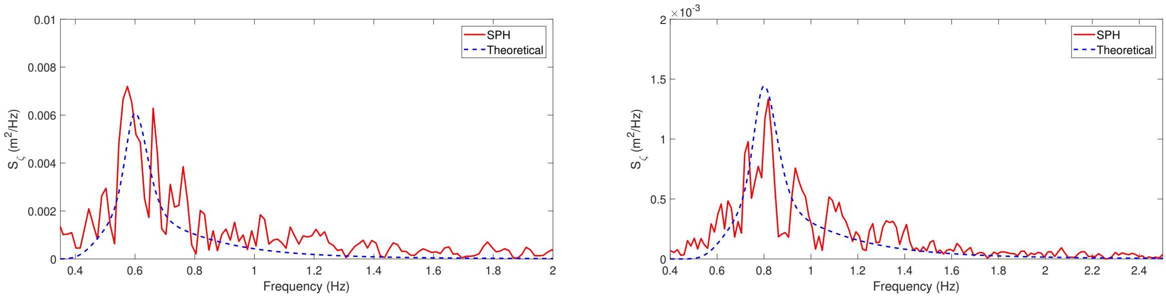

(a) (b)

Figure 3.8 Frequency domain analyses of the wave energies (Theoretical: Airy wave theory) for the first (a) and second (b) test cases in Table 3.2.

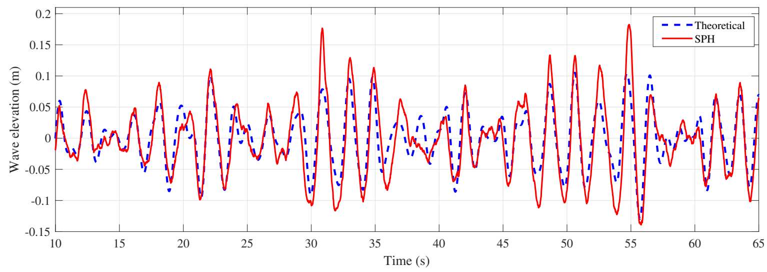

(a)

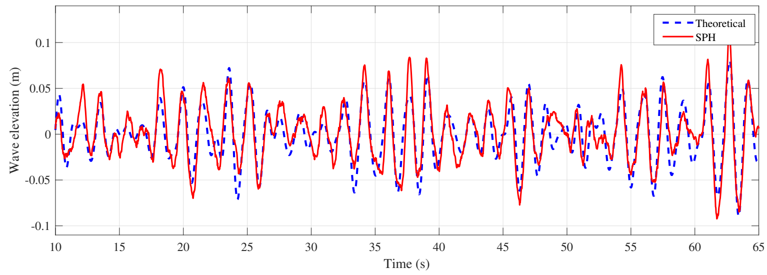

(b)

Figure 3.9 Time series of the wave elevations (Theoretical: Airy wave theory) for the third (a) and fourth (b) test cases in Table 3.2.

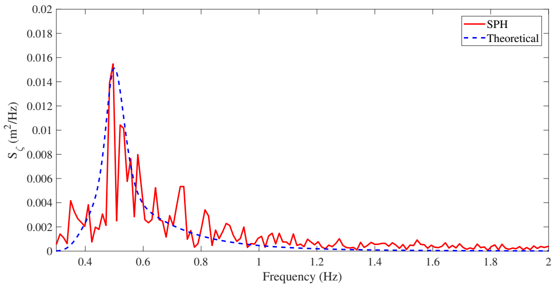

(a)

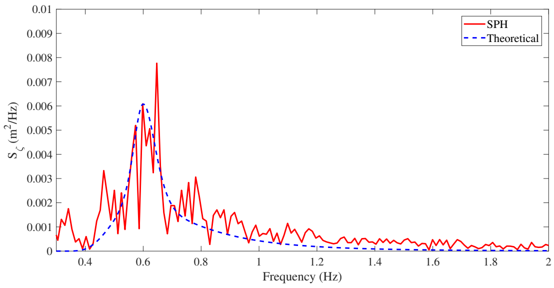

(b)

Figure 3.10 Frequency domain analyses of the wave energies (Theoretical: Airy wave theory) for the third (a) and fourth (b) test cases in Table 3.2.

3.3 Conclusion

Computational modelling of a wave generator system that can generate regular and irregular wave trains has been made by means of WCSPH approach in SPH. To enhance the robustness of the numerical method and accuracy of the results, additional treatments, which have been successfully adopted in our previous violent flow studies, namely, density smoothing, hybrid VFS-APD algorithm and kernel gradient correction has been included into the solution scheme. Navier-Stokes and Continuity equations are utilized as governing equations of the fluid flow where pressure and density are coupled through an equation of state.

Regular wave simulations are performed by considering ten different wave-length test cases with a wave steepness of 1/10 which leads to an investigation of non-breaking wave conditions. The time series of wave elevations at given wave probe point and corresponding FFT analyses are provided for each cases and compared with the results of linear wave theory. It is observed that the dominant frequencies occurred in the simulations are in very good agreement with the theoretical results where higher order modes also noticed in all test cases. The existence of higher order frequency modes (although with significantly low magnitudes) points out the non-linear nature of the generated waves which also cause a limited variation in the wave elevations. Higher harmonics naturally contained in the present SPH formulation are said to be the main cause of slight discrepancy between the present results and those of the linear theory.

To conduct a further inquiry on the nature of the non-linearity of regular wave system, wave steepness of the generated waves has been varied. The frequency domain results have shown that the order of higher modes are increasing with the higher wave steepness values while the magnitudes of the second and also third modes also rising which lead to remarkable damping effects on the wave elevation time series. As a final observation of the numerical simulations associated with the regular wave generation, the limiting value of wave steepness, implying the inception of wave-breaking, is found fully compatible with the theoretical value of 1/7.

The other concern of the present work is the modelling of irregular wave patterns by using flap and piston type wave-makers. As a consequence of a survey procedure to find a compromise between computational time and the order of accuracy of the solutions, a peak frequency range of 0.50 - 0.80 [Hz] has been determined as a reasonable modelling region in the present study for the implementation of JONSWAP wave spectrum. In the light of the wave elevation time series and the wave energy spectrum analyses, it has been observed that the proposed WCSPH algorithm have the capability of capturing the wave characteristics and produce compatible results with the theoretical solutions.

4. A Preliminary Investigation on the Modelling of Overtopping Wave Energy Converter Systems by SPH Method

4.1 Introduction

This chapter focuses on the hydrodynamic analysis of Overtopping Wave Energy Converter (OWEC) systems, providing a comprehensive overview of the state-of-the-art in this field. Among the pioneering overtopping converter devices is the Tapchan OWEC, located in Norway, boasting a maximum power capacity of 350 kW. Other noteworthy floating overtopping systems include the Wave Dragon, constructed in Denmark [2], and the Seawave Slot Cone Generator, which incorporates three reservoirs stacked vertically [120].

OWEC devices generate electricity by harnessing the power of overtopping waves, which are collected in a pre-storage system and subsequently discharged into the ocean via low-head turbines [34]. These systems are particularly suited for coastal regions characterized by high wave heights [2]. Accurately estimating the flow rate of overtopping waves is crucial during the design stages of an OWEC system, as it directly determines the amount of wave energy that can be harvested. Therefore, marine and coastal engineers involved in the conceptual design of WECs should employ high-fidelity Computational Fluid Dynamics techniques capable of accurately predicting mean overtopping discharges.

Along these lines, Victor and Troch [121] conducted an investigation into the performance of overtopping wave energy converters with various geometric configurations. Through experimental analyses, they developed a new overtopping prediction formula specifically for steep, low-crested structures. Additionally, Van der Meer and Bruce [118] proposed an overtopping prediction formula for OWECs based on their study of the UG10 dataset [121] and the CLASH database [20]. The UG10 dataset includes two crucial parameters, namely the slope angle α and the relative crest freeboard.

In this study, the non-dimensional average wave overtopping flow rate is calculated for a slope angle range of 25° to 60°, employing two different particle resolutions within the flow domain. The numerical results are then compared with the predictions obtained from the aforementioned formulas, and the findings are presented in Section 4.3.

4.2 Problem definition

This study examines the energy efficiency of an OWEC-type wave generator device by generating regular waves using flap-type moving boundaries. The schematic display of the two-dimensional numerical wave tanks used for the overtopping wave energy converter test cases is presented in Figure 4.1.

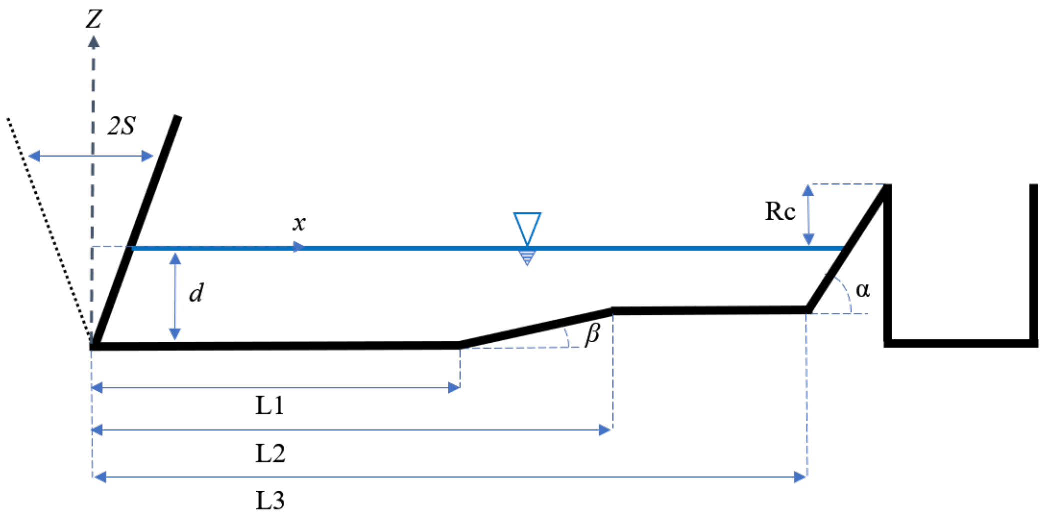

Figure 4.1 Schematic representation of the computational domain for the OWEC devices.

Simulations were conducted in a numerical wave flume with a length of $L_3 = 12.5$ m. The inclined beach has an angle of $\beta = 1/10$ and extends from $L_1 = 5$ m to $L_2 = 8$ m. The still water level was set at $d = 0.82$ m, and the relative crest height to significant wave height ratio was $R_c/H_{m0} = 0.2$ (see Fig. 4.1). For the simulations, Stokes' third-order regular waves were used with a period of 0.8 seconds, a wavelength of

1 m, and a wave height of 0.1 m. To assess the convergence and robustness of the numerical scheme, two different particle resolutions were employed: $d/60$ and $d/96$, resulting in the use of 25,140 and 59,603 fluid particles, respectively.

4.2.1 Overtopping prediction formulations

Recently, Victor and Troch [121] and van der Meer and Bruce [118] published overtopping prediction formulations for steep low-crested structures. In this study, the average overtopping rate obtained from Smoothed Particle Hydrodynamics (SPH) simulations is analyzed and compared with the provided prediction equations, which are summarized in Table 4.1.

Table 4.1 Overview of the prediction formula with their range of utilization for slope angle and relative crest freeboard [121].

	Range of cot α		
Range of $R_c/H_{m\mathbf{0}}$	$0.0 \leq cot\alpha \leq 1.43$	$1.43 < cot\alpha < 1.73$	$1.73 \leq cot\alpha \leq 2.75$
$0.0 \leq R_c/H_{m\mathbf{0}} \leq 0.8$	Eq.4.3	Min [Eqs.4.3, 4.4]	Eq.4.4
$0.8 \leq R_c/H_{m\mathbf{0}} \leq 2.0$	Eq.4.2	Min [Eqs.4.2, 4.1]	Eq.4.1

The average rate of overtopping of mildly sloping dikes exposed to non-breaking waves can be estimated using the following formula [121]:

$$\frac{q}{\sqrt{gH_{m0}^3}} = 0.20exp\left[(-2.6)\frac{R_c}{H_{m0}}\right], \tag{4.1}$$

$$\frac{q}{\sqrt{gH_{m0}^3}} = (0.033cot\alpha + 0.062)\,exp\left[(1.08cot\alpha - 3.45)\frac{R_c}{H_{m0}}\right], \tag{4.2}$$

$$\frac{q}{\sqrt{gH_{m0}^3}} = 0.2exp\left[(1.57cot\alpha - 4.88)\frac{R_c}{H_{m0}}\right], \tag{4.3}$$

$$\frac{q}{\sqrt{gH_{m0}^3}} = 0.11exp\left(-1.85\frac{R_c}{H_{m0}}\right), \tag{4.4}$$

Where q represents the average overtopping rate, α denotes the slope angle, R_c represents the vertical distance between the crest of the structure and the still water level (refer to Fig. 4.1), and H_{m0} represents the spectral wave height of the incident wave.

4.3 Results and Discussion

To evaluate the simulation results of the OWEC device in this study, the average overtopping rates calculated for eight different slope angles are compared with the prediction formulas from the literature [118, 121]. The comparative graph is presented in Figure 4.1. It can be observed that the SPH results closely follow the general trend of the prediction formulas, particularly as the particle resolution increases in the simulation.

For lower slope angles such as $\alpha = 25°$ and $\alpha = 30°$, the WCSPH results slightly overestimate the prediction formula. Conversely, for slope angles ranging from $\alpha = 35°$ to $\alpha = 55°$, WCSPH underestimates the average overtopping rate. However, it is notable that the results converge towards the prediction formula in high-resolution simulations. In the case of the highest slope angle, the prediction formula aligns with the WCSPH results obtained from both high and low resolution simulations.

These simulations demonstrate that the proposed WCSPH scheme consistently captures the average overtopping rates predicted by the empirical formula across a wide range of slope angle variations.

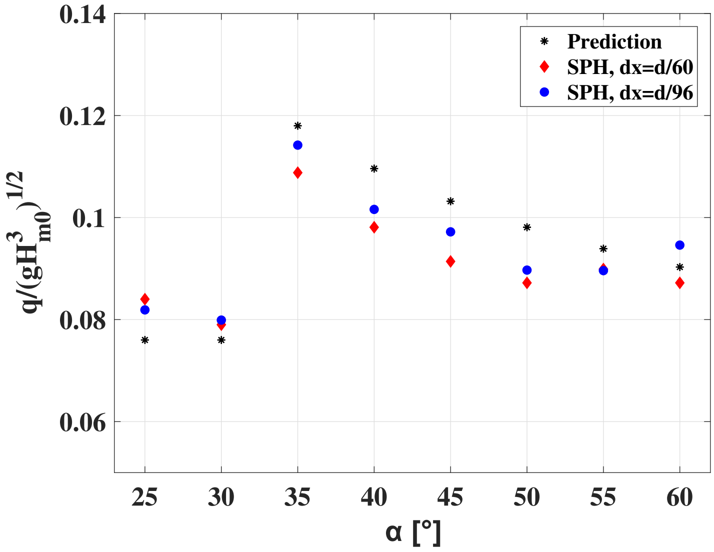

Figure 4.2 The comparison of SPH and Prediction formula average wave overtopping flow rate results in different slope angles.

4.4 Conclusions

In conclusion, the numerical performance of the proposed SPH scheme was evaluated through a quantitative comparison of the average overtopping rate for the OWEC device with various slope angles. The study focused on comparing the average overtopping rates obtained from numerical simulations at two different particle resolutions with existing prediction formulas available in the literature.

The results demonstrate that the proposed SPH scheme is capable of accurately capturing the average overtopping rates predicted by the empirical formulas across a wide range of slope-angle variations, particularly as the particle resolutions in the problem domain increase. The simulations validate the effectiveness of the SPH scheme in replicating the average overtopping rates predicted by the empirical formulas.

These findings highlight the reliability and applicability of the proposed SPH scheme for analyzing OWEC systems and their performance in terms of average overtopping rates. The scheme can serve as a valuable tool for marine and coastal engineers involved in the design and optimization of OWEC devices, providing insights into the hydrodynamic behavior and improving the overall efficiency of such systems.

5. A Numerical Investigation on the Energy Efficiency Enhancement of Oscillating Water Column Wave Energy Converter Systems

This work focuses on the geometry effects over the performance of OWC type WEC systems and searches for the OWC geometries that enhance the energy efficiencies under the same wave conditions. To analyze the hydrodynamic performances of the WEC systems, an in-house SPH code based on weakly compressible fluid approach is utilized. The energy efficiency enhancement studies of the determined OWC device are carried out with a two-step geometry modification procedure. The first step starts with the validation of the free-surface elevation and orbital velocity time histories. Then, a 3-by-3 simulation matrix which depends on the geometrical design parameters of chamber length and front wall draft is run at three different wave conditions and the OWC geometry that produces the maximum energy efficiency is determined. In the second step, the corner regions of the obtained optimal geometry are chamfered, and another simulation matrix is tested at the wave condition that yields to produce maximum wave energy. It is observed in this step that the energy efficiency index can still be improved by 4.3% by only chamfering the back face of the OWC chamber. To scrutinize the physical grounds of this increase, the correlation between the time-averaged vorticity and energy efficiency is presented. Finally, the performance of the best configuration is also examined in three different wave periods, where the suggested geometry shows better performance with respect to base geometry results in all wave conditions.

5.1 Introduction

Because of global warming due to the dramatic increase in CO_2 levels mainly associated with the massive fossil fuel consumption, energy production relying on renewable sources (i.e., solar, wind, and wave energies) has increased tremendously in the last two decades [1, 87]. In 2017, it was reported that almost 20% of the total energy generation of humankind is based upon the renewable energy sources [26]. Among these renewable energy resources, the high theoretical potential of the ocean energy resources [77] keeps free surface waves to be a prominent candidate for generating green electricity [24], although large-scale utilization of wave energy converters (WECs) still has not reached a mass-marketable level [88].

The main challenge in the commercialization of wave energy converters (WEC) is the requirement of high investment capitals and operational costs of harvesting energy from waves in harsh offshore and nearshore conditions [97]. So far, several attempts have been made to overcome these hurdles by offering various WEC designs. To improve the efficiency of the WECs, various concepts and designs have been developed, where the number of patents has been reached to more than a thousand as of 2002 [15]. Despite the considerable variation in the suggested concepts, WECs are generally categorized by types of harvesting technology as oscillating water column, oscillating wave surge converter, submerged pressure differential, and overtopping device [24]. These systems can be placed along the shoreline as stationary structures or employed as floating structures on the open seas. General reviews of the existing concepts and designs of wave energy converters can be found in the referenced studies [9, 27, 63, 71].

The Oscillating Water Column (OWC) is one of the most promising concepts which have reached the prototype development stage in some regions, e.g., the LIMPET experimental plant in Islay Island, Scotland [109], the Mutriku power plant in Spain [44], the Pico power plant, in Portugal and the REWEC3 experimental plant, in Italy [109]. OWC systems consist of a hollow and partially immersed storage that is open to water and a chamber of trapped air. Ocean waves cause the free surface inside the tank to oscillate vertically, which pressurize and depressurize the air inside the chamber. This trapped air's pneumatic power enters and leaves the bidirectional turbine located on the device chamber and turns into electrical energy through power take-off systems [51].

In recent years, several experimental and numerical studies have been conducted to investigate and characterize the hydrodynamic behavior of WECs from different aspects. Khatibani et al. [52] studied the dynamics and power absorption of the wave energy converter and proposed a new hybrid single-pile wind turbine with two pitching WECs for the coast of Dayyer port in the Persian Gulf. They developed a numerical model to study and analyze the dynamics of the hybrid system and the effect of the damping coefficient between the wind turbine and the WEC on power generation under operating conditions. Morris-Tomas et al. [78] performed experiments to study the effect of the front wall configuration on the hydrodynamic efficiency of OWCs. Chang et al. [14] carried out an experimental study to find the optimal geometrical design to achieve the maximum hydrodynamic efficiency of the OWC device. Various geometric parameters were tested. The results showed that chamber geometry, especially the backplate slope, substantially influenced the OWC performance.

Although experimental research captures and reveals such devices' hydrodynamic behavior in a more realistic way, they are often known as expensive and time-consuming tools which may also suffers from the scale effects to use at the design stage. Alternatively, compared to experimental testing, a reliable and less costly technique is computational modeling and analysis of the hydrodynamic performance of OWCs using numerical wave tanks. Simonetti et al. [106] used a mesh-based finite volume method in OpenFOAM environment to analyze a fixed asymmetric OWC device. The results showed that chamber length, front wall draught, and relative OWC PTO damping had a strong effect on OWC efficiency. As shown in [81], chamber length has a significant effect on OWC performance compared to other OWC geometric parameters. Also, the angle of inclination in the bottom profile is an important parameter for shoreline OWC efficiency. Kamath et al. [50] investigated the hydrodynamic behavior of a 2D OWC under various wave conditions; they used the REEF3D CFD code in their numerical study. The rigid piston-like motion of the inner free surface was seen in the simulation with lower wave steepness, while the non-uniform motion was observed at higher wave steepness.

In addition to widely implemented mesh-based computational solutions [25, 50, 95, 108], which may have difficulties in capturing the nonlinear dynamics of high free-surface deformations in the problem area and the instantaneous response of WEC device in severe wave conditions, in the last decade, meshless techniques have attained significant interest in providing high-fidelity results [6, 33, 86, 105]. Luo et al. [66] reviewed the state of the art in the application of particle methods to hydrodynamic problems in marine and coastal engineering. Particle-based simulations of wave generation, propagation, and refraction, and associated turbulence generation and dissipation, air entrainment, and mass transport are discussed. Fu et al. [33] used a semi-Lagrangian meshless frame to investigate the sloshing phenomenon in a two-dimensional numerical tank. Their approach is shown to provide more stable and accurate results than one with an explicit mesh-based scheme. Among these meshless methods, Smoothed Particle Hydrodynamics (SPH) is one of the most popular mesh-free computational methods used to model various physical fluid flow conditions [4, 40, 100, 99]. He et al. [40] developed a coupled weakly compressible and total Lagrangian SPH(WC-TL SPH) method to simulate the interactions of elastic bodies with free surface flows. Khayyer et al. [37] briefly reviewed recent progress in the development of entirely Lagrangian, mesh-free computational methods for hydroelastic fluid-structure interactions in marine engineering and highlighted some important issues in this context. Almasi et al. [4] presented a multi-phase Incompressible Smoothed Particle Hydrodynamics (ISPH) method to examine complicated multi-physics electrohydrodynamics (EHD) problems. Moreover, due to its unique advantages in modeling highly nonlinear free-surface problems, the SPH approach is widely used to study coastal and marine engineering problems [83, 90, 98, 122]. Gotoh et el. [36] provides an update on recent advances in particle methods used in coastal and marine engineering. They discuss recent advances in accuracy, stability, conservation properties, fluid-structure interactions, and computational efficiency. Lyu et al. [67] provided a detailed overview of SPH-based hydrodynamic simulations for ocean energy systems. The main focus is on three topics: SPH-based numerical fluid tanks, multiphysics SPH techniques for simulating ocean energy systems, and finally computational efficiency and capacity. Ozbulut et al. [83] utilized the SPH technique in order to model a numerical wave tank. A wide variety of test cases with different wavelengths and steepness ratios for regular and irregular ocean waves are investigated using piston and flap type wavemakers. The application of SPH method to model the wave energy converters has also increased over the past few years [98, 17, 22, 124]. Crespo et al. [17] simulated wave interaction with an offshore OWC device in a numerical wave tank by an open-source SPH code (DualSPHysics). It has been proven that their models can accurately create the free-surface evolution inside the chamber when the air pressure is neglected. Wen et al. [124] used an improved SPH model to investigate the hydrodynamic performance of onshore OWC and considered the turbulence effect during their work. It was demonstrated that a sloshing phenomenon could be observed in the OWC chamber for a smaller value of the front wall depth. More recently, Ropero-Giralda et al. [98] utilized the SPH method to investigate the efficiency and survivability of a point-absorber type WEC device under different regular wave conditions. Recently, Quartier et al. [98] used the SPH approach to numerically model a OWC WEC. The PTO system is numerically modelled by applying a force to a plate floating on the free surface inside the OWC chamber. This avoids the simulation of the air phase, which is computationally intensive in SPH methods. During the review process, a new closely related reference was published by Soleimani et al. [110]. In this study, a OWC WEC device is modeled using the WCSPH method. The turbine effect was simulated by applying an equivalent orifice damping force to a thin plate in the chamber. The flow and pressure drop across the orifice were determined from the plate's stroke velocity. The model results were validated by an experimental study at the Technical University of Denmark.

In this study, the Weakly Compressible SPH (WCSPH) approximation [35] is employed to investigate the hydrodynamic characteristics and the energy efficiencies of OWC type wave energy converter system. The current geometrical model of the present study is assumed to be the simplified version of the 3D case due to its longitudinal symmetry, where the validity of the results can be generalized for the 3D cases by ignoring the effects of higher-order terms related to the eddy-vortices. The proposed in-house SPH code is validated by an experimental study [47] consisting of a stationary OWC with an open chamber. Additionally, a particle resolution and convergence test is also performed to determine the optimum particle resolution on the problem domain. After achieving accurate results by utilizing the proposed SPH scheme on OWC system, a two-step efficiency enhancement study is performed based on the geometrical modifications of the chamber part in the OWC device to obtain the configuration that provides maximum available wave energy. In the first step, the geometrical parameters, length, and front wall draft are varied to obtain the maximum harvested energy in three different wave periods. Using the best geometrical configuration that leads to maximum wave energy production among all wave period conditions, the second step is applied by chamfering the corner parts of the chamber region considering all possible configurations. As a final scrutiny, an investigation to obtain the relationship between the time-averaged magnitude of vorticity in the OWC inner channel and the hydrodynamic efficiency is performed through a quantitative comparison among all test cases. The novelty of this study lies in the systematic and encompassing analysis on the geometrical configuration of OWC system to increase the efficiency of harvested energy. Through varying the geometry of the OWC system, the hydrodynamic characteristic of the flow is enhanced such that the magnitude of the vorticity is reduced whereby the overall efficiency of the OWC system is improved.

The paper's organization is as follows: In the second section, the governing equations, and the discretized form of these equations based on the proposed WCSPH approach are mentioned. Following the definition of the physical and geometrical parameters of the problem, the hydrodynamic wave generation efficiency equations of the OWC devices are presented in the third section. In the fourth section, the robustness, consistency and accuracy of our numerical method is examined through comparing the experimental and theoretical results found in the literature [47]. Then the effect of geometrical modifications on the OWC system is scrutinized with quantitative and qualitative measures. Finally, the discussions on the obtained results and concluding remarks are highlighted in the last section.

5.2 Problem definition

In this work, the energy efficiency of OWC type wave generator device is examined through generating regular waves by using flap-type moving boundaries. The simulation cases have been chosen to provide intermediate water conditions which avoids shallow water effects in the wave tank and the high computational costs associated with deep water conditions. In addition, all test cases were simulated at a constant depth to reduce the problem parameters in the simulation matrix and focus directly on the geometric parameters of the OWC chamber. Finally, the value of the wave height was chosen to produce a comparable variation of the chamber pre-draft (y) heights. Considering all of these design criteria, the wave properties of this study remain at the upper limit of 2^{nd} order Stokes waves according to the Le Méhauté [57] abacus given in Fig. 5.1.

The schematic display of the two-dimensional numerical wave tank geometries employed in the comparisons of the experimental study of Iturrioz et al. (2014) [47] and all other oscillating wave energy converter test cases of the present work are presented in Fig. 5.2.

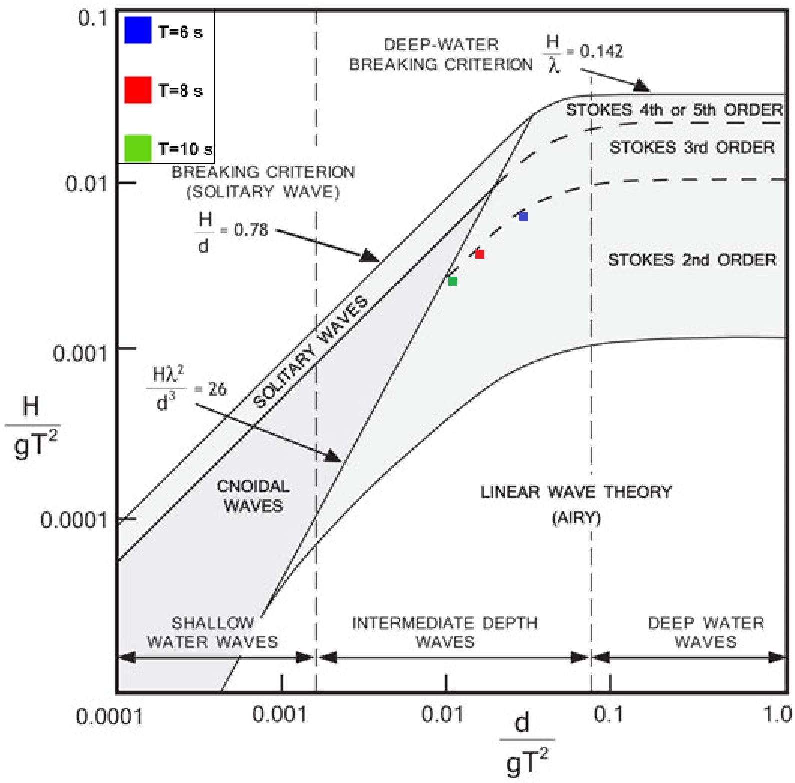

Figure 5.1 Wave characteristics of simulations with ($d = 10m$ and $H = 2.5m$) for different wave periods on Le Méhauté [57] abacus.

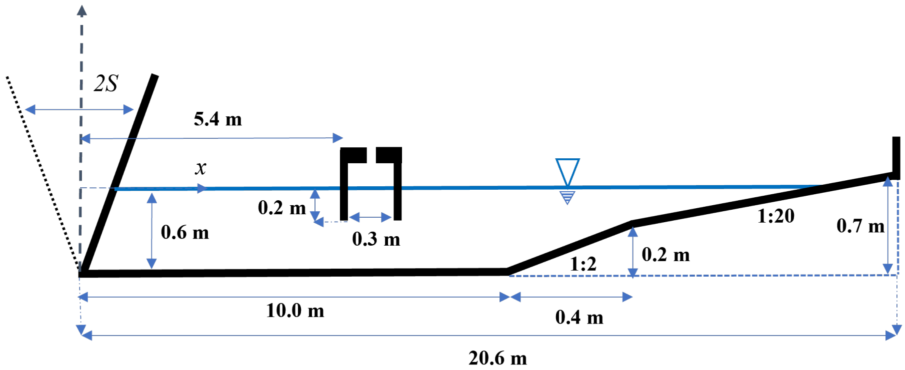

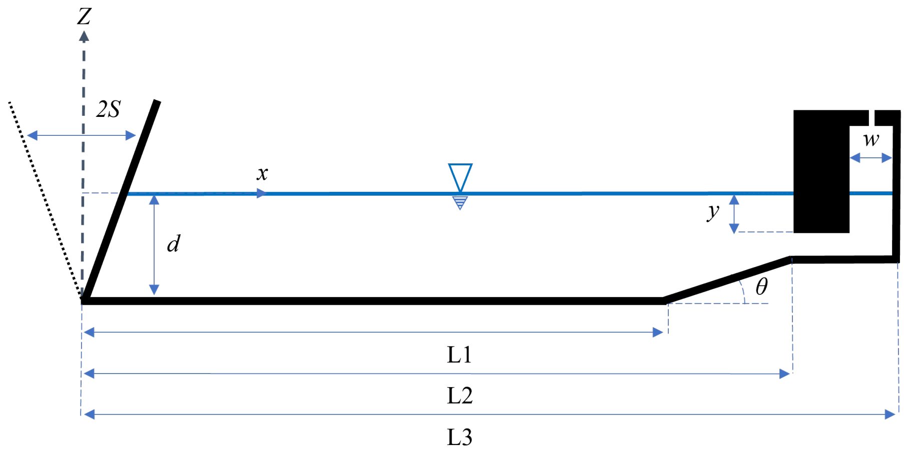

Figure 5.2 Schematic representation of the computational domain for the validation case wave tank (top) and the baseline OWC devices (bottom).

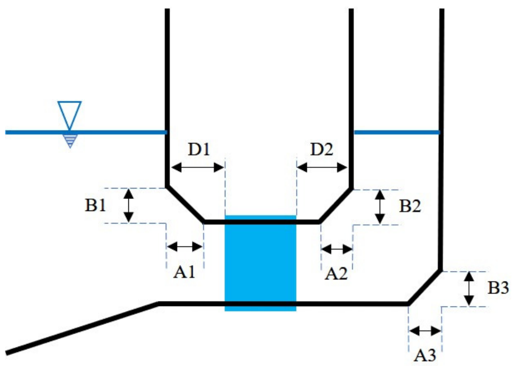

Figure 5.3 Schematic representation of the chamber region details utilized in the OWC geometry modification test cases (the blue color area represents the calculation region of vorticity magnitude).

The Stokes 2^{rd} order regular waves with a period of 3.2 seconds, and wave height of $0.08[m]$ are generated in the simulations when comparing the SPH results with the experimental measurements provided in [47].

The geometrical details of the baseline OWC device are defined as follows: The overall length of the channel equals to $L_3 = 120[m]$, the distance between the flap and the OWC front wall is $L_2 = 110[m]$ and the distance between the flap and the toe of the sloping wall is $L_1 = 102.5[m]$. The still water depth at the flap boundary (d) is equal to $10[m]$. θ is the 4/10 inclined beach's angle, w and y represent the optimization variables, namely, the chamber length and draft of the front wall, respectively.

Fig. 5.3 represents the schematic view of the OWC chamber with modified slope walls utilized in the performance enhancement simulations of the OWC geometry. The blue area inside the chamber indicates the calculation region of the time averaged vorticity magnitude which has the equivalent distance $D_1 = D_2 = 2.5[m]$ from both front and back sides of the OWC walls.

5.2.1 OWC hydrodynamic efficiency

The present study mainly concentrates on the investigation of increasing the harvested total wave energy in OWC systems by modifying the chamber geometries. Therefore, the energy losses due to the mechanical efficiency of turbine and energy conversion efficiency of the PTO system are not considered. To pursue an objective comparison between the efficiency levels of different OWC geometries, an Energy Efficiency Index formulation is identified according to the ratio of calculated mean pneumatic power absorbed by the OWC (without any contribution from the damping effects of PTO system) to the incident wave power per length multiplied by the chamber width b:

$$EEI = 100\frac{P_{OWC}}{P_i b}, \tag{5.1}$$

where the chamber width is taken as unity. The average pneumatic power harvested by the OWC can be expressed as follows:

$$P_{OWC} = \frac{1}{T_s}\int_0^{T_s} P(t)_{air} Q_t \mathrm{d}t, \tag{5.2}$$

here, T_s indicates the total duration of the simulation, $P(t)_{air}$ represents the instantaneous differential air column pressure obtained from numerical simulation, Q_t is the air volume flux inside the OWC chamber, and dt represents the time step of the simulation:

$$Q_t = bwv(t), \tag{5.3}$$

In Eq.5.3, w is the length of the chamber and $v(t)$ is the instantaneous vertical velocity of free-surface in the OWC chamber, which is calculated by averaging the vertical velocity of the free-surface particles inside the OWC chamber at each time step.

The relationship between the air pressure and air flow rate at the turbine inlet can be expressed with the following parabolic expression [64, 107, 128]:

$$P(t)_{air} = \begin{cases} (k_{dm} q_t)^2, & q_t > 0, \\ -(k_{dm} q_t)^2, & q_t \leq 0, \end{cases} \tag{5.4}$$

where q_t is the volume flow rate of air per second per unit width ($q_t = Q_t/b$) and k_{dm} is the damping term in the OWC chamber which is defined as:

$$k_{dm} = \frac{B^* {\rho_{air}}^{0.5}}{w}, \tag{5.5}$$

Here, ρ_{air} represents the air density (taken as, $1.225[kg/m^3]$) and B^* is a dimensionless damping coefficient representing the relation between the pressure drop in the OWC chamber and the turbine's flow rate. The damping coefficient depends on the utilized turbine characteristics which may significantly affect the overall performance of the OWC device [64]. To keep the simplicity and for the sake of quantitative comparison in the representation of the energy efficiencies of each OWC geometries, B^* is considered as unity in all simulation cases. One can assign the specific value of B^* to determine the total power harvested by the OWC for the given wave conditions and OWC device geometries.

The average incident wave power per unit width for the Stokes 2^{nd} order wave is expressed as [19].

$$P_i = \frac{1}{16} \rho g H_i^2 \frac{\omega}{k} (1 + \frac{2kd}{\sinh(2kd)})(1 + \frac{9}{64} \frac{H_i^2}{k^4 d^6}), \tag{5.6}$$

where H_i is the incident wave height, ω denotes the angular frequency of the incident wave, and d is the depth of water. By substituting all of the expressions into the OWC energy efficiency index, it can be simply calculated as follows:

$$EEI = \frac{100 \rho_{air} w (B^*)^2 \int_0^{T_s} |v\,(t)^3| \mathrm{d}t}{T_s P_i}. \tag{5.7}$$

5.3 Results and Discussion

Simulation results of OWC type wave energy converter device are presented in this section. As a first step, the validation and verification of the proposed numerical scheme is examined through comparing the free-surface deformations and velocity components inside the OWC chamber with the available experimental and theoretical results of the literature. In the former test case, the numerical performance of the proposed SPH algorithm is validated through the comparison of free-surface elevation in the middle of the OWC device with experimental and time-domain results of Iturrioz et al. [47]. Additionally, a resolution test has also been performed to achieve the convergence of the numerical scheme and obtain the optimum number of particle distribution in the fluid domain. For the latter case, the time series of the free-surface elevation and velocity components close to free-surface are verified with the theoretical results of 2^{nd} order Stokes waves.

After validation and verification studies of the proposed WCSPH scheme through comparing the free-surface deformations inside the OWC chamber, a simulation matrix created by varying the geometrical parameters of chamber length and front wall draft has been run in three different wave conditions to find out the geometrical configuration that gives the best EEI values. Finally, to further improve the OWC device wave energy production capacity of the optimal configuration, simulation results with chamfered corners are presented.

5.3.1 Validation and Verification Studies for the OWC Simulations

A systematical investigation on the evaluation of the performance of OWC type WECs is carried out to determine the geometry that produces the largest energy under same wave conditions. As a first step, the validation of the numerical scheme proposed in this study is examined through measuring the free surface time series in the middle of an OWC device are compared with the experimental and time-domain results given in the literature [47]. Iturrioz et al. [47] presented a simplified time-domain model for a stationary OWC. In this model, the Cummins integro-differential equation is utilized to express the motion of a floating body.

To examine the particle size independence of the proposed algorithm, a convergence study is also carried out with five different particle resolutions. Furthermore, the accuracy of the numerical simulation results is measured using the root mean square error (RMSE) to make a quantitative comparison between the performances of particle resolutions, defined as:

$$RMSE = \sqrt{\frac{1}{N}\sum_{\mathbf{i}}^{N}\left(\zeta_{\mathbf{n},\mathbf{i}} - \zeta_{\mathbf{e},\mathbf{i}}\right)^2}, \tag{5.8}$$

where $\zeta_{\mathbf{n},\mathbf{i}}$ and $\zeta_{\mathbf{e},\mathbf{i}}$ represent the water surface elevation inside the OWC chamber for any ith sample of the numerical and experimental results, respectively, and N is the number of samples for each simulation.

Fig.5.4 displays the comparative graph of the numerical simulations with variable particle resolutions, while Table 5.1 indicates the RMSE values, computational performances of each cases. One can say that SPH results of the present study can capture the overall wave characteristics inside the OWC chamber in all resolutions and produces compatible free surface profiles with experimental results with the increasing particle resolutions. It can also be stated that SPH predicts the nonlinear characteristics of the wave trough deformations inside the chamber better than the time domain model solution.

In the light of the obtained RMSE values, it can be said that there is no significant difference between $d/40$ and $d/50$ resolutions. On the other hand, using $d/60$ resolutions results in a significant increase in computational costs. The $d/40$ resolution is still accurate enough to compare with experimental data without increasing the particle number and computation time. Following the observations and outcomes of the convergence study, $d/40$ particle resolution is utilized in all simulations of this work.

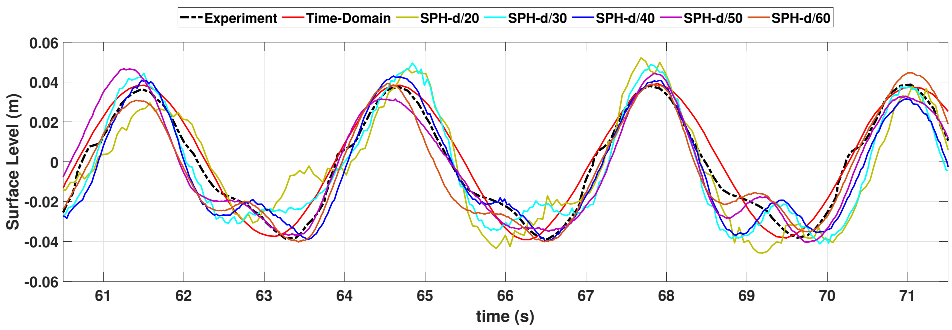

Figure 5.4 Comparison of free surface elevation time series of the present SPH results with those of time-domain and experimental findings of [47].

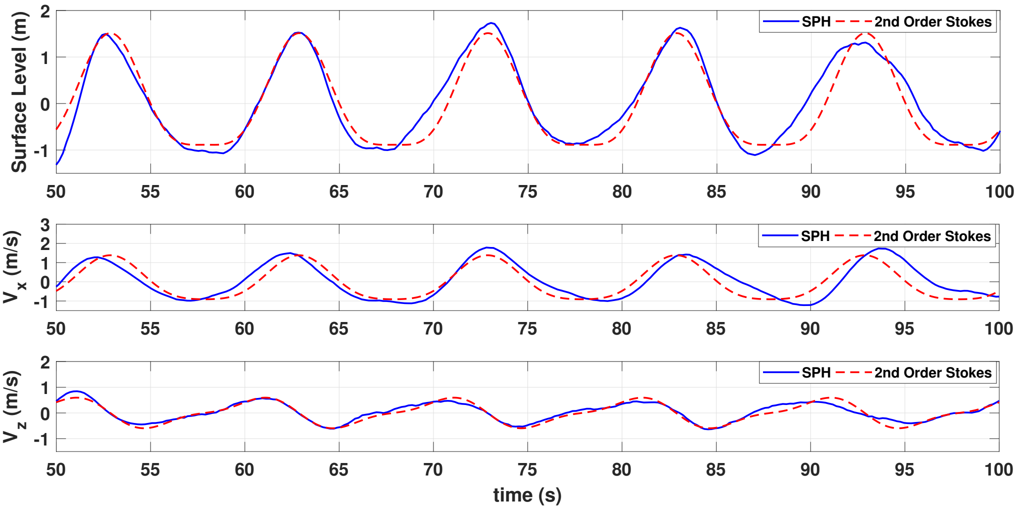

Figure 5.5 Comparison of SPH numerical and theoretical (2^{nd} order Stokes) wave surface elevation and orbital velocities with ($T = 10s$, $H = 2.4m$ and $d = 10m$) at $x = 55m$ and $z = -3m$.

Table 5.1 RMSE comparison between the free surface elevation measured in the experiment and calculated by the SPH simulations.

Particle Resolutions [m]	RMSE [m]	Iteration per second	Performance (hours/s)
d/20	0.0134	5.223	0.274
d/30	0.0112	1.579	1.407
d/40	0.0086	0.616	4.797
d/50	0.0084	0.252	14.24
d/60	0.0070	0.146	30.35

To verify the characteristics of generated waves in the numerical OWC tank, the wave kinematic quantities, namely, the free-surface elevation and orbital velocities at $x = 55[m]$ and $z = -3[m]$ are compared with the Stokes 2^{nd} order wave theory [19]. As can be seen from the time-series given in Fig.5.5, the generated waves in the numerical wave tank are in good match with the theoretical wave characteristics.

5.3.2 Performance Assessment of Chamber Length and Front Wall Draft

Configurations

Recollect that investigating the effect of geometry configurations and wave conditions on the efficiency of the stationary OWC type wave energy converters constitutes the main objective of this study. In this context, a 3-by-3 simulation matrix has been created based on the variation of the characteristic lengths of the system, namely, chamber length (w) and front wall draft (y). Additionally, whole simulation matrix has been run for three different wave period conditions at each geometrical configuration. It may be convenient to recall that second-order Stokes waves are generated in all OWC device simulations and wave heights are set to a constant value of 2.5[m] to reduce the complexity of the comparison. In all cases, the simulations are carried out for 150 seconds.

The obtained EEI results for all geometry configurations and wave conditions are presented in Table 5.2. It can be seen that the anterior wall immersion depth may have a significant effect on OWC efficiency for the wave period $T = 6[s]$ where the EEI values drops dramatically with the increasing draft values. In the cases of wave period $T = 8[s]$, the EEI values highly depends on both geometry parameters, where it can be deduced that there is a tendency of decreasing efficiency with higher draft sizes. In contrast, the simulation results of the wave conditions with $T = 10[s]$, the increase in chamber length and draft values generally leads to a positive effect on the wave energy efficiencies except the maximum values of both parameters. The comparative analysis on the results of all test cases indicates that the amount of the harvested wave energy highly depends on the OWC geometry for each particular wave conditions and the collected energy may be increased by the appropriate design of OWC geometry according to the dominating wave characteristics of the region. If the utilized regular wave periods are considered, it can be clearly inferred that these OWC geometries can be a good candidate for a coastal region with the peak wave period of $T = 8[s]$ and average wave height of $H = 2.5[m]$, where the maximum EEI values are achieved for nearly all geometrical configurations.

Table 5.2 Obtained EEI values for each OWC geometries and wave periods

Wave Period		**T=6s**			**T=8s**			**T=10s**		
Chamber Length		**2.3 m**	**3.3 m**	**4.3 m**	**2.3 m**	**3.3 m**	**4.3 m**	**2.3 m**	**3.3 m**	**4.3 m**
draft	**3.0 m**	0.094	0.039	0.012	0.090	0.117	0.077	0.011	0.019	0.029
	4.0 m	0.022	0.008	0.005	0.097	0.075	0.059	0.012	0.021	0.034
	5.0 m	0.006	0.004	0.002	0.087	0.051	0.029	0.021	0.028	0.025

To provide further details for the EEI calculations of all geometries, the time series of free-surface elevation, velocity and air pressure inside the chamber are plotted in Fig.5.6. As can be seen in Fig.5.6, an increase in the front wall draft of the OWC for a fixed chamber length generally results in a decrease in the EEI index due to a decrease in the surface velocity of the water and the air pressure in the chamber. For a fixed front wall draft, a decrease in chamber length generally results in an increase in surface velocity and air pressure in the OWC chamber, leading to an increase in EEI index.

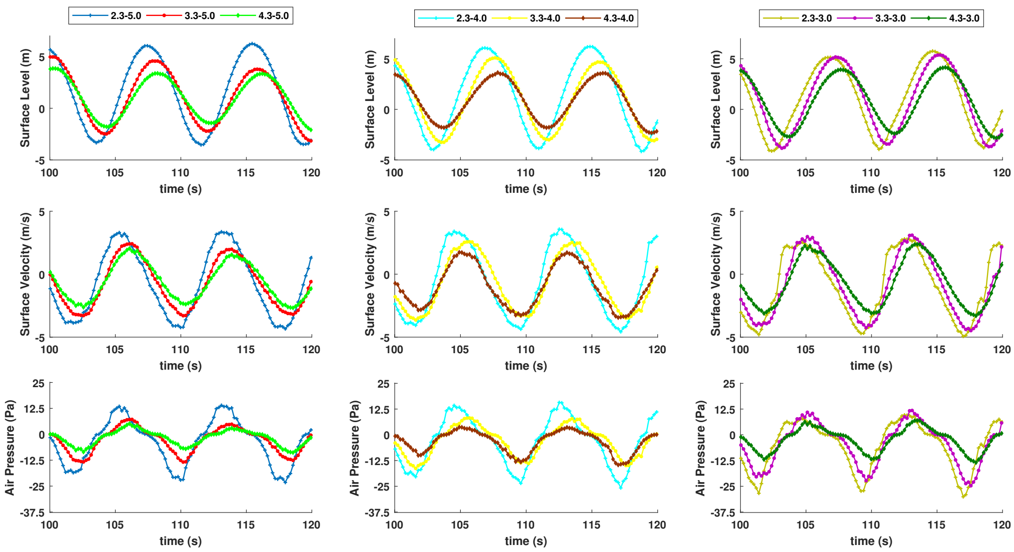

Figure 5.6 Time series of water surface elevation (top), velocity (center), and air pressure drop (bottom) within the OWC chamber for a propagating wave with $T = 8s$.

5.3.3 Effect of the Corner Chamfering on the Energy Effeciency

Having determined the chamber geometry configuration and wave condition that yields the maximum EEI value, a systematical investigation on this chamber geometry and wave characteristic is performed to seek for further improvement in the total efficiency by only chamfering the corners inside the OWC channel. Thus, seven additional geometry configurations (see Fig.5.3) are created wherefore the dimensional details are described in Table 5.3 together with the best geometry of the previous analyses.

Table 5.3 OWC geometry variations and measured hydrodynamic efficiency for each of them (Base model, $T = 8s$, $y = 3.0m$, and $w = 3.3m$).

Cases	**A1** [m]	**B1** [m]	**A2** [m]	**B2** [m]	**A3** [m]	**B3** [m]	**EEI**	**Vorticity** [-]
1	0	0	0	0	0	0	0.117	63.96
2	1	1	0	0	0	0	0.106	67.02
3	0	0	1	1	0	0	0.122	63.21
4	0	0	0	0	1	1	0.105	67.24
5	1	1	1	1	0	0	0.115	64.15
6	1	1	0	0	1	1	0.109	65.36
7	0	0	1	1	1	1	0.121	63.75
8	1	1	1	1	1	1	0.113	65.28

As can be seen in Table 5.3, all simulation cases except for cases 3 and 7 cause a drop in the OWC efficiency compared to case 1 (base model). Modifying the channel walls' geometry to cases 3 and 7 leads to an increase in efficiency by 3.4 and 4.3 percents, respectively. The possible reason that lies behind this improvement is considered to be related to the amount of vorticity levels. To extract the vortical characteristics in all geometry configurations, a strategy for the objective quantification of vorticities is proposed. According to this strategy, a correlation between the amount of vorticity generated inside the common region for all geometries (shown as blue in Fig.5.3) and the EEI has been established. The absolute amount of dimensionless vorticity ($\omega^* = \omega(\lambda/g)^{0.5}$ with λ denoting the wave length) is averaged over the total simulation time. To extract this correlation and represent the results in a succinct manner, the dimensionless vorticity and EEI values of each test cases are plotted in sequential order in Fig.5.7. It is numerically proven that EEI values are improving with the decrease in vorticity levels, which is actually an achievement of proper chamfers applied in the OWC chamber geometry.

Fig.5.8 presents the vorticity fields of test cases with maximum and minimum EEI values whereby one can clearly realize that the magnitude of the vorticity field is smaller for the case with the maximum EEI value. This observation can be attributed to the fact that the vorticity inherently leads to energy dissipation. The chamfering hampers the formation of vorticity through providing a streamlined flow pattern and larger space for fluid flow. The comparison of test cases 3 and 7 reveals that they have nearly identical EEI and vorticity values, which suggests that the chamfer formed by the dimensional factors of A3-B3 pairs does not have a notable influence on the EEI and vorticity magnitude. In all simulations, it is observed the existence of the chamfer defined by the geometrical factor of A1-B1 pair reduces the EEI value.

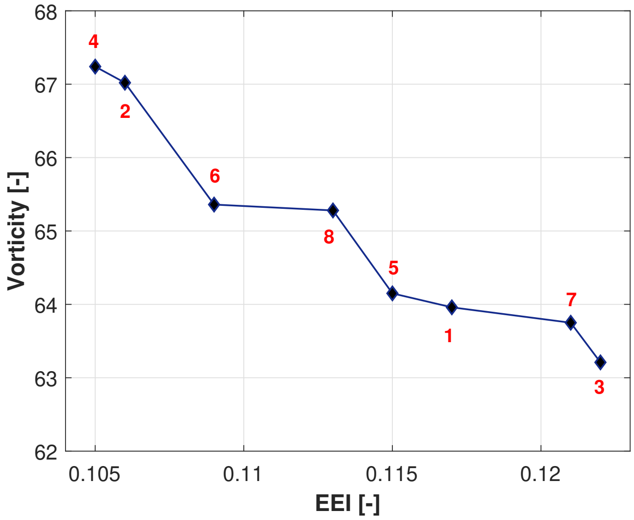

Figure 5.7 Comparison between efficiency and amount of vorticity recorded within the OWC chamber for different sloping wall configurations ($T = 8s$, $y = 3.0m$, and $w = 3.3m$).

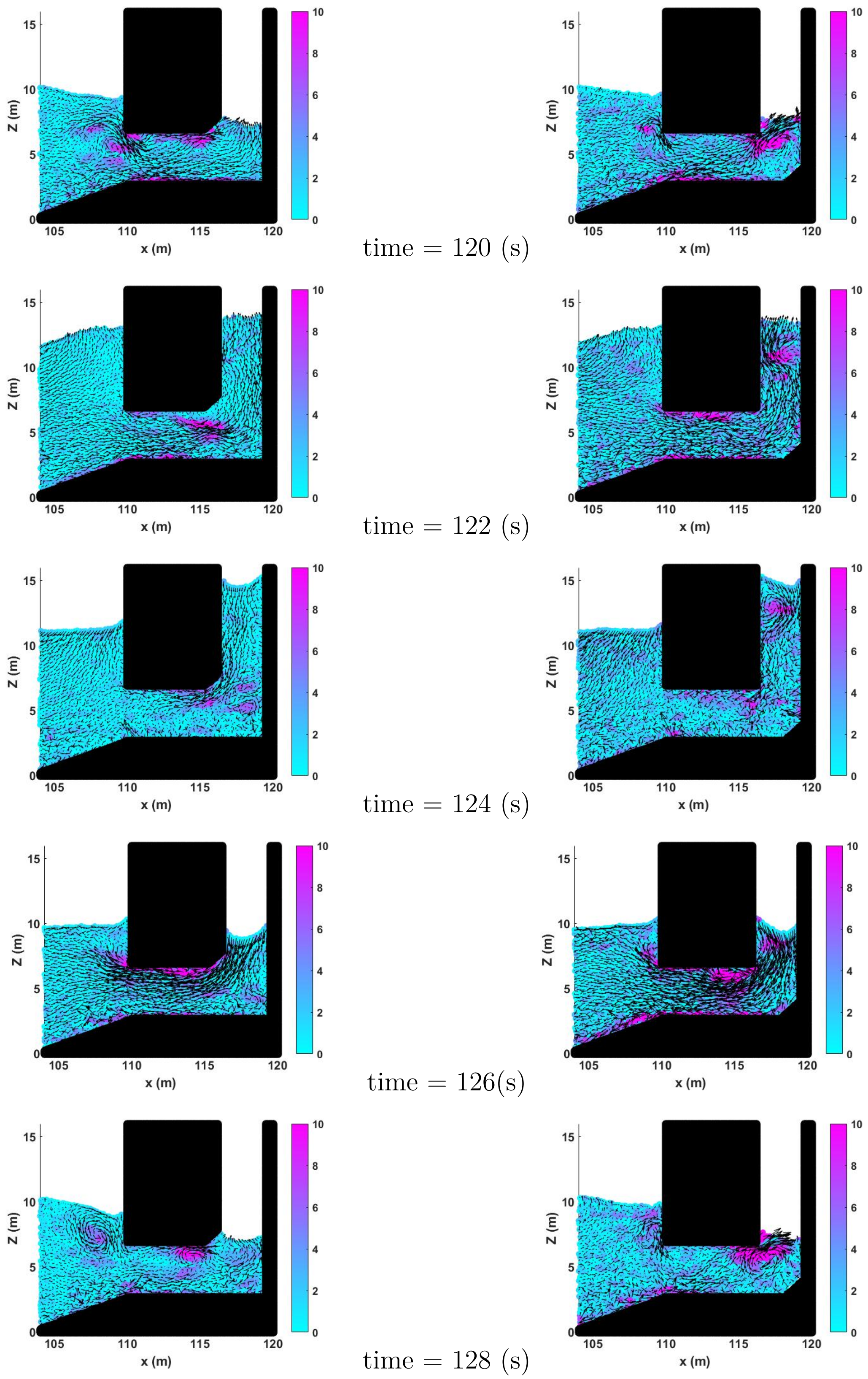

Figure 5.8 Instantaneous vorticity field and velocity vector representations of test cases with maximum (case 3, left) and minimum (case 4, right) EEI values for a full period of motion.

One can easily observe that there is an inverse relationship between the energy efficiency and the amount of vorticity inside the determined region. Using the chamfer configuration of cases 3 and 7 result lower vortex flow characteristics in the blue region (Fig.5.3), hence, leads to lower energy losses in the OWC system. Especially, the chamfer on the back wall of the chamber encourages more streamlined flow along the vertical direction and enhances the free-surface velocity and the air pressure inside the chamber which can be seen in the time series graphs given in Fig.5.9.

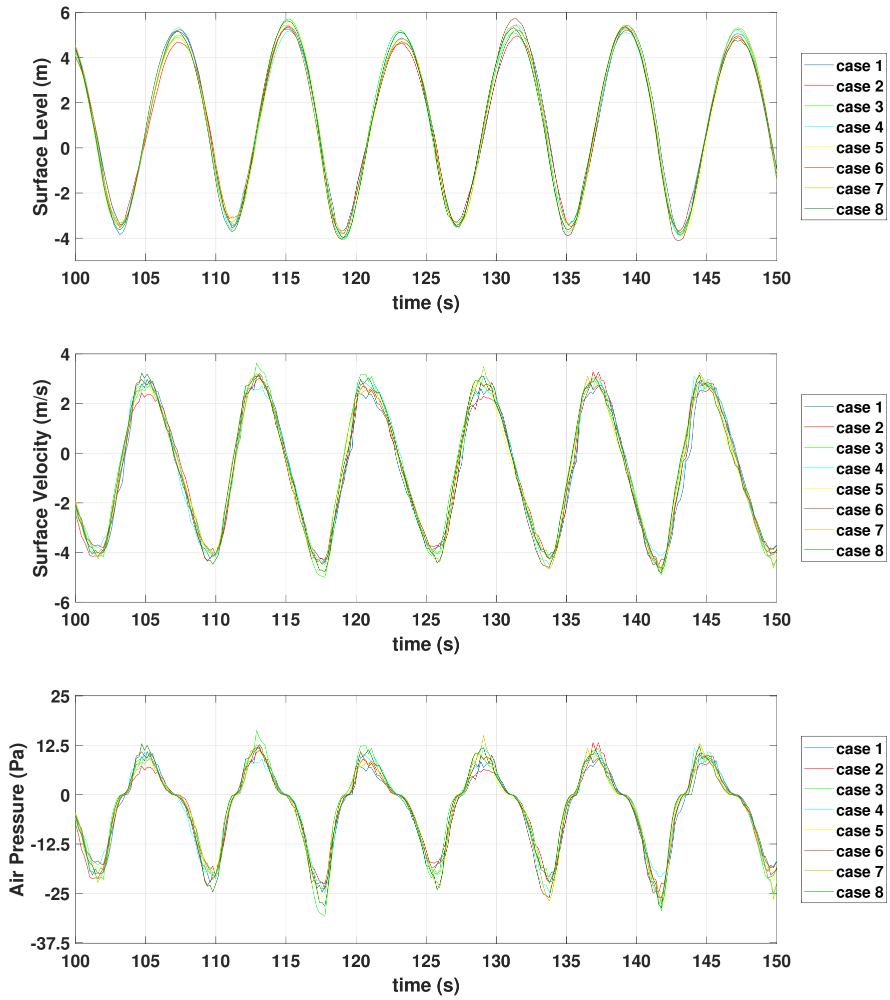

Figure 5.9 Time series of free-surface elevation (top), velocity (center), and air pressure drop (bottom) within the OWC chamber for different chamfer configurations ($T = 8s$, $y = 3.0m$ and, $w = 3.3m$).

The working performance of the best geometrical configuration (test case 3) has also been evaluated for the wave periods of $T = 6$, 8, and 10 seconds. Achieved efficiencies are tabulated and compared with the findings of base geometry in Table 5.4. As can be seen from the table, modifying the channel walls' geometry to case number 3 leads to an increase in efficiency in all wave conditions, where the amount of increase depends on the incident wave characteristics. Fig.5.10 displays the time series of free-surface elevations, velocities, and air pressure in the chamber for all simulated wave periods.

When considering the whole OWC device simulation results, it can be claimed that utilizing the obtained chamber length and draft dimensions together with implying the chamfer modifications of test case 3 can be a good candidate for a coastal region with the peak wave period of $T = 8[s]$ and characteristic wave height of $H = 2.5[m]$.

Table 5.4 Comparison of EEI values for the base geometry and the best performance geometry configuration (case 3) at each wave period.

Cases	**T=6** [s]	**T=8** [s]	**T=10** [s]
Base Geometry	0.039	0.117	0.019
Optimized Geometry	0.054	0.122	0.020

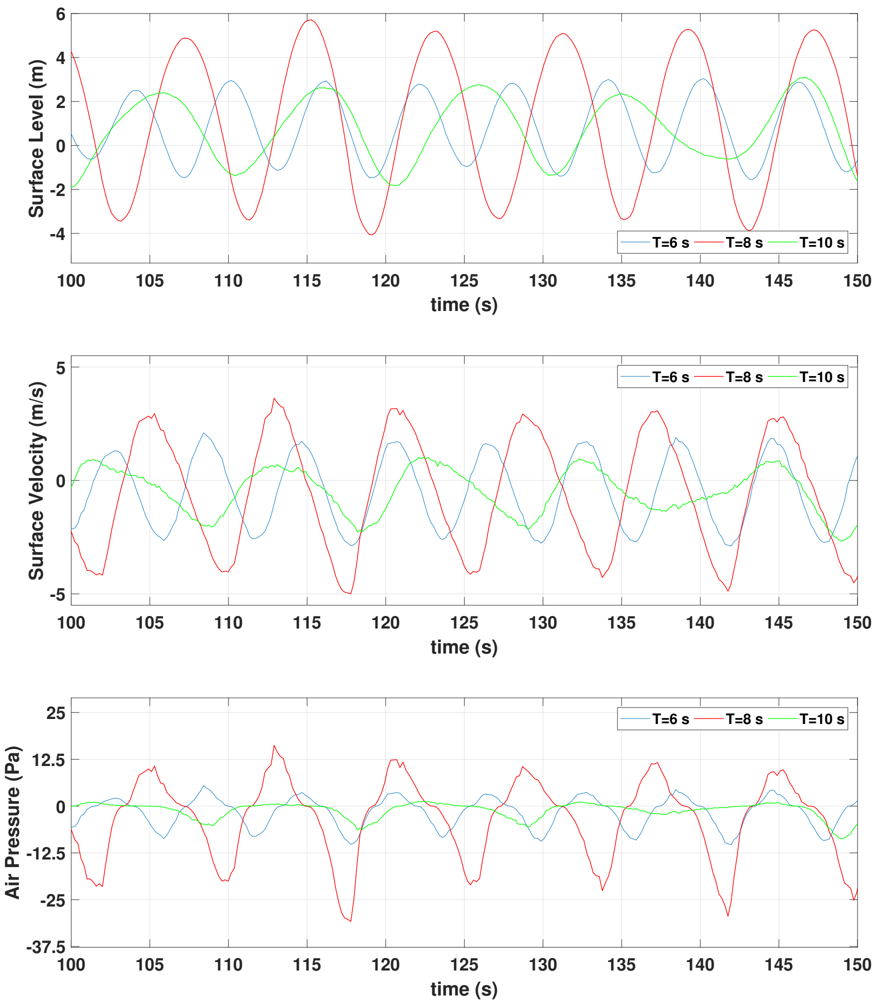

Figure 5.10 Time series of free-surface elevation (top), velocity (center), and air pressure drop (bottom) inside the OWC chamber for the best performance geometry configuration (case 3) at each wave period.

5.4 Conclusions

The search for possible energy efficiency enhancement in OWC type WECs under the same wave conditions comprises the main objective of this study. Weakly Compressible SPH approach is employed to investigate the hydrodynamic characteristics and the energy efficiency of OWC type wave energy converter system. Numerical simulations are performed in a two-dimensional numerical wave tank, that generates regular waves using a flap-type moving boundary.

As an initial validation study, the numerical performance of the proposed SPH scheme is examined by comparing the free-surface elevation in the middle of the OWC device with experimental and time-domain method results of Iturrioz et al. [47]. To investigate the particle size independence of the numerical scheme and obtain the optimum particle size, a convergence study is conducted, where the accuracy of the numerical results is assessed by comparing the root mean square error with experimental results. The outcomes of these simulations prove that the proposed SPH scheme can capture the free surface time series given by the experimental and time-domain method study of [47]. Secondly, the free-surface elevation and the orbital velocity time series of the proposed SPH scheme are compared with the theoretical 2^{nd} order Stokes wave theory findings, where highly compatible results are observed.

Following the validation of the numerical method for the utilized OWC geometry, a two-step efficiency enhancement study is conducted through systematical geometry modifications. In the first step, the chamber length and front wall draft has been varied to obtain the best geometry that leads to maximum harvested energy in three different wave periods. After determining the geometrical configuration that gives the maximum efficiency, the second step geometry modification has been carried out on the optimal geometry of the first step. A simulation matrix that consists of the combinations of chamfered corner regions of the OWC chamber has been run and it is observed that the energy efficiency of the OWC geometry can be still improved by 4.3%. Furthermore, the enhanced OWC geometry configuration, also harvests more wave energy in different wave conditions with respect to the base geometry, which has no chamfering at the corners. As a final investigation, a quantified relationship between the time-averaged vorticity inside the chamber region and the energy efficiency has been built. The vorticity analyses inside the chamber region indicate that reducing the vorticity magnitudes results in the higher total energy efficiency of the device, which is an expected outcome of energy conservation laws in physics.

To summarize and make an overall assessment of all test cases, the potential of the harvested wave energy highly depends on the OWC geometry for each particular wave condition, and the collected energy may be increased by the appropriate design of OWC geometry according to the dominating wave climates of the region. Nonetheless, the inspection of the effect of the water depth is not included in the limelight of this study. As trials at different water depths will lead to different oscillation characteristics of the free surface inside the chamber, it may be beneficial to extend the comprehensiveness of this study under various water depths and wave characteristics in future studies.

6. Comprehensive Numerical Study on the Behavior of Floating Structures under Challenging Ocean Conditions using WCSPH

This paper presents a comprehensive study that utilizes Smoothed Particle Hydrodynamics (SPH) simulations to analyze the behavior of floating structures under certain wave conditions. This work is constructed upon the achievement of five sub-steps. The first step focuses on ensuring the accuracy of the generated wave characteristics. Then, heave motion of a point-absorber wave energy converter is studied to examine the validity of rigid body motion modeling under regular wave conditions together with having different Power Take-Off (PTO) damping coefficients. Determining the validity of the model in a motion with single degree of freedom, free roll motion of a rectangular floating body is examined through comparing the natural frequencies and damping coefficients with available literature data. After having highly accurate results in free roll motion, roll motion of a fixed floating structure under a wide-range regular wave system is simulated to obtain corresponding Respond Amplitude Operators (RAOs). And finally, free body motion of a floating body under regular wave excitation condition is investigated considering all kinematic and dynamic aspects of the problem. By providing valuable insights into the behavior of floating structures, it can be said that this study contributes to the development of effective and sustainable offshore structures.

6.1 Introduction

The growing interest in renewable energy sources has led to extensive research into innovative solutions. Due to its high potential, reliability, and predictability, wave energy has emerged as a promising candidate gaining widespread attention in the scientific community. Despite several advancements in this field, only a few wave energy systems are currently generating electricity commercially [3]. Among these systems, the point-absorber, which involves a floating device that captures the oscillating motion of waves (heaving and/or pitching) and converts it into electricity through a PTO system [24] is one of the most widely used devices for wave energy conversion.

Point absorber wave energy converters (PAWECs) have become a leading area of research due to their versatility and straightforward design. To enhance the amount of energy extraction from ocean waves, it is crucial to develop accurate and reliable mathematical models requiring the solution of fluid-structure interaction (FSI) problems. FSI problems involve the complex interplay between moving or deforming structures and the surrounding or internal fluid flow [115]. They have various engineering applications such as the impact of waves on coastal structures, aeroelasticity of aircraft wings, and sloshing phenomena in LNG tanks [54, 49, 127].

In recent years, a multitude of numerical methods have been proposed to model FSI problems [32, 53, 62, 40]. These methods can be broadly classified into mesh-based and particle-based techniques. Mesh-based approaches, such as the Finite Element Method (FEM) [129], Finite Difference Method (FDM) [31], and Finite Volume Method (FVM) [119], are widely employed. However, due to their grid-based nature, these methods often encounter difficulties in updating meshes and capturing solid-fluid interface deformations, especially during abrupt and significant surface deformations of fluid motion [127].

Lagrangian particle-based methods, such as Smoothed Particle Hydrodynamics, Moving Particle Semi-implicit Method (MPS), Peridynamics and Discrete Element Method (DEM), are particularly suitable for simulating free-surface flows and interactions with highly deformable structures [79]. Meshless techniques have garnered substantial attention for their ability to yield highly accurate results in FSI simulations [45, 115, 53, 40]. Fully-Lagrangian mesh-free FSI solvers have been utilized in various studies. For instance, Yang et al. [125] coupled SPH and Element Bending Group (EBG) methods to investigate the impact of dam-breaking flow on an elastic structure, whereas Rahimi et al. [89] introduced the Arbitrary Lagrangian-Eulerian (ALE) method as a hybrid approach to address FSI problems. This method combines SPH and Peridynamics to simulate fluid behavior and solid structure behavior, respectively. Additionally, the authors proposed a novel Lagrangian mapping technique to accurately capture interfacial displacements in their approach. He et al. [40] employed a combination of weakly compressible SPH and total Lagrangian SPH to study hydroelastic FSI problems. Khayyer et al. [53] proposed an ISPH-SPH hydroelastic FSI method, validated through several classical and ocean engineering benchmark tests. Tofighi et al. [116] present a two-dimensional SPH scheme for simulating rigid body motion in Newtonian fluids. Assuming the structural deformations are negligible, their approach combines rigidity constraints, the viscous penalty method, and evaluates various viscosity ratios and interpolation schemes. The proposed method accurately captures the motion of rigid bodies driven by flow or external forces, as demonstrated through systematic testing in different scenarios. Ozbulut et al. [82] conducted a comprehensive investigation into the nonlinear effects present in the enforced roll motion of a 2-D rigid body in the free surface through the utilization of the SPH method. By employing their in-house code, they successfully disclosed inherent nonlinearities in the roll motion, while also providing insights into hydrodynamic coefficients, damping coefficients, and vortex flow characteristics.

In this research study, we undertake an investigation of various FSI problems using our in-house Weakly Compressible Smoothed Particle Hydrodynamics (WCSPH) numerical code. SPH is a widely used particle-based numerical method introduced by Monaghan et al. in 1977 [35]. It discretizes the computational domain using particles, each carrying its own physical properties [35]. SPH excels in modeling highly nonlinear free-surface problems and finds extensive application in various complex engineering scenarios such as free-surface flows [86, 83, 75, 91], dam-break simulations [92, 125], sloshing motion [104], and rigid body motion [114]. The obtained results of the present work are compared with the existing experimental and theoretical findings documented in relevant scientific literature. To ensure the reliability of the generated numerical wave flumes, the time series of free surface elevations and orbital velocities are compared with those of 2^{nd} order Stokes theory results [19]. Following the verification of the results and the determination of the optimum particle size for the tackled problem sets of the present study, the heave displacement and vertical velocity of a point-absorber wave energy converter device under regular wave excitation is simulated. Additionally, the converter's efficiency is calculated for different PTO damping coefficients. The achieved numerical outcomes from the SPH simulations are compared with experimental data from the literature [126] for three distinct PTO constants, allowing for a comprehensive evaluation and validation of the model. The third part of the study focuses on investigating the free roll motion of a hinged rectangular structure. The natural frequency and damping ratio of the floating structure are determined which will be required in the analysis of next steps. In the fourth problem, the relationship between Response Amplitude Operators (RAOs), wave frequencies, and steepness is examined. As a further examination of the proposed numerical scheme, roll motion of a floating body excited in a wide range of wave frequencies are investigated to obtain corresponding RAO values. Finally, we compare the obtained results with the experimental data

[48]. Finally, the coupled surge, heave, and pitch motions of a freely floating body is investigated in regular wave conditions. To assess the accuracy and reliability of the SPH method in modeling the motion of the floating box, we compared our numerical results with the experimental time series data from Ren et al. [96].

To assess the reliability, coherence, and precision of our numerical approach, we conduct a comparative analysis with experimental and theoretical findings documented in existing literature for each individual problem. Root mean square error (RMSE) values are calculated for each problem, and the results are compared to determine the optimal interparticle distances. Through the comparison of numerical and experimental results, we aim to identify the strengths and limitations of our SPH method in modeling non-deformable FSI problems, as well as suggest areas for further improvement and research.

The findings of this study provide valuable insights into the performance of floating systems under various wave conditions and contribute to the design and optimization of similar structures for wave energy conversion. Through the comparison of numerical and experimental results, we can identify both the strengths and limitations of our SPH code in accurately modeling the motion of floating systems under various regular wave conditions. These analyses also point towards potential areas for further improvement and future research in this field.

The paper is organized as follows: Section 2 presents an overview of the governing equations and their discretized form using the proposed WCSPH approach. It includes equations for modeling the motion of floating bodies and mathematical formulas for modeling and absorbing numerical waves, as well as equations for calculating the efficiency of the wave energy converter device. Section 3 focuses on defining the physical and geometrical parameters of the five investigated problems. In this section, we examine the robustness, consistency, and accuracy of the numerical method by comparing our findings with the available experimental and theoretical studies of the literature. The last section presents the concluding remarks and discussions on the obtained results.

6.1.1 Modeling of Dynamic Floating Body Motion

The one-way coupling between fluid and solid has been represented using the viscous penalty approach, which has been previously validated in a study on the motions of rigid bodies in fluids [116]. In this approach, a color function value, denoted as

$c_{\mathbf{i}}^{\alpha}$, is assigned to each phase. For particles belonging to the same phase, the color function value is set to one, while for particles in the other phase, it is set to zero. Subsequently, the color function is smoothed across phase boundaries, as described below:

$$\widehat{c_{\mathbf{i}}^{\alpha}} = V_{\mathbf{i}} \sum_{\mathbf{j}=1}^{N} c_{\mathbf{j}}^{\alpha} W_{\mathbf{ij}}, \tag{6.1}$$

In the study conducted by Tofighi et al. [116], it is demonstrated that employing a weighted harmonic mean for smoothing between boundaries yields more precise outcomes. Therefore, the same interpolation technique is employed, as presented below, where α, represents the phase of the particle:

$$\frac{1}{\phi_{\mathbf{i}}} = \sum_{\alpha} \frac{\widehat{c_{\mathbf{i}}^{\alpha}}}{\phi_{\mathbf{s}}} + \frac{\widehat{c_{\mathbf{i}}}}{\phi_{\mathbf{f}}}, \tag{6.2}$$

In this particular context, the subscripts "s" and "f" serve to differentiate between solid and fluid particles, respectively. The interpolation process for fluid properties, denoted as $\phi_{\mathbf{ij}}$, is conducted using the following equation [82]:

$$\phi_{\mathbf{ij}} = \frac{2\phi_{\mathbf{i}}\phi_{\mathbf{j}}}{\phi_{\mathbf{i}} + \phi_{\mathbf{j}}}, \tag{6.3}$$

In a broader context, the variable ϕ is capable of representing any fluid property. Prior studies have demonstrated that achieving satisfactory accuracy involves assigning a viscosity value for the solid phase that is 100 times greater than the fluid phase [116, 82].

The dynamic motion of floating body is determined through applying rigidity constraints based on conservation of linear and angular momentum [116] which has three separate steps. At first step, the floating body particles are considered as fluids with higher viscosity and their instantaneous velocities are calculated through entering the whole governing equation system for fluids. Then, the obtained instantaneous velocities are employed to calculate the translational and rotational velocity at the body center of mass as given in the following:

$$\mathbf{u}_s^t = \frac{1}{M_\mathbf{s}} \sum_{\mathbf{j}=1}^{N_s} \mathbf{u_j} V_\mathbf{j} W_\mathbf{ij}, \tag{6.4}$$

$$\mathbf{u}_s^r = \frac{1}{I_\mathbf{s}} \sum_{\mathbf{j}=1}^{N_s} (\mathbf{u_j} \times \mathbf{r_{js}}) V_\mathbf{j} W_\mathbf{ij}, \tag{6.5}$$

And finally, the individual velocities are assigned to each solid particle in accordance with rigid body motion principle:

$$\mathbf{u}_i = \mathbf{u}_s^t + \mathbf{u}_s^r \times \mathbf{r_{is}}. \tag{6.6}$$

In this context, the vector $\mathbf{r_{is}}$ is defined as the difference between the position vector $\mathbf{r}_i$ of a solid particle and the center of mass vector $\mathbf{r}_s$ of the solid object. N_s indicates the total number of particles in the solid phase. $M_\mathbf{s}$ represents the total mass of the rigid body, while $I_\mathbf{s}$ represents the moment of inertia of the rigid body about its center of mass.

$$M_\mathbf{s} = \sum_{\mathbf{j}=1}^{N_s} V_\mathbf{j} W_\mathbf{ij}, \tag{6.7}$$

$$I_\mathbf{s} = \sum_{\mathbf{j}=1}^{N_s} \mathbf{r_{js}}^2 V_\mathbf{j} W_\mathbf{ij}, \tag{6.8}$$

By combining the viscous penalty method with the rigidity constraint within the SPH framework, the particles are able to exhibit rigid behavior within the solid body due to the elevated viscosity.

6.1.2 Equations for Determining the Hydrodynamic Performance of

Point-Absorber Wave Energy Converter

In this section, we present the equations related to the hydrodynamic performance of the point-absorber wave energy converter. The power of wave per meter of the wavefront width, is calculated by formulation given by [28]:

$$J = \frac{1}{16}\rho g H^2 \frac{\omega}{k}(1 + \frac{2kd}{sinh(2kd)}). \tag{6.9}$$

The power captured by the wave energy converter (WEC) at any given instant is directly proportional to the damping force exerted by the power take-off system, which can be expressed as follows:

$$P_{abs}(t) = F_{PTO}(t)v_z(t) = b_{PTO}v_z^2(t). \tag{6.10}$$

The variable v_z represents the vertical velocity of the point absorber wave energy converter device, while b_{PTO} denotes the damping coefficient of the PTO system. The averaged power absorbed by the device:

$$P_a = \frac{1}{T}\int_{t_0}^{t_0+T} P_{abs}(t)dt, \tag{6.11}$$

The maximum absorbed power that can be theoretically obtained by a symmetrical body oscillating solely in heave can be computed using the following formula [80]:

$$P_{a,max} = \frac{J}{k}. \tag{6.12}$$

The WEC efficiency can be determined through calculating the ratio of averaged power and the theoretical maximum value:

$$\frac{P_a}{P_{a,max}} = 2\pi\frac{P_a}{J\lambda}. \tag{6.13}$$

In equation 6.13 the variable λ represents the wavelength of the incoming wave. The two parameters frequently employed to assess the effectiveness of a wave energy converter are the capture width (CW) and the capture width ratio (CWR). The capture width denotes the width of the wave front that the device fully captures, whereas the CWR corresponds to the proportion of the available power in the incident wave that the device absorbs. These metrics can be mathematically defined as follows:

$$CW = \frac{P_a}{J}, \tag{6.14}$$

$$CWR = \frac{P_a}{P_w}. \tag{6.15}$$

The capture width is expressed in meters, while the capture width ratio is a dimensionless parameter defined as the capture width divided by the device dimension perpendicular to wave propagation, which in this case is the buoy diameter D. Therefore, the energetic efficiency can also be characterized using the ratios CW/CW_{max} or CWR/CWR_{max}, since:

$$\frac{CWR}{CWR_{max}} = \frac{CW}{CW_{max}} = \frac{P_a}{P_{a,max}} = 2\pi\frac{P_a}{J\lambda}. \tag{6.16}$$

6.2 Results and Discussion

6.2.1 Modelling of Regular Ocean Waves

In this section, we will examine the accuracy levels in the generated wave characteristics through performed simulation results of regular ocean waves in a numerical wave tank. To begin, we will evaluate the validity of the proposed numerical method by comparing the wave kinematic variables, such as the free-surface elevation and the orbital velocities at a specific point ($x = 3.4[m]$ and $z = -0.2[m]$) with those predicted by the Stokes 2^{nd} order wave theory [19]. To ensure the verification of the proposed numerical scheme, a mesh-independency analyses will be also presented.

Figure 6.1 depicts the two-dimensional numerical wave tanks that are used to verify the accuracy of the produced regular waves. The simulations are conducted in a numerical wave flume that has a length of $\lambda = 4.75$ meters and a still water level of $d = 1.1$ meters. These simulations are targeting to produce 2^{nd} order Stokes regular waves with a period of $T = 1.5$ seconds and a wave height of $H = 0.16$ meters. In order to reduce the effect of reflected waves on the simulation results, a combination of numerical passive wave absorption system and a sloped beach (γ=1/2) on the right-hand side of the tank were utilized.

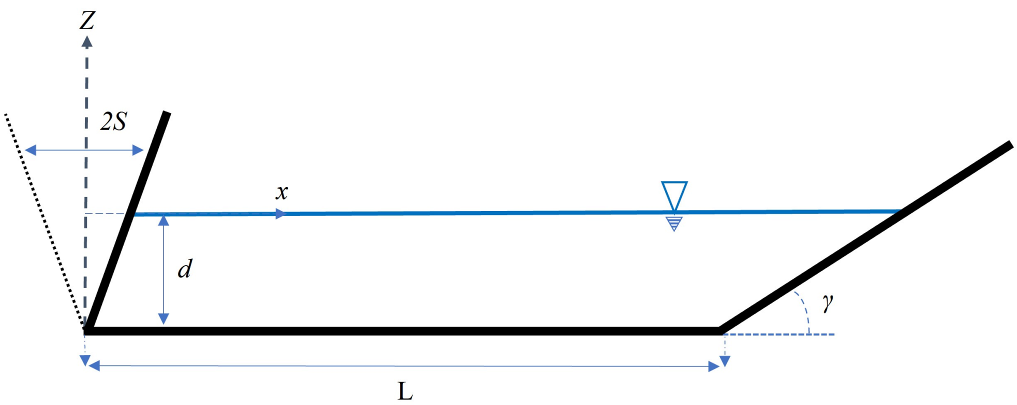

Figure 6.1 Schematic visualization of the computational domain for the verification model.

The time series of water surface elevation and orbital velocities of water particles at the defined location can be calculated based on the 2^{nd} order wave theory, as follows [19]:

$$\zeta_t = \frac{H}{2}cos(kx-\omega t) + \frac{H^2 k}{16}\frac{cosh(kd)}{sinh^3(kd)}(2+cosh(2kd))cos(2(kx-\omega t)), \tag{6.17}$$

$$V_x = \frac{H}{2}\frac{gk}{\omega}\frac{cosh(k(d+z))}{cosh(kd)}cos(kx-\omega t) + \frac{3}{16}\frac{H^2\omega k cosh(2k(d+z))}{sinh^4(kd)}cos(2(kx-\omega t)), \tag{6.18}$$

$$V_z = \frac{H}{2}\frac{gk}{\omega}\frac{sinh(k(d+z))}{cosh(kd)}sin(kx-\omega t) + \frac{3}{16}\frac{H^2\omega k sinh(2k(d+z))}{sinh^4(kd)}sin(2(kx-\omega t)). \tag{6.19}$$

The variables used in the equations are defined as follows: ζ_t represents the water surface elevation, while V_x and V_z denote the horizontal and vertical components of the orbital velocities of water particles, respectively.

The mesh-independency simulations are conducted with four different interparticle distances (dx=0.028 m, 0.020 m, 0.014 m and 0.010 m), and the corresponding results are presented in Figure 6.2. As can be seen from the graphs, the SPH results are converging to the 2^{nd} order wave theory as the particle refinement increases. Additionally, Table 6.1 provides detailed information on the computational performance and RMSE values for each case. This analysis helps us determine the appropriate mesh resolution required for accurate numerical simulations of the problem at hand. To quantify the convergence level, a root-mean-square error (RMSE) analysis is also performed. The RMSE is used as a metric to assess the accuracy of the numerical simulation outcomes and is expressed as follows:

$$RMSE = \sqrt{\frac{1}{N}\sum_{\mathbf{i}}^{N}\left(\zeta_{\mathbf{n},\mathbf{i}} - \zeta_{\mathbf{e},\mathbf{i}}\right)^2}, \tag{6.20}$$

Where N represents the number of data points in the comparison, which is equal to the maximum data amount among all the data sets being compared. $\zeta_{\mathbf{n},\mathbf{i}}$ denotes the numerical value of the ith data point, while $\zeta_{\mathbf{e},\mathbf{i}}$ represents the exact (or expected) value of the ith data point. The formula calculates the difference between the numerical and exact values for each data point. Table 6.1 provides detailed information on the computational performance and RMSE values for each case. This analysis helps us determine the appropriate particle resolution required for accurate numerical simulations of the problem at hand.

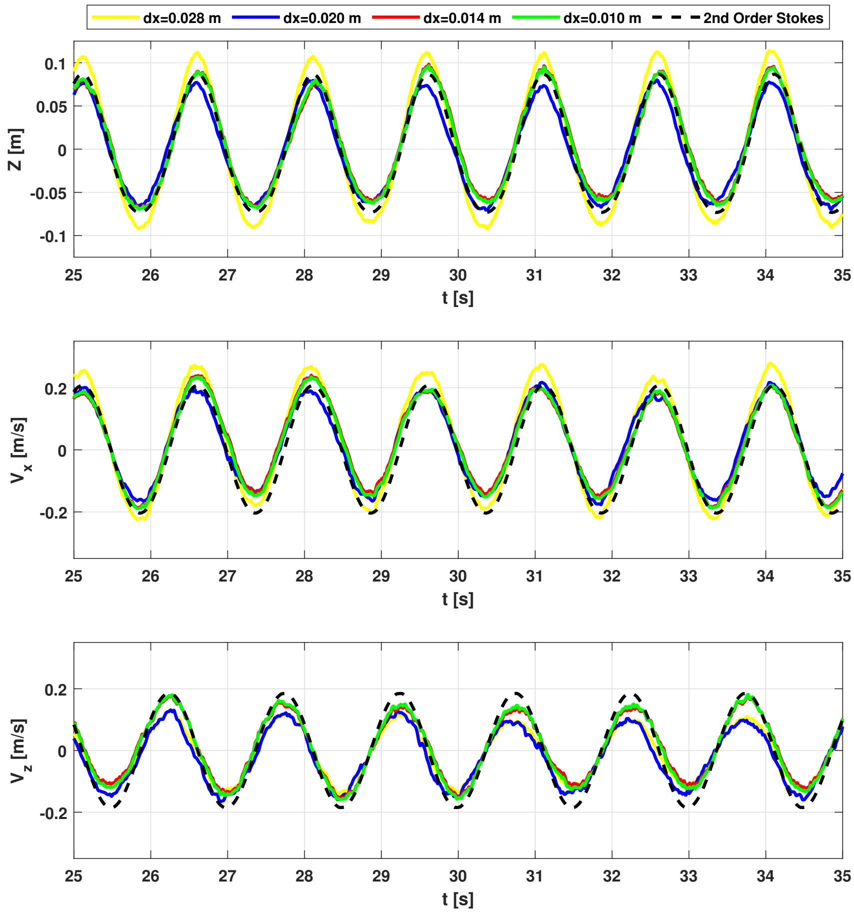

Figure 6.2 Comparison of numerical and theoretical (2$^{\text{nd}}$ order Stokes) wave surface elevation and orbital velocities for SPH at $T = 1.5$ s, $H = 0.16$ m, and $d = 1.1$ m, at location $x = 3.4$ m and depth $z = -0.2$ m.

Table 6.1 Comparison of RMSE values between the theoretical 2$^{\text{nd}}$ order stokes and SPH simulated free surface elevation.

Interparticle distances [m]	**RMSE [m]**
0.028	0.0136
0.020	0.0108
0.014	0.0104
0.010	0.0088

As expected, fine particle resolution leads to lower RMSE values in the expense of higher computational time costs. To determine the optimal particle resolution for modeling numerical regular waves within a reasonable computational time, a value of $dx = 0.014$ m was chosen. This analysis enables us to achieve a balance between accuracy and computational efficiency for the simulations. The overall results of this section have proven that the proposed numerical wave-making model can capture the kinematic wave characteristics of the desired wave conditions with a good accuracy. Therefore, this wave generator model has been employed in all simulations of the present work that requires wave generation.

6.2.2 Investigating the Behaviour of Point Absorber Wave Energy Converter in the Presence of Regular Waves

This section investigates the heave displacement and vertical velocity of a point-absorber wave energy converter device and compares the SPH results with experimental measurements found in the literature [126].

Figure 6.3 depicts the schematic view of the problem geometry. The modeled point-absorber is a cylindrical structure with a height of 0.22 m and a diameter of 0.50 m. The buoy has a density of 500 kg/m^3. The flap boundary is located at a still water depth of 1.1 m, and the length parameter L is set to 3.4 m. The beach slope, denoted as γ, is 1/2.

A single wave condition is investigated which is characterized by a wave period (T) of 1.5 s, a wave height (H) of 0.16 m, which corresponds to a wave length of 3.4 m.

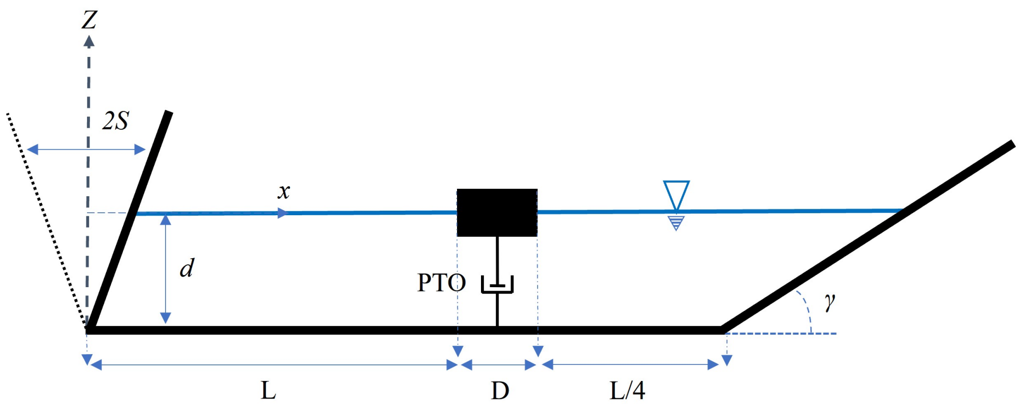

Figure 6.3 Schematic visualization of the computational domain for the point-absorber wave energy converter device.

Figure 6.4 compares the heave displacement and vertical velocity time series of the point-absorber at three different particle resolutions, while Table 6.2 provides an overview considering the RMSE values of each particle size. The table presents the RMSE values extracted from heave displacement and vertical velocity time series of the point-absorber device with the PTO damping value (b_{PTO})) of 240 Ns/m.

The results demonstrate a strong correlation between the numerical and experimental time series. Based on the RMSE values derived from the comparison of our simulation outcomes with experimental data from the literature [126], we determined that an initial particle spacing of 0.014 m produces well-matched outputs with experimental measurements at bearable computational time cost margins. Thereby, dx = 0.014 m is selected for all subsequent simulations.

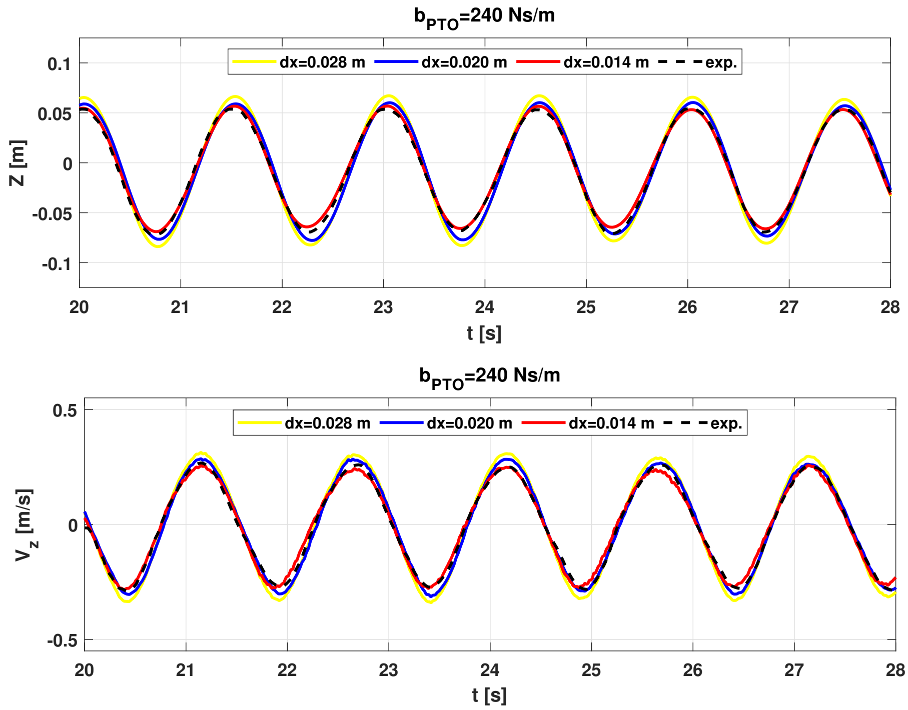

Figure 6.4 Comparison between experimental [126] and numerical time-series of heave displacement and vertical velocity for the point-absorber device with a PTO damping coefficient of 240 Ns/m.

Table 6.2 Comparison of RMSE Values between experimental [126] and SPH simulation results for heave displacement and vertical velocity at a damping coefficient of 240 Ns/m.

Interparticle distances [m]	**Z RMSE [m]**	**Vz RMSE [m/s]**
0.028	0.0091	0.0367
0.020	0.0062	0.0219
0.014	0.0030	0.0187

Subsequently, we conducted simulations to compare the heave displacement and vertical velocity of the point-absorber using different PTO damping coefficients (0 Ns/m, 240 Ns/m, and 1100 Ns/m). The results of these simulations are presented in Figures 6.5 and 6.6, which illustrate the comparison between the experimental and numerical time series of heave displacement and vertical velocity for the device at three distinct b_{PTO} values. The outcomes demonstrated very good agreement in terms of both amplitude and phase across all three cases.

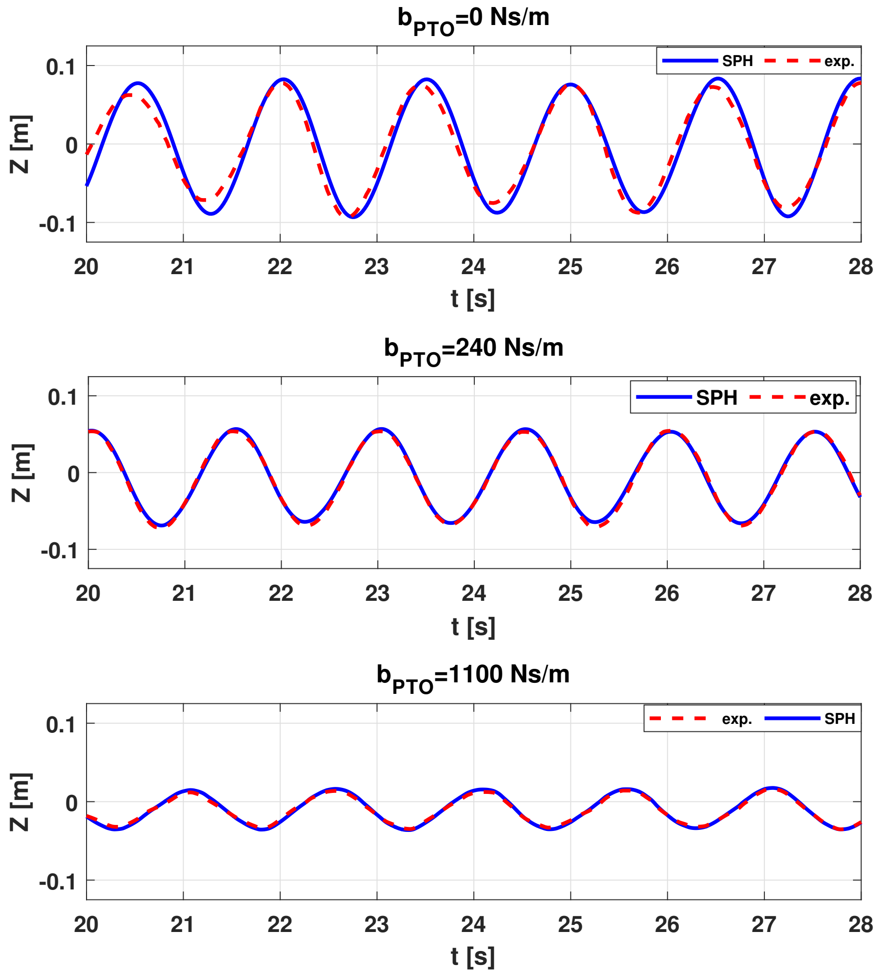

Figure 6.5 Comparison of experimental [126] and numerical time-series of heave displacement for the point-absorber with PTO damping coefficients of 0 Ns/m, 240 Ns/m, and 1100 Ns/m.

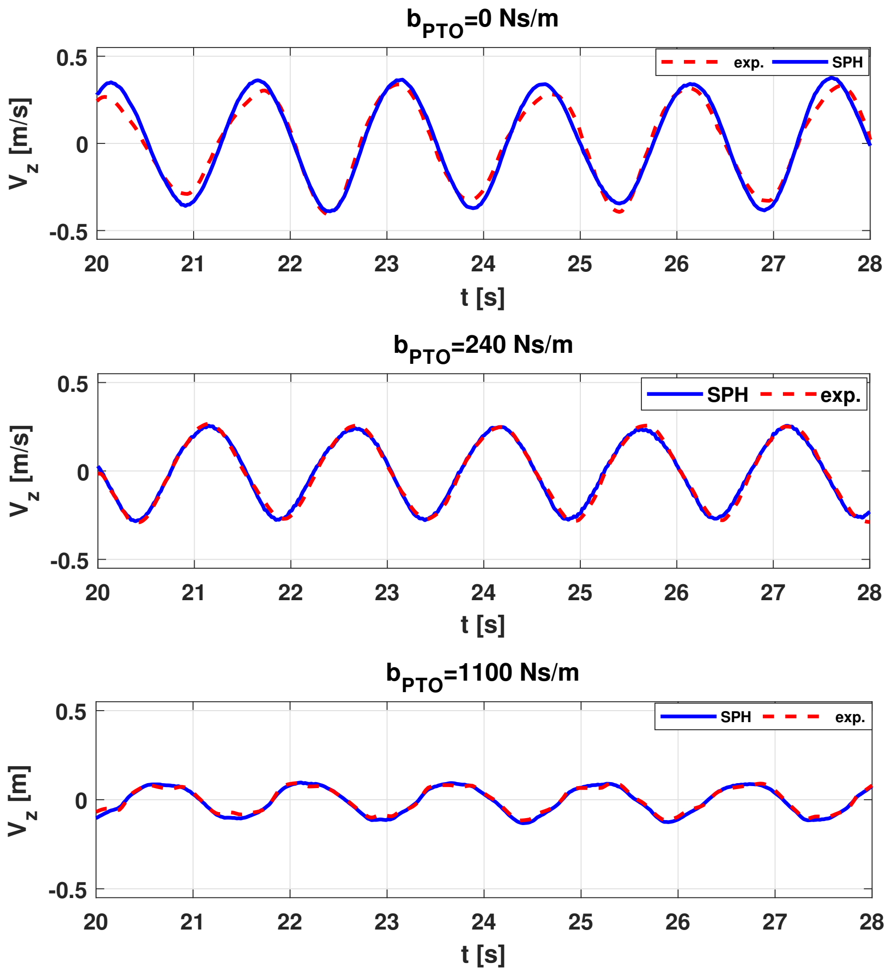

Figure 6.6 Comparison of numerical and experimental [126] time-series of vertical velocity for the point-absorber device with PTO damping coefficients of 0 Ns/m, 240 Ns/m, and 1100 Ns/m.

Table 6.3 provides a comprehensive comparison of the average power and efficiency for different values of b_{PTO} between our SPH simulations and experimental results. This comparison allows us to assess the agreement between the numerical predictions and the actual experimental measurements, providing valuable insights into the accuracy and reliability of our simulation approach.

When b_{PTO} is set to 240 Ns/m, the experimental average power is measured at 8.31 W/m, while the SPH simulation predicts a slightly lower value of 7.92 W/m. The efficiency for this configuration is found to be 0.38 for the experimental data and 0.36 for the SPH simulation.

For the highest value of b_{PTO} at 1100 Ns/m, the experimental average power is recorded as 5.15 W/m, while the SPH simulation yields a higher value of 7.52 W/m. The efficiency in this case is measured at 0.23 for the experimental data and 0.34 for the SPH simulation. Based on these results, it can be concluded that the SPH simulations generally demonstrate reasonably close agreement with the experimental data in terms of average power and efficiency for different values of b_{PTO}. While there are slight deviations observed between the experimental and simulated values, the overall trends and magnitudes are in good agreement. These findings reinforce the validity and accuracy of our numerical model in capturing the behavior of the wave energy converter under varying PTO damping coefficients.

Table 6.3 Comparison of Average Power and Efficiency for different values of b_{PTO} (Ns/m)

b_{PTO} (Ns/m)	240		1100	
	Exp.	**SPH**	**Exp.**	**SPH**
Average Power (W/m)	8.31	7.92	5.15	6.19
Efficiency (-)	0.38	0.36	0.23	0.28

The results of this study suggest that an increase in PTO damping leads to a decrease in both the maximum heave displacement and vertical velocity of the buoy, as illustrated in Figures 6.5 and 6.6. Specifically, when $b_{PTO} = 0$, which corresponds to structural damping alone, the maximum heave displacement approximates the incident wave height. In contrast, when $b_{PTO} = 1100$, the maximum heave displacement decreases to about one-third of the incident wave height. Even though the period remains the same as that of the incident waves, both the maximum heave displacement and velocity of the buoy decrease as PTO damping increases.

Therefore, this highlights the capability of our in-house code to accurately replicate the response of a point-absorber under regular waves for various PTO system configurations with a reasonable computational time. In conclusion, our study provides important insights into the behavior of a point-absorber WEC and demonstrates the accuracy and validity of our numerical model for simulating its performance. Our findings can be used to inform the design and optimization of point-absorber WECs for wave energy conversion.

6.2.3 Analysis of Rolling Motion for a Floating Box in Calm Water Conditions

After conducting a comprehensive investigation and validation of our code's capability to simulate wave-making and the interaction between free surface waves and the heave motion of a floating box, we now intend to further improve its quality.

Specifically, we will validate our SPH model's accuracy in simulating the free roll motion of a rectangular floating structure with a free surface.

To achieve this, we will compare our model's predictions with the experimental results reported by Jung et al. [48]. Once we successfully validate and calibrate our model, we can utilize it to assess the impact of various sea states and floating structure geometries on roll motion. This will allow us to gain a better understanding of the behavior of such structures under different conditions and inform future design decisions.

To replicate the experimental setup of Jung et al. [48], we designed a two-dimensional numerical wave tank. The rectangular structure under consideration had one degree of freedom, hinged at its center of gravity, and was initially inclined and released at an angle of 15 degrees. The structure had a width of 0.3 m, a height of 0.1 m, and a mass moment of inertia of 0.36 kg m^2.

To ensure the accuracy of our numerical model, we discretized the tank using three different interparticle distances: 0.020 m, 0.014 m, and 0.010 m. Additionally, sponge layers were incorporated on both sides of the tank to mitigate the effects of reflected waves, which could potentially impact the accuracy of the measured roll angles due to the body's oscillation. Figure 6.7 provides a detailed illustration of the numerical wave tank used in the simulation.

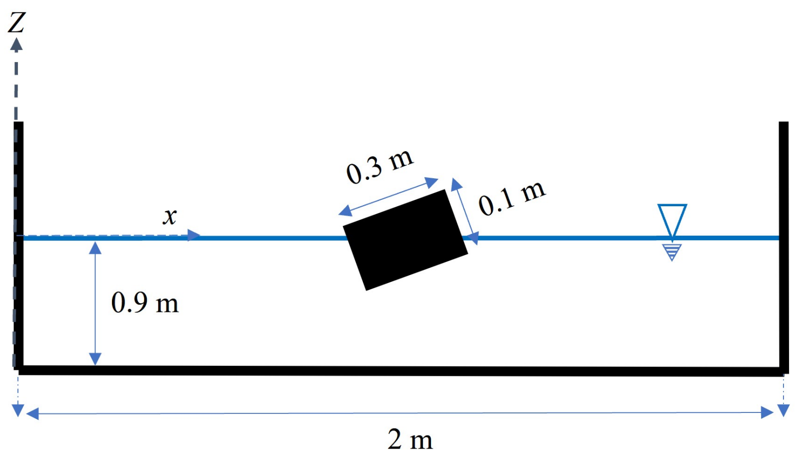

Figure 6.7 Schematic representation of the numerical tank for damped roll motion.

In Figure 6.8, we compare the time history of the roll angle of the rectangular structure during damped rolling oscillations for different particle distances (0.020 m, 0.014 m, and 0.010 m) with the experimental results from Jung et al. [48]. To identify the optimal particle resolution, we evaluate the root mean square error of the simulation outcomes, which are presented in Table 6.4. The results indicate a strong agreement between the SPH simulation outcomes and the experimental data reported in the literature. The highest degree of agreement is observed for the interparticle distances of 0.010 m.

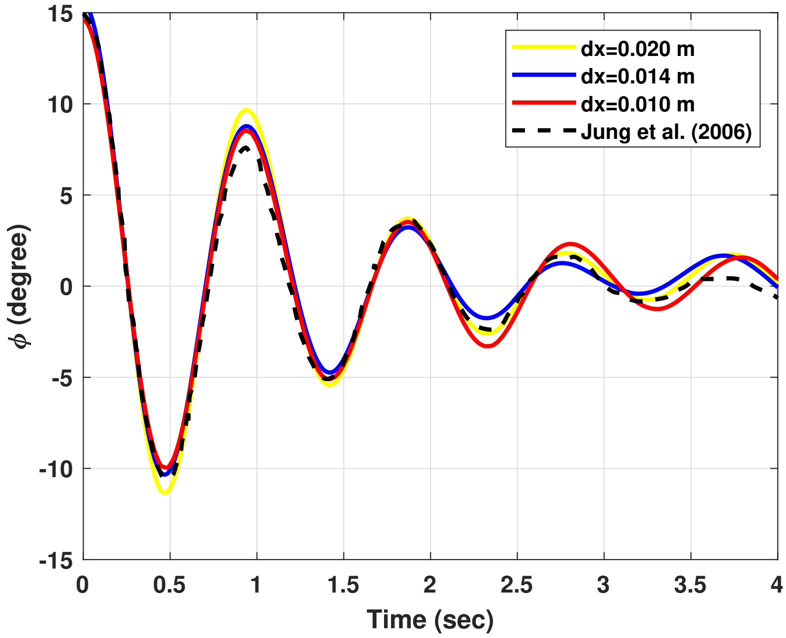

Figure 6.8 Comparison of the time history of box roll angle during damped rolling oscillation for dx values of 0.020 m, 0.014 m, and 0.010 m with experimental results from Jung et al. [48].

Table 6.4 Comparison of RMSE values for experimental [48] and SPH simulation results of the box roll angle during damped rolling oscillation, for dx values of 0.020 m, 0.014 m, and 0.010 m.

Interparticle distances [m]	**RMSE [degree]**
0.020	0.8251
0.014	0.7138
0.010	0.6781

To determine the natural frequencies, we performed Fast Fourier Transform (FFT) analyses on the time histories shown in Figure 6.8. The resulting frequency spectra are presented in Figure 6.9. For a interparticle distances (dx) of 0.010 m, the spectrum reveals a natural period of 0.968 s and a corresponding natural angular frequency of 6.495 rad/s.

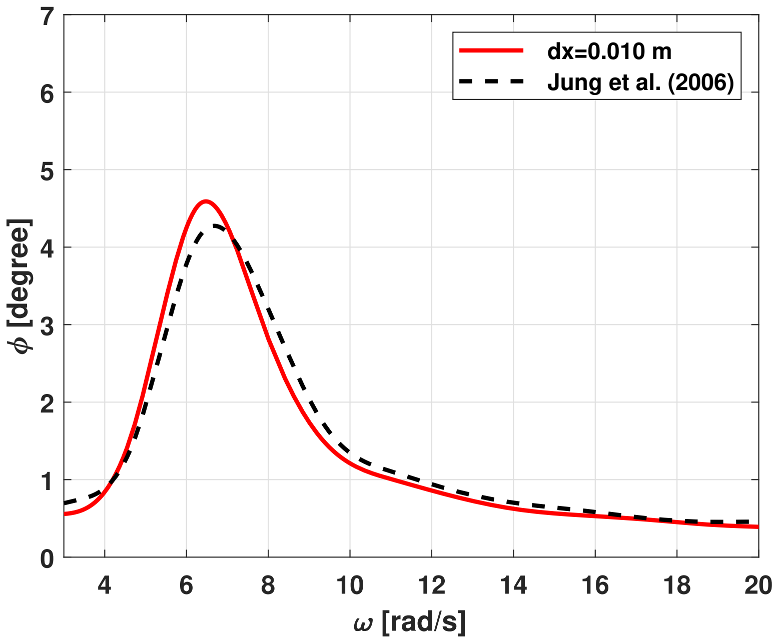

Figure 6.9 Spectrum analysis of the roll free decay test.

After calculating the natural roll frequency and roll period of the investigated rolling box, we proceeded to compute the damping coefficient and damping ratio using the following procedure [48, 59]. The equation of motion governing the roll dynamics of a structure is given by:

$$I'\frac{d^2\theta}{dt^2} + b\frac{d\theta}{dt} + c\theta = 0, \tag{6.21}$$

where θ represents the roll angle. The virtual mass moment of inertia for roll is denoted by I', which is known to be 0.36 kg m^2 [48] for the current case study, according to Jung et al. [48]. The damping coefficient is represented by b, and the restoring force coefficient is represented by c.

The damping coefficient b can be computed using the formula provided by Jung et al. [48]:

$$\frac{b}{I'} = 2\zeta_d\omega_n, \tag{6.22}$$

where ζ_d signifies the damping ratio, and ω_n represents the natural frequency. Consequently, the equation of motion can be reformulated as:

$$\frac{d^2\theta}{dt^2} + 2\zeta_d\omega_n\frac{d\theta}{dt} + \omega_n^2\theta = 0. \tag{6.23}$$

The damping coefficient b can be computed using the formula provided by Jung et al. [48]:

$$b = \frac{K_s T_\varphi \Delta g M}{\pi^2}, \tag{6.24}$$

Where K_s represents the slope of the rolling extinction curve, it characterizes the rate at which the rolling motion of an object diminishes over time due to damping. The rolling extinction curve, depicted in Figure 6.10, illustrates the relationship between the decrease in inclination for a single roll ($\frac{d\phi}{dn}$) and the total inclination (ϕ_m). The quantity $\frac{d\phi}{dn}$ represents the difference between successive amplitudes of the structure, regardless of the direction of inclination. On the other hand, ϕ_m denotes the average angle of roll for a single roll. The slope of this curve can be utilized to calculate the damping coefficient. The roll period, denoted as T_φ, and the change in the metacentric height, represented by Δ, are the key parameters involved in this calculation. Additionally, the mass of the box, denoted as M, is considered in the determination of the damping coefficient.

Finally, the damping ratio ζ_d can be determined as follows:

$$\zeta_d = \frac{b}{2\omega_n I'}. \tag{6.25}$$

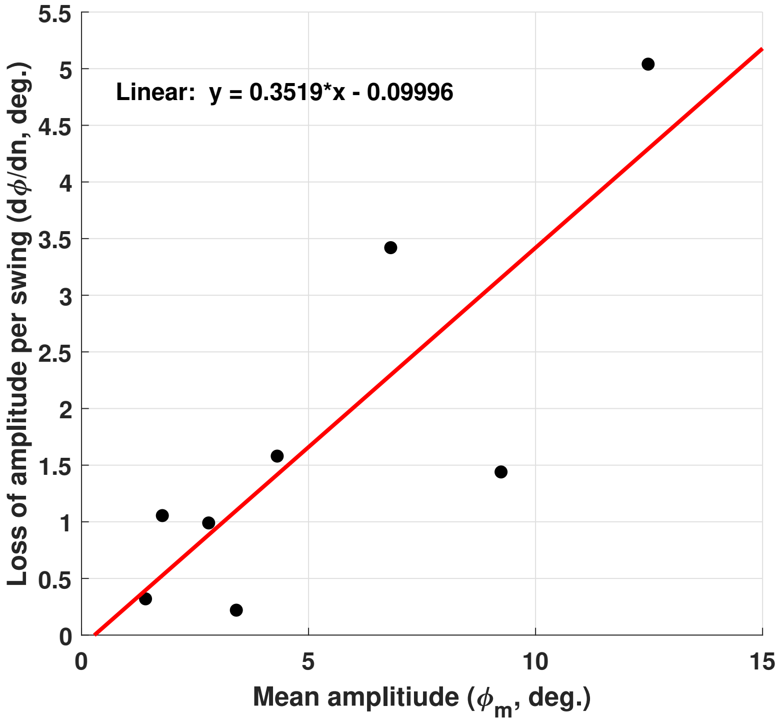

Figure 6.10 Rolling extinction curve for dx=0.010 m.

Figure 6.10 illustrates the curve depicting the decay of rolling for a interparticle distance (dx) of 0.010 m. From this curve, we determined the value of K_s to be 0.3519. The rectangular structure has a mass of 13.5 kg and a metacentric height (Δ) of 0.125 m [48]. Using Equation (6.24), we computed the damping coefficient b to be 0.575. As a result, the damping ratio ζ_d was found to be 0.123.

Table 6.5 provides a comprehensive comparison of the natural frequency, natural period, and damping ratio values for the roll motion dynamics. The experimental results are presented alongside the corresponding values obtained from the SPH simulations. The experimental data yields a natural frequency (ω_n) of 6.780 rad/s and a natural period (T_n) of 0.926 s. The damping ratio (ζ_d) is determined to be 0.106. On the other hand, the SPH simulations yield a slightly lower natural frequency of 6.495 rad/s and a longer natural period of 0.968 s. The damping ratio obtained from the simulations is 0.123. Upon closer inspection, it is evident that the results from the SPH simulations match reasonably well with the experimental measurements. Although there are slight deviations observed between the simulated and experimental values, the overall trends and magnitudes are in good agreement.

Table 6.5 Comparison of Roll Motion Dynamics

	Natural Frequency ω_n $[rad.s^{-1}]$	**Natural Period** T_n $[s]$	**Damping Ratio** ζ_d
Experimental	6.780	0.926	0.106
SPH	6.495	0.968	0.123
Error	-4.2%	4.5%	16%

6.2.4 Investigating the Rolling Motion of a Floating Box in the Presence of Regullar Ocean Waves

In this section, our objective is to investigate the response of a rectangular floating body to various regular wave conditions through SPH numerical simulations. Building upon the calculations of the natural frequency and period of the box in the previous section, we now proceed to test the structure's response to waves with different periods, including those shorter, equal to, and longer than the natural period.

To further explore this relationship, we conducted simulations under different wave conditions, as outlined in Table 6.6. These specific wave conditions were selected based on a previous experiment conducted by Jung et al. [48], allowing us to validate the feasibility of our solver for simulating the interaction problem. Figure 6.11 depicts the schematic of the numerical wave flume utilized during the simulations.

Table 6.6 Selected wave scenarios.

Case	**1**	**2**	**3**	**4**	**5**	**6**	**7**	**8**	**9**
ω $[rad.s^{-1}]$	4.830	5.240	5.710	6.280	6.760	7.390	7.850	8.980	10.470
T $[s]$	1.300	1.200	1.100	1.000	0.930	0.850	0.800	0.700	0.600
H $[m]$	0.060	0.060	0.057	0.044	0.027 0.032 0.040	0.033	0.029	0.029	0.017

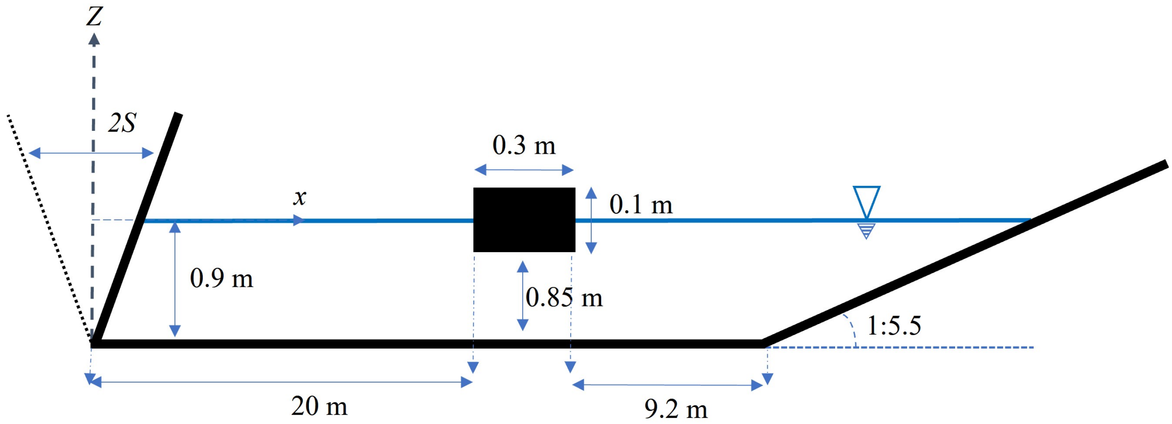

Figure 6.11 Sketch of numerical wave tank for damped roll motion.

Figure 6.12 illustrates a comparison between experimental measurements obtained during the experiment [48] using waves of different characteristics: a) $T = 0.93$ s, $H = 0.027$ m, and b) $T = 1.2$ s, $H = 0.060$ m, and the results obtained from our SPH simulations. The comparison is performed for both the free surface elevation of the incoming waves and the roll angle of the structure. The measurement of the free surface elevation and roll angle aims to provide insights into the dynamic response of the floating box structure under wave conditions. Our analysis reveals a strong agreement between the SPH and experimental results in terms of surface elevation and roll angles.

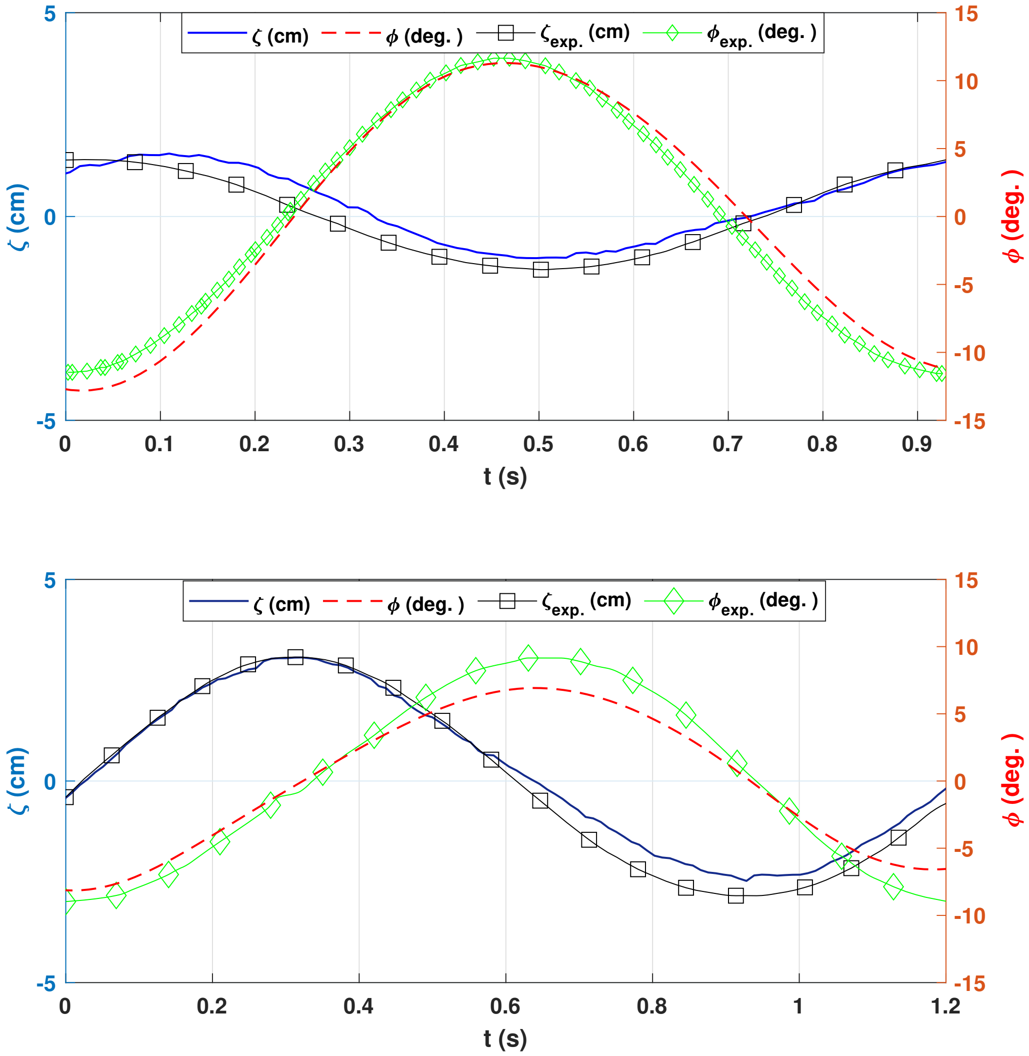

Figure 6.12 Comparison between experimental measurements [48] and SPH simulations for the free surface elevation and roll angle of the structure. The comparison is conducted for two sets of wave conditions: a) $T = 0.93$ s, $H = 0.027$ m and b) $T = 1.2$ s, $H = 0.060$ m.

To enhance the validation of our methodology, we conducted a comparison between our RAO results and the experimental data provided by Jung et al. [48]. Additionally, we compared our RAOs with the results obtained from linear potential theory, as a function of ω/ω_N (where ω represents the wave frequency and ω_N denotes the natural frequency). As depicted in Figure 6.13, our RAOs exhibit a close resemblance to the experimental results and align well with the predictions of linear potential theory, particularly for higher frequency waves. However, potential theory significantly overestimates the roll motion at the natural frequency due to neglecting viscous damping. These results suggest that our SPH approach can accurately predict the roll motion of a floating body under the influence of regular waves with varying periods.

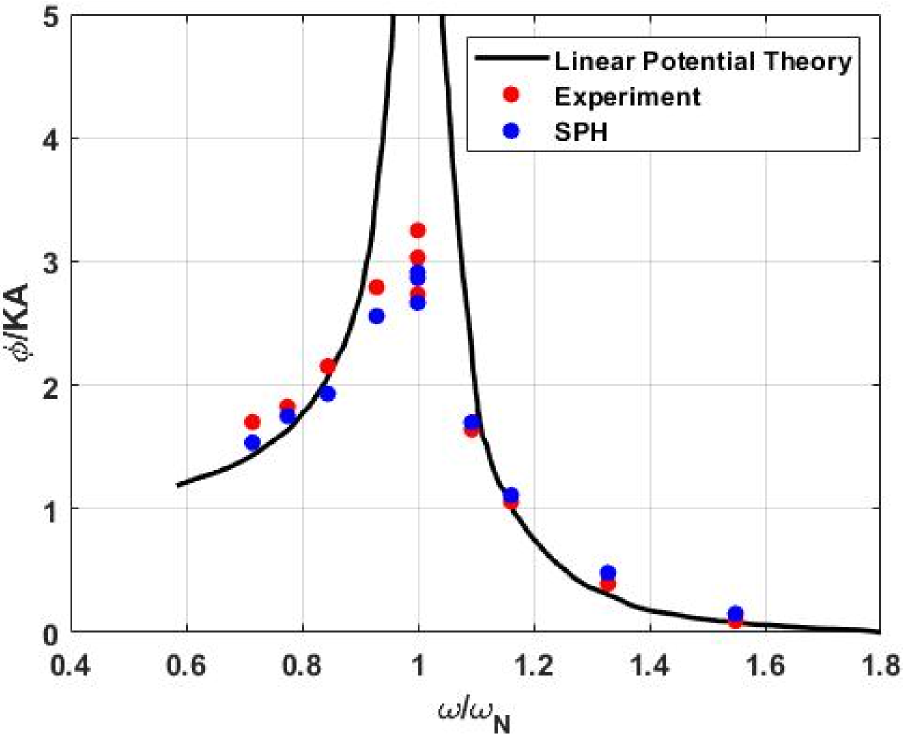

Figure 6.13 Magnification factors (RAOs) for roll motion.

The amplitude spectra of the roll motions were computed using the Fast Fourier Transformation method. The results, depicted in Figure 6.14, demonstrate a correspondence between the dominant frequencies of roll motions for the floating body and the incident wave frequencies.

Our study has revealed that the viscous damping has a significant effect on the roll motion of the structure under regular wave conditions. Specifically, when the wave period matches the natural period of the structure, the viscous damping strongly dampens the roll motion. In contrast, for wave periods shorter or longer than the natural period, the effect of viscous damping is weaker, and can even amplify the roll motion for longer wave periods.

Overall, our study highlights the importance of considering the effect of viscous damping on the roll motion of structures, especially near the natural frequency. The results suggest that our SPH approach can accurately predict the roll motion of floating bodies under the influence of regular waves with varying periods. This provides valuable insights into the behavior of floating structures in different wave conditions, which can inform the development of more effective design and engineering strategies.

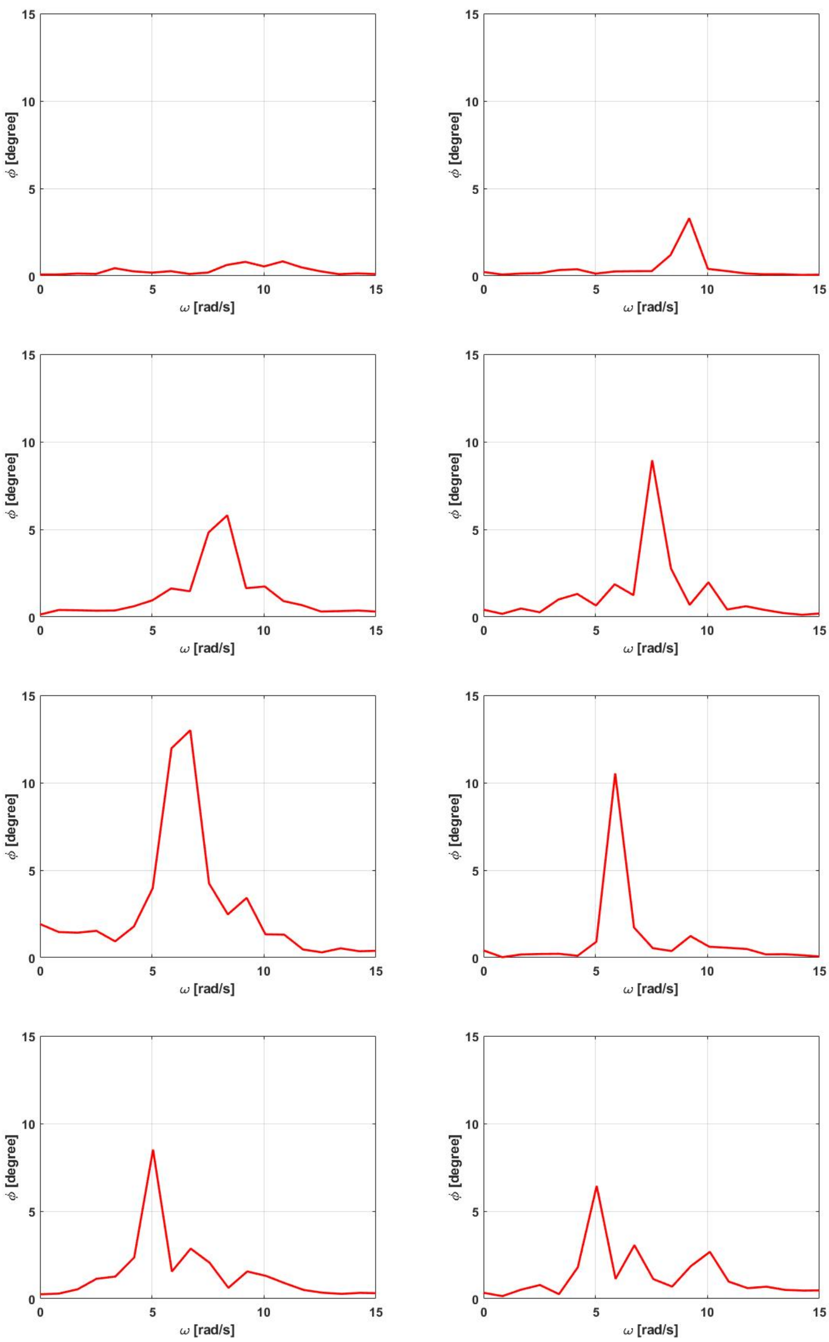

Figure 6.14 Spectrum of Roll motion for different wave conditions.

6.2.5 Investigating the Interaction of Regular Ocean Waves with a Freely Floating Box

After conducting rigorous validation tests on our in-house SPH code for generating regular waves and simulating the heave displacement of a floating box under different

PTO damping factors, as well as thoroughly investigating and validating the free roll motion of the box in both calm and regular wave conditions, we turn our attention to a challenging FSI problem: the interaction of a freely moving box with regular wave train. In this section, we present a comprehensive study of the surge, heave, and rolling motion of the box in three degrees of freedom under regular wave condition.

Our study utilizes an in-house numerical WCSPH model to accurately capture the complex and dynamic interactions between hydrodynamic forces and the motion of a floating box. This numerical model allows us to analyze the behavior of the floating box in three degrees of freedom, considering its response to various hydrodynamic forces. This approach provides valuable insights into the behavior of floating structures in real-wave conditions. We validate the results of our numerical simulations through direct comparisons with experimental data from Ren et al. [96], ensuring the accuracy and reliability of our findings.

The numerical configuration employed in this study, based on the experimental setup by Ren et al. [96], is illustrated in Figure 6.15. It comprises a 2D numerical wave flume that spans a length of 6 m, with an initial water depth (d) of 0.4 m. A flap-type wave maker is positioned on the left side of the flume, while a wave-dissipative beach and a numerical damping sponge are located on the opposite side to minimize wave reflections in the flume. In the physical experiments, regular waves with a wave height (H) of 0.1 m and a wave period (T) of 1.2 s were utilized.

For the numerical setup, an initial particle spacing (dx) of 0.01 m was employed. The rectangular box had dimensions of 30 cm in length and 20 cm in height, with a mass of 12.6 kg, resulting in a density of 500 kg/m^3.

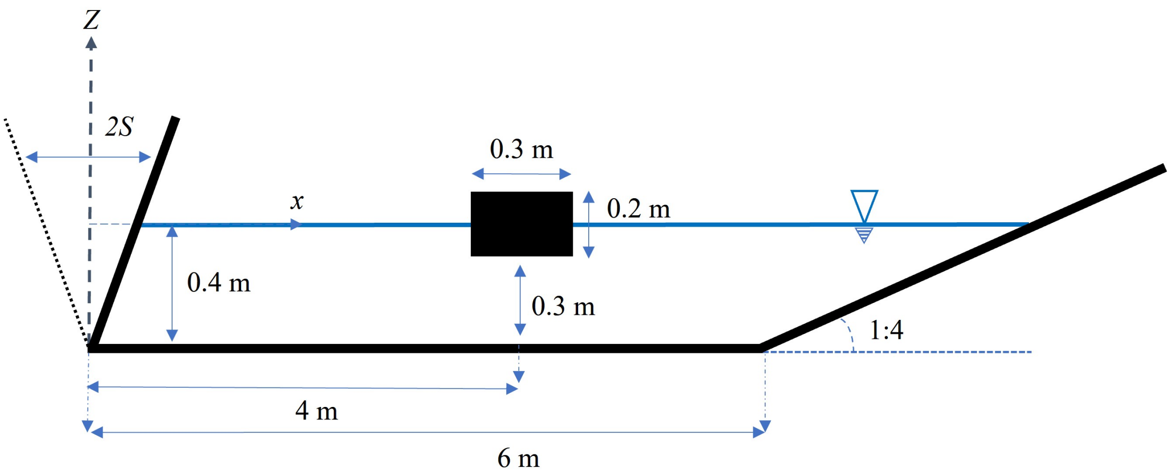

Figure 6.15 Numerical setup for the experiment by Ren et al. [96] for modeling a freely floating box.

Figure 6.16 presents a comparison of the numerical and experimental results for the heave, surge, and pitch motions of the floating box. The first row displays the heave motion, where the numerical results closely match the experimental data. The second row shows the surge motion, and it can be observed that the simulation results are in good agreement with the experimental time series. Finally, the pitch angles for both the experimental and numerical results are compared in the last row of Fig. 6.16. These results demonstrate the ability of our in-house SPH code to accurately simulate fluid-driven structures under the influence of regular waves.

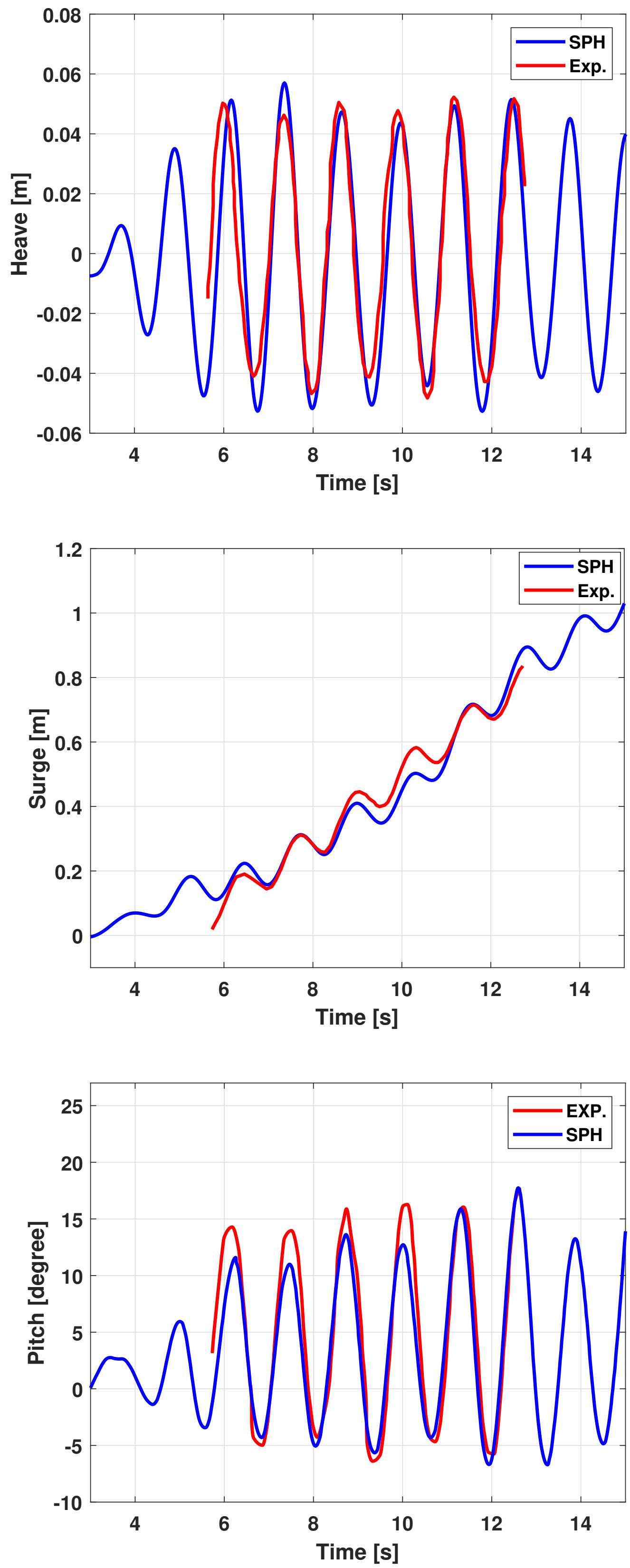

Figure 6.16 Comparison between experimental and numerical time-series of heave (a) and surge (b) motion of a freely floating box, as well as the pitch angles (c) under the influence of regular waves.

Furthermore, Fig. 6.17 shows the centroid trajectories (X position versus Z position) of the floating box over several motion periods, with a satisfactory agreement between the numerical and experimental results. This indicates that the numerical model can accurately capture the dynamic behavior of the floating box under real wave conditions.

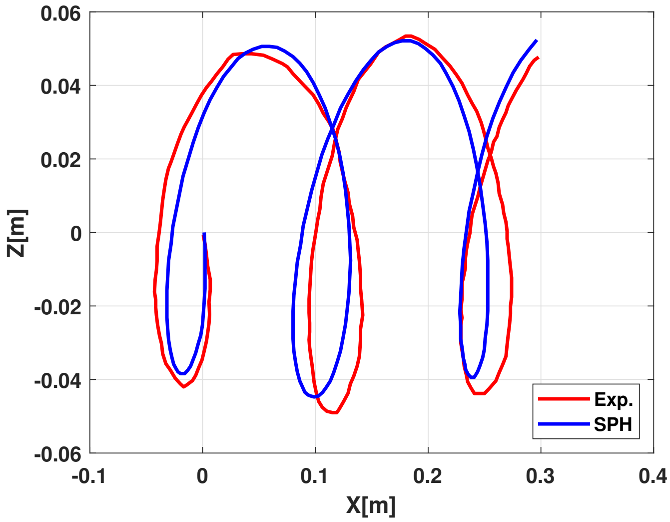

Figure 6.17 Centroid trajectories of the floating box.

Overall, these results confirm the reliability and accuracy of our numerical simulations, and demonstrate the potential of SPH for modeling the behavior of floating structures in real-ocean wave conditions. Our study provides valuable insights into the behavior of floating structures in challenging ocean environments and can inform the development of more effective, efficient, and sustainable offshore structures.

6.3 Conclusions

In conclusion, our study utilizes SPH simulations to comprehensively analyze the behavior of floating structures under the influence of waves across different scenarios. The reliability and accuracy of our SPH model have been extensively validated through direct comparisons with experimental and theoretical data reported in the literature. These validations confirm the robustness of our findings and the effectiveness of our SPH approach in accurately representing the dynamics of floating structures.

We verified the accuracy of our numerical wave-making model in the first part of our study by comparing numerical and theoretical time series data of wave surface elevation and orbital velocities at a specific location, showing good agreement between them.

In the second part of our study, we focused on examining the heave displacement and vertical velocity of a point-absorber wave energy converter under various PTO damping factors. Additionally, we calculated the efficiency of the wave energy converter device. This investigation involved a comprehensive comparison between SPH numerical simulations and experimental measurements obtained from the literature. Our findings showcase the accuracy and reliability of our numerical model in capturing the behavior of the point-absorber device under different PTO damping factors, reinforcing the validity of our approach.

In the third part of our study, we focused on the validation and calibration of our WCSPH model specifically for the free roll motion of a rectangular floating structure with a free surface. To achieve this, we compared our simulation results with the experimental findings reported by Jung et al. [48]. Through this comparison, we were able to confirm the accuracy and reliability of our approach in predicting the roll motion of the floating body under calm sea conditions.

In the fourth part of our study, we explored the relationship between the RAOs and wave frequencies and steepness. Our findings revealed the substantial influence of viscous damping on the roll motion of the structure under regular wave conditions. This investigation provided valuable insights into the dynamics of the system and highlighted the importance of considering viscous damping effects when analyzing the response of floating structures to waves.

Finally, we used our in-house code to further investigate the behavior of floating structures under real-ocean conditions, comparing our simulation results with the experimental data of Ren et al. [96] Our study provides valuable insights into the behavior of floating structures in challenging ocean environments and can inform the development of more effective, efficient, and sustainable offshore structures.

In summary, our study underscores the significance of our in-house WCSPH code in accurately modeling the behavior of floating structures in real-ocean wave conditions. By utilizing this code, we have gained valuable insights into the dynamic response and performance of these structures. Our findings have broader implications for the design and engineering of wave energy converters, offshore structures, and other floating systems.

7. GENERAL CONCLUSIONS

The primary objective of this dissertation was to investigate advanced computational modeling techniques for wave energy converters and fluid-structure interaction using the SPH approach. The following results, which align with the research objectives, are presented below:

In Chapter 3, the SPH technique is utilized to model a numerical wave tank. The governing equations for fluid motion, specifically the Navier-Stokes and continuity equations, are solved using the WCSPH approach.

To generate regular and irregular waves, a moving boundary is implemented at the inlet of the tank. A dissipative beach is added at the end of the numerical wave tank to simulate natural damping. Various test cases involving different wavelengths and steepness ratios are investigated for the regular wave simulations. Despite applying a linear sinusoidal oscillation to the wave-maker at the inlet, the nonlinear behavior of the free surface becomes apparent due to the relatively high wave steepness ratios. This observation is confirmed through FFT analyses. The wave energy densities obtained from the SPH results are compared with the expectations of the linear theory per unit wavelength. Additionally, the conditions for wave-breaking inception are examined by simulating three additional wave steepness values at a single wavelength.

As a further validation of the proposed SPH scheme, the JONSWAP irregular wave spectrum is employed with both flap and piston-type moving boundaries. The conducted simulations demonstrate that the proposed SPH numerical scheme is robust and consistent in generating regular and irregular wave systems in deep-water conditions. It exhibits high sensitivity in capturing the nonlinear characteristics of the generated waves, including wave-breaking phenomena.

In Chapter 4, the WCSPH approach is employed to investigate the hydrodynamic characteristics of an overtopping wave energy converter system. The numerical performance of the proposed SPH scheme is examined by quantitatively comparing the average overtopping rate for the OWEC device with different slope angles. The average overtopping rates obtained from the numerical simulations at two different particle resolutions are calculated and compared with existing prediction formulas from the literature. The simulation results demonstrate that the proposed SPH scheme accurately captures the average overtopping rates predicted by empirical formulas over a wide range of slope angle variations, particularly with increasing particle resolutions within the problem domain.

Chapter 5 of this PhD thesis focuses on investigating the effects of geometry on the performance of OWC-type wave energy converter systems. The objective is to identify OWC geometries that enhance energy efficiency under consistent wave conditions. The study employs a two-step geometry modification procedure to enhance the energy efficiency of the selected OWC device.

The first step involves validating the accuracy of the free-surface elevation and orbital velocity time histories. Subsequently, a 3-by-3 simulation matrix is constructed, incorporating the geometrical design parameters of chamber length and front wall draft. This matrix facilitates simulations at three distinct wave conditions, enabling the determination of the OWC geometry that yields the maximum energy efficiency. In the second step, the corner regions of the optimized geometry are chamfered, and another simulation matrix is employed to evaluate wave energy production under the wave condition that maximizes energy generation. Notably, this step reveals that chamfering only the back face of the OWC chamber can lead to a further 4.3% improvement in the energy efficiency index.

Furthermore, a quantified relationship between the time-averaged vorticity within the chamber region and energy efficiency is established. The analysis of vorticity within the chamber region demonstrates that reducing the magnitude of vorticity results in higher overall energy efficiency of the device, aligning with the expected outcomes based on energy conservation laws in physics.

In summary, the potential of harvested wave energy is heavily influenced by the OWC geometry for each specific wave condition. By appropriately designing the OWC geometry to align with the dominant wave climates of the region, the collected energy can be increased. This overall assessment underscores the significance of optimizing the OWC geometry to maximize wave energy extraction.

In conclusion, Chapter 6 of this PhD thesis presents a comprehensive study that utilizes SPH simulations to analyze the behavior of floating structures under specific wave conditions. This chapter is based on the accomplishment of five key sub-steps. The reliability and accuracy of our SPH model have been extensively validated through rigorous comparisons with experimental and theoretical data reported in the literature. These validations affirm the robustness of our findings and the effectiveness of our SPH approach in accurately representing the intricate dynamics of floating structures.

The first crucial step focuses on ensuring the utmost accuracy of the generated wave characteristics. Subsequently, we examine the heave motion of a point-absorber wave energy converter to validate the modeling of rigid body motion under regular wave conditions, considering various PTO damping coefficients. Additionally, we calculate the efficiency of the wave energy converter device. To further assess the validity of our model, we investigate the free roll motion of a rectangular floating body by comparing its natural frequencies and damping coefficients with available data in the literature. Having achieved highly accurate results in the free roll motion analysis, we proceed to simulate the roll motion of a fixed floating structure under a wide range of regular wave systems to obtain the corresponding RAOs. Lastly, we thoroughly examine the free body motion of a floating structure under regular wave excitation conditions, taking into account all relevant kinematic and dynamic aspects of the problem.

These comprehensive findings provide valuable insights into the dynamic response and performance of floating structures, making a significant contribution to the design and engineering of offshore structures, wave energy converters, and other floating systems operating in challenging ocean environments. The results obtained from this study have broader implications for the development of more effective, efficient, and sustainable offshore structures. They underscore the paramount importance of our in-house WCSPH code in accurately modeling the intricate behavior of floating structures under real-ocean wave conditions.

BIBLIOGRAPHY

[1] Abas, N., Kalair, A., & Khan, N. (2015). Review of fossil fuels and future energy technologies. *Futures*, *69*, 31–49.

[2] Aderinto, T. & Li, H. (2019). Review on power performance and efficiency of wave energy converters. *Energies*, *12*(22), 4329.

[3] Ahamed, R., McKee, K., & Howard, I. (2020). Advancements of wave energy converters based on power take off (pto) systems: A review. *Ocean Engineering*, *204*, 107248.

[4] Almasi, F., Shadloo, M. S., Hadjadj, A., Ozbulut, M., Tofighi, N., & Yildiz, M. (2021). Numerical simulations of multi-phase electro-hydrodynamics flows using a simple incompressible smoothed particle hydrodynamics method. *Computers & Mathematics with Applications*, *81*, 772–785.

[5] Altomare, C., Crespo, A., Domínguez, J., Gómez-Gesteira, Suzuki, T., & Verwaest, T. (2015). Applicability of smoothed particle hydrodynamics for estimation of sea wave impact on coastal structures. *Coastal Engineering*, *96*, 1–12.

[6] Altomare, C., Crespo, A. J., Domínguez, J. M., Gómez-Gesteira, M., Suzuki, T., & Verwaest, T. (2015). Applicability of smoothed particle hydrodynamics for estimation of sea wave impact on coastal structures. *Coastal Engineering*, *96*, 1–12.

[7] Altomare, C., Domínguez, J. M., Crespo, A., González-Cao, J., Suzuki, T., Gómez-Gesteira, M., & Troch, P. (2017). Long-crested wave generation and absorption for sph-based dualsphysics model. *Coastal Engineering*, *127*, 37–54.

[8] Altomare, C., Domínguez, J., Crespo, A., González-Cao, J., Suzuki, T., Gómez-Gesteira, M., & Troch, P. (2017). Long-crested wave generation and absorption for SPH based DualSPHysics model. *Coastal Engineering*, *127*, 37–54.

[9] Antonio, F. d. O. (2010). Wave energy utilization: A review of the technologies. *Renewable and sustainable energy reviews*, *14*(3), 899–918.

[10] Antuono, M., Colagrossi, A., Marrone, S., & Lugni, C. (2011). Propagation of gravity waves through an SPH scheme with numerical diffusive terms. *Computer Physics Communications*, *182*, 866–877.

[11] Bhattacharya, R. (1978). *Dynamics of Marine Vehicles*. John Wiley & Sons Inc.

[12] Biesel, F. (1951). Etude théorique d'un type d'appareil à houle. *La Houille Blanche*, *6*, 152–165.

[13] Bouscasse, B., Colagrossi, A., Marrone, S., & Souto-Iglesias, A. (2017). Sph modelling of viscous flow past a circular cylinder interacting with a free surface. *Computers & Fluids*, *146*, 190–212.

[14] Chang, C.-Y., Chou, F. N.-F., Chen, Y.-Y., Hsieh, Y.-C., & Chang, C.-T. (2016). Analytical and experimental investigation of hydrodynamic performance and chamber optimization of oscillating water column system. *Energy*, *113*, 597–614.

[15] Clément, A., McCullen, P., Falcão, A., Fiorentino, A., Gardner, F., Hammarlund, K., Lemonis, G., Lewis, T., Nielsen, K., Petroncini, S., et al. (2002). Wave energy in europe: current status and perspectives. *Renewable and sustainable energy reviews*, *6*(5), 405–431.

[16] Colagrossi, A., Nikolov, G., Durante, D., Marrone, S., & Souto-Iglesias, A. (2019). Viscous flow past a cylinder close to a free surface: benchmarks with steady, periodic and metastable responses, solved by meshfree and mesh-based schemes. *Computers and Fluids*, *181*, 345–363.

[17] Crespo, A., Altomare, C., Domínguez, J., González-Cao, J., & Gómez-Gesteira, M. (2017). Towards simulating floating offshore oscillating water column converters with smoothed particle hydrodynamics. *Coastal Engineering*, *126*, 11–26.

[18] Crespo, A., Domínguez, J., Rogers, B., Gómez-Gesteira, Longshaw, S., Canelas, R., Vacondio, R., Barreiro, A., & García-Feal, O. (2015). DualSPHysics: open-source parallel CFD solver based on smoothed particle hydrodynamics (SPH). *Comput Phys Commun*, *187*, 204–216.

[19] Dalrymple, R. A. & Dean, R. G. (1991). *Water wave mechanics for engineers and scientists*, volume 2. World Scientific Publishing Company.

[20] De Rouck, J., Verhaeghe, H., & Geeraerts, J. (2009). Crest level assessment of coastal structures—general overview. *Coastal Engineering*, *56*(2), 99–107.

[21] Dean, R. & Dalrymple, R. (1991). Water wave mechanics for engineers and scientists. *World Scientific Publishing Company*, *2*, 368.

[22] Dias, F., Renzi, E., Gallagher, S., Sarkar, D., Wei, Y., Abadie, T., Cummins, C., & Rafiee, A. (2017). Analytical and computational modelling for wave energy systems: the example of oscillating wave surge converters. *Acta Mechanica Sinica*, *33*(4), 647–662.

[23] Domínguez, J. M., Crespo, A. J., Hall, M., Altomare, C., Wu, M., Stratigaki, V., Troch, P., Cappietti, L., & Gómez-Gesteira, M. (2019). Sph simulation of floating structures with moorings. *Coastal Engineering*, *153*, 103560.

[24] Drew, B., Plummer, A. R., & Sahinkaya, M. N. (2009). A review of wave energy converter technology. *Proceedings of the Institution of Mechanical Engineers, Part A: Journal of Power and Energy*, *223*(8), 887–902.

[25] Elhanafi, A., Fleming, A., Macfarlane, G., & Leong, Z. (2016). Numerical energy balance analysis for an onshore oscillating water column–wave energy converter. *Energy*, *116*, 539–557.

[26] Energy, B. (2016). Renewables 2017 global status report. *Renewable Energy Policy Network for the 21st Century. Paris: REN21.*

[27] Falnes, J. (2007). A review of wave-energy extraction. *Marine structures*, *20*(4), 185–201.

[28] Falnes, J. & Kurniawan, A. (2020). *Ocean waves and oscillating systems: linear interactions including wave-energy extraction*, volume 8. Cambridge university press.

[29] Fatehi, R., Rahmat, A., Tofighi, N., Yildiz, M., & Shadloo, M. (2019). Density-based smoothed particle hydrodynamics methods for incompressible flows. *Computers & Fluids*, *185*, 22–33.

[30] Fontanet, P. (1961). Théorie de la génération de la home cylindrique par un batteur plan. *La Huille Blanche*, *16*, 3–31.

[31] Forsythe, G. E. & Wasow, W. R. (1960). Finite-difference methods for partial differential equations. *Applied Mathematics Series*.

[32] Fourey, G., Hermange, C., Le Touzé, D., & Oger, G. (2017). An efficient fsi coupling strategy between smoothed particle hydrodynamics and finite element methods. *Computer Physics Communications*, *217*, 66–81.

[33] Fu, Z.-J., Zhang, J., Li, P.-W., & Zheng, J.-H. (2020). A semi-lagrangian meshless framework for numerical solutions of two-dimensional sloshing phenomenon. *Engineering Analysis with Boundary Elements*, *112*, 58–67.

[34] Gallach-Sánchez, D., Troch, P., & Kortenhaus, A. (2018). A critical analysis and validation of the accuracy of wave overtopping prediction formulae for owecs. *Energies*, *11*(1), 133.

[35] Gingold, R. A. & Monaghan, J. J. (1977). Smoothed particle hydrodynamics: theory and application to non-spherical stars. *Monthly notices of the royal astronomical society*, *181*(3), 375–389.

[36] Gotoh, H. & Khayyer, A. (2018). On the state-of-the-art of particle methods for coastal and ocean engineering. *Coastal Engineering Journal*, *60*(1), 79–103.

[37] Gotoh, H., Khayyer, A., & Shimizu, Y. (2021). Entirely lagrangian meshfree computational methods for hydroelastic fluid-structure interactions in ocean engineering—reliability, adaptivity and generality. *Applied Ocean Research*, *115*, 102822.

[38] Hasselmann, K., Barnett, T. P., Bouws, E., Carlson, H., Cartwright, D. E., Enke, K., Ewing, J., Gienapp, A., Hasselmann, D., Kruseman, P., et al. (1973). Measurements of wind-wave growth and swell decay during the joint north sea wave project (jonswap). *Ergaenzungsheft zur Deutschen Hydrographischen Zeitschrift, Reihe A*.

[39] Havelock, T. (1929). Forced surface waves on water. *Phil. Mag. Series*, *7*, 569–576.

[40] He, J., Tofighi, N., Yildiz, M., Lei, J., & Suleman, A. (2017). A coupled wc-tl sph method for simulation of hydroelastic problems. *International Journal of Computational Fluid Dynamics*, *31*(3), 174–187.

[41] Hermange, C., Oger, G., Le Chenadec, Y., & Le Touzé, D. (2019). A 3d SPH-FE coupling for FSI problems and its application to tire hydroplaning simulations on rough ground. *Computer Methods in Applied Mechanics and Engineering*, *355*, 558–590.

[42] Hudspeth, R. & Sulisz, W. (1991). Stokes drift in two-dimensional wave flumes. *Journal of Fluid Mechanics*, *230*, 209–229.

[43] Hyun, J. (1975). Theory of hinged wavemakers of finite draft in water of constant depth. *Journal of Hydronautics*, *10*(1), 2–7.

[44] Ibarra-Berastegi, G., Sáenz, J., Ulazia, A., Serras, P., Esnaola, G., & Garcia-Soto, C. (2018). Electricity production, capacity factor, and plant efficiency index at the mutriku wave farm (2014–2016). *Ocean Engineering*, *147*, 20–29.

[45] Idelsohn, S., Oñate, E., & Del Pin, F. (2003). A lagrangian meshless finite element method applied to fluid–structure interaction problems. *Computers & Structures*, *81*(8-11), 655–671.

[46] ITTC (2002). The specialist committee on waves. In *ITTC - Recomended Procedures and Guidelines, Proceedings of* 23^{rd} *ITTC*, volume 2, (pp. 1–13)., Venice, Italy.

[47] Iturrioz, A., Guanche, R., Armesto, J., Alves, M., Vidal, C., & Losada, I. (2014). Time-domain modeling of a fixed detached oscillating water column towards a floating multi-chamber device. *Ocean Engineering*, *76*, 65–74.

[48] Jung, K. H., Chang, K.-A., & Jo, H. J. (2006). Viscous effect on the roll motion of a rectangular structure. *Journal of engineering mechanics*, *132*(2), 190–200.

[49] Kamakoti, R. & Shyy, W. (2004). Fluid–structure interaction for aeroelastic applications. *Progress in Aerospace Sciences*, *40*(8), 535–558.

[50] Kamath, A., Bihs, H., & Arntsen, Ø. A. (2015). Numerical investigations of the hydrodynamics of an oscillating water column device. *Ocean Engineering*, *102*, 40–50.

[51] Kharati-Koopaee, M. & Fathi-Kelestani, A. (2020). Assessment of oscillating water column performance: Influence of wave steepness at various chamber lengths and bottom slopes. *Renewable Energy*, *147*, 1595–1608.

[52] Khatibani, M. J. & Ketabdari, M. J. (2022). Numerical modeling of an innovative hybrid wind turbine and wec systems performance: A case study in the persian gulf. *Journal of Ocean Engineering and Science*.

[53] Khayyer, A., Gotoh, H., Falahaty, H., & Shimizu, Y. (2018). An enhanced isph–sph coupled method for simulation of incompressible fluid–elastic structure interactions. *Computer Physics Communications*, *232*, 139–164.

[54] Khayyer, A., Gotoh, H., & Shao, S. (2009). Enhanced predictions of wave impact pressure by improved incompressible sph methods. *Applied Ocean Research*, *31*(2), 111–131.

[55] Kolukisa, D. C., Ozbulut, M., Pesman, E., & Yildiz, M. (2020). Development of computationally efficient augmented lagrangian sph for incompressible flows and its quantitative comparison with wcsph simulating flow past a circular cylinder. *International Journal for Numerical Methods in Engineering*, *121*(18), 4187–4207.

[56] Le Meahute, B. (1976). *An Introduction to Hydrodynamics and Water Waves*. Springer-Verlag.

[57] Le Méhauté, B. (2013). *An introduction to hydrodynamics and water waves*. Springer Science & Business Media.

[58] Libersky, L. D., Petschek, A. G., Carney, T. C., Hipp, J. R., & Allahdadi, F. A. (1993). High strain lagrangian hydrodynamics: a three-dimensional sph code for dynamic material response. *Journal of computational physics*, *109*(1), 67–75.

[59] Lifen, C., Liang, S., Jun, Z., Hillis, A. J., & Plummer, A. R. (2016). Numerical study of roll motion of a 2-d floating structure in viscous flow. *Journal of Hydrodynamics, Ser. B*, *28*(4), 544–563.

[60] Lind, S., Stansby, P., & Rogers, B. (2016). Fixed and moored bodies in steep and breaking waves using SPH with the Froude Krylov approximation. *Journal of Ocean Engineering and Marine Energy*, *2*, 331–354.

[61] Liu, M. & Liu, G. (2010). Smoothed particle hydrodynamics (sph): an overview and recent developments. *Archives of computational methods in engineering*, *17*(1), 25–76.

[62] Long, T., Hu, D., Wan, D., Zhuang, C., & Yang, G. (2017). An arbitrary boundary with ghost particles incorporated in coupled fem–sph model for fsi problems. *Journal of Computational Physics*, *350*, 166–183.

[63] López, I., Andreu, J., Ceballos, S., De Alegría, I. M., & Kortabarria, I. (2013). Review of wave energy technologies and the necessary power-equipment. *Renewable and sustainable energy reviews*, *27*, 413–434.

[64] López, I., Pereiras, B., Castro, F., & Iglesias, G. (2014). Optimisation of turbine-induced damping for an owc wave energy converter using a rans–vof numerical model. *Applied Energy*, *127*, 105–114.

[65] Lucy, L. (1977). Numerical approach to testing the fission hypothesis. *Astronomical Journal*, *82*, 1013–1024.

[66] Luo, M., Khayyer, A., & Lin, P. (2021). Particle methods in ocean and coastal engineering. *Applied Ocean Research*, *114*, 102734.

[67] Lyu, H.-G., Sun, P.-N., Huang, X.-T., Zhong, S.-Y., Peng, Y.-X., Jiang, T., & Ji, C.-N. (2022). A review of sph techniques for hydrodynamic simulations of ocean energy devices. *Energies*, *15*(2), 502.

[68] Ma, Q., Zhou, Y., & Yan, S. (2016). A review on approaches to solving poisson's equation in projection-based meshless methods for modelling strongly nonlinear water waves. *Journal of Ocean Engineering and Marine Energy*, *2*, 279–299.

[69] Madhi, F. & Yeung, R. W. (2018). On survivability of asymmetric wave-energy converters in extreme waves. *Renewable Energy*, *119*, 891–909.

[70] Madsen, O. (1971). On the generation of long waves. *J. Geophys Res*, *76*, 8672–8673.

[71] Markel, P. & Ringwood, J. V. (2016). A review of wave-to-wire models for wave energy converters. *Energies*, *9*(7), 506.

[72] Marrone, S., Antuono, M., Colagrossi, A., Colicchio, G., Touzé, D., & Graziani, G. (2011). δ-SPH model for simulating violent impact flows. *Comput Methods Appl Mech Engrg*, *200*, 1526–1542.

[73] Monaghan, J. (1994a). Simulating free surface flow with SPH. *Journal of Computational Physics*, *110*, 399–406.

[74] Monaghan, J. & Gingold, R. (1977). Smoothed particle hydrodynamics theory and application to non-spherical stars. *Monthly Notices of The Royal Astronomical Society*, *181*, 375–389.

[75] Monaghan, J. J. (1994b). Simulating free surface flows with sph. *Journal of computational physics*, *110*(2), 399–406.

[76] Monaghan, J. J. & Kos, A. (1999). Solitary waves on a cretan beach. *Journal of waterway, port, coastal, and ocean engineering*, *125*(3), 145–155.

[77] Mork, G., Barstow, S., Kabuth, A., & Pontes, M. T. (2010). Assessing the global wave energy potential. In *International Conference on Offshore Mechanics and Arctic Engineering*, volume 49118, (pp. 447–454).

[78] Morris-Thomas, M. T., Irvin, R. J., & Thiagarajan, K. P. (2007). An investigation into the hydrodynamic efficiency of an oscillating water column.

[79] Müller, M., Charypar, D., & Gross, M. H. (2003). Particle-based fluid simulation for interactive applications. In *Symposium on Computer animation*, (pp. 154–159).

[80] Newman, J. N. (1976). The interaction of stationary vessel with regular waves. In *International Proceedings of the 11th Symposium on Naval Hydrodynamics, ONR, 1976*.

[81] Ning, D.-Z., Shi, J., Zou, Q.-P., & Teng, B. (2015). Investigation of hydrodynamic performance of an owc (oscillating water column) wave energy device using a fully nonlinear hobem (higher-order boundary element method). *Energy*, *83*, 177–188.

[82] Ozbulut, M., Olmez, O., Kolukisa, D., Deliktas-Ozdemir, E., Goren, O., & Yildiz, M. (2022). An investigation into the nonlinear effects in the roll motion of 2-d bodies by sph method. *Ocean Engineering*, *248*, 110679.

[83] Ozbulut, M., Ramezanzadeh, S., Yildiz, M., & Goren, O. (2020). Modelling of wave generation in a numerical tank by sph method. *Journal of Ocean Engineering and Marine Energy*, *6*, 121–136.

[84] Ozbulut, M., Tofighi, N., Goren, O., & Yildiz, M. (2018a). Investigation of wave characteristics in oscillatory motion of partially filled rectangular tanks. *Journal of Fluids Engineering*, *140*(4).

[85] Ozbulut, M., Tofighi, N., Goren, O., & Yildiz, M. (2018b). Investigation of wave characteristics in oscillatory motion of partially filled rectangular tanks. *ASME Journal o Fluids Engineering*, *140*(4), 041204–041204–11.

[86] Ozbulut, M., Yildiz, M., & Goren, O. (2014). A numerical investigation into the correction algorithms for sph method in modeling violent free surface flows. *International Journal of Mechanical Sciences*, *79*, 56–65.

[87] Panwar, N., Kaushik, S., & Kothari, S. (2011). Role of renewable energy sources in environmental protection: A review. *Renewable and sustainable energy reviews*, *15*(3), 1513–1524.

[88] Papillon, L., Costello, R., & Ringwood, J. V. (2020). Boundary element and integral methods in potential flow theory: A review with a focus on wave energy applications. *Journal of Ocean Engineering and Marine Energy*, *6*, 303–337.

[89] Rahimi, M. N., Kolukisa, D. C., Yildiz, M., Ozbulut, M., & Kefal, A. (2022). A generalized hybrid smoothed particle hydrodynamics–peridynamics algorithm with a novel lagrangian mapping for solution and failure analysis of fluid–structure interaction problems. *Computer Methods in Applied Mechanics and Engineering*, *389*, 114370.

[90] Ramezanzadeh, S., Ozbulut, M., & Yildiz, M. (2019). Simulation of irregular wave motion using a flap-type wavemaker. In *MARINE VIII: proceedings of the VIII International Conference on Computational Methods in Marine Engineering*, (pp. 783–794). CIMNE.

[91] Ramezanzadeh, S., Ozbulut, M., & Yildiz, M. (2022). A numerical investigation of the energy efficiency enhancement of oscillating water column wave energy converter systems. *Energies*, *15*(21), 8276.

[92] Ran, Q., Tong, J., Shao, S., Fu, X., & Xu, Y. (2015). Incompressible sph scour model for movable bed dam break flows. *Advances in Water Resources*, *82*, 39–50.

[93] Randles, P. & Libersky, L. (1996a). Smoothed particle hydrodynamics: some recent improvements and applications. *Computer Methods in Applied Mechanics and Engineering*, *139*, 375–408.

[94] Randles, P. & Libersky, L. D. (1996b). Smoothed particle hydrodynamics: some recent improvements and applications. *Computer methods in applied mechanics and engineering*, *139*(1-4), 375–408.

[95] Ransley, E., Greaves, D., Raby, A., Simmonds, D., & Hann, M. (2017). Survivability of wave energy converters using cfd. *Renewable Energy*, *109*, 235–247.

[96] Ren, B., He, M., Dong, P., & Wen, H. (2015). Nonlinear simulations of wave-induced motions of a freely floating body using wcsph method. *Applied Ocean Research*, *50*, 1–12.

[97] Rezanejad, K., Gadelho, J., & Soares, C. G. (2019). Hydrodynamic analysis of an oscillating water column wave energy converter in the stepped bottom condition using cfd. *Renewable Energy*, *135*, 1241–1259.

[98] Ropero-Giralda, P., Crespo, A. J., Tagliafierro, B., Altomare, C., Domínguez, J. M., Gómez-Gesteira, M., & Viccione, G. (2020). Efficiency and survivability analysis of a point-absorber wave energy converter using dualsphysics. *Renewable Energy*, *162*, 1763–1776.

[99] Saghatchi, R., Ozbulut, M., & Yildiz, M. (2021). Dynamics of double emulsion interfaces under the combined effects of electric field and shear flow. *Computational Mechanics*, *68*(4), 775–793.

[100] Saghatchi, R., Rahmat, A., & Yildiz, M. (2020). Electrohydrodynamics of a droplet in a highly confined domain: A numerical study. *Physics of Fluids*, *32*(12), 123305.

[101] Schaffer, H. (1996). Second-order wavemaker theory for irregular waves. *Ocean Engineering*, *23*(1), 47–88.

[102] Schwartz, L. & Fenton, J. (1982). Strongly nonlinear waves. *Annual Rev. Fluid Mech.*, *14*(11), 39–60.

[103] Shadloo, M. S., Zainali, A., Yildiz, M., & Suleman, A. (2012). A robust weakly compressible sph method and its comparison with an incompressible sph. *International Journal for Numerical Methods in Engineering*, *89*(8), 939–956.

[104] Shao, J., Li, H., Liu, G., & Liu, M. (2012). An improved sph method for modeling liquid sloshing dynamics. *Computers & Structures*, *100*, 18–26.

[105] Shobeyri, G. & Afshar, M. (2010). Simulating free surface problems using discrete least squares meshless method. *Computers & Fluids*, *39*(3), 461–470.

[106] Simonetti, I., Cappietti, L., El Safti, H., & Oumeraci, H. (2015). Numerical modelling of fixed oscillating water column wave energy conversion devices: toward geometry hydraulic optimization. In *International Conference on Offshore Mechanics and Arctic Engineering*, volume 56574, (pp. V009T09A031). American Society of Mechanical Engineers.

[107] Simonetti, I., Cappietti, L., Elsafti, H., & Oumeraci, H. (2017). Optimization of the geometry and the turbine induced damping for fixed detached and asymmetric owc devices: A numerical study. *Energy*, *139*, 1197–1209.

[108] Simonetti, I., Cappietti, L., Elsafti, H., & Oumeraci, H. (2018). Evaluation of air compressibility effects on the performance of fixed owc wave energy converters using cfd modelling. *Renewable energy*, *119*, 741–753.

[109] Simonetti, I., Cappietti, L., & Oumeraci, H. (2018). An empirical model as a supporting tool to optimize the main design parameters of a stationary oscillating water column wave energy converter. *Applied Energy*, *231*, 1205–1215.

[110] Soleimani, K., Ketabdari, M. J., & Bingham, H. B. (2022). Wcsph simulation of the forced response of an attenuator oscillating water column wave energy converter. *European Journal of Mechanics-B/Fluids*, *95*, 38–51.

[111] Songdong, S. & Changming, J. (2006). SPH computation of plunging waves using a 2-d sub-particle scale (SPS) turbulence model. *International Journal for Numerical Methods in Fluids*, *51*, 913–936.

[112] Spinneken, J. & Swan, C. (2009). Second-order wave maker theory using force-feedback control. part i: A new theory for regular wave generation. *Ocean Engineering*, *36*, 539–548.

[113] Sun, P., M., L., Le Touzé, D., & Zhang, A. (2019). The suction effect during freak wave slamming on a fixed platform deck: Smoothed particle hydrodynamics simulation and experimental study. *Physics of Fluids*, *31*(11), 117108.

[114] Sun, P., Ming, F., & Zhang, A. (2015). Numerical simulation of interactions between free surface and rigid body using a robust sph method. *Ocean Engineering*, *98*, 32–49.

[115] Sun, W.-K., Zhang, L.-W., & Liew, K. (2020). A smoothed particle hydrodynamics–peridynamics coupling strategy for modeling fluid–structure interaction problems. *Computer Methods in Applied Mechanics and Engineering*, *371*, 113298.

[116] Tofighi, N., Ozbulut, M., Rahmat, A., Feng, J. J., & Yildiz, M. (2015). An incompressible smoothed particle hydrodynamics method for the motion of rigid bodies in fluids. *Journal of Computational Physics*, *297*, 207–220.

[117] Ursell, R., Dean, R., & Yu, Y. (1960). Forced small amplitude water waves: a comparison of theory and experiment. *Journal of Fluid Mechanics*, *7*, 32–52.

[118] van der Meer, J. & Bruce, T. (2014). New physical insights and design formulas on wave overtopping at sloping and vertical structures. *Journal of Waterway, Port, Coastal, and Ocean Engineering*, *140*(6), 04014025.

[119] Versteeg, H. K. & Malalasekera, W. (2007). *An introduction to computational fluid dynamics: the finite volume method*. Pearson education.

[120] Vicinanza, D. & Frigaard, P. (2008). Wave pressure acting on a seawave slot-cone generator. *Coastal Engineering*, *55*(6), 553–568.

[121] Victor, L. & Troch, P. (2012). Wave overtopping at smooth impermeable steep slopes with low crest freeboards. *Journal of Waterway, Port, Coastal, and Ocean Engineering*, *138*(5), 372–385.

[122] Violeau, D. & Rogers, B. D. (2016). Smoothed particle hydrodynamics (sph) for free-surface flows: past, present and future. *Journal of Hydraulic Research*, *54*(1), 1–26.

[123] Wen, H. & Ren, B. (2018). A non-reflective spectral wave maker for SPH modeling of nonlinear wave motion. *Wave Motion*, *79*, 112–128.

[124] Wen, H., Ren, B., & Yu, X. (2018). An improved sph model for turbulent hydrodynamics of a 2d oscillating water chamber. *Ocean Engineering*, *150*, 152–166.

[125] Yang, X., Liu, M., Peng, S., & Huang, C. (2016). Numerical modeling of dam-break flow impacting on flexible structures using an improved sph–ebg method. *Coastal Engineering*, *108*, 56–64.

[126] Zang, Z., Zhang, Q., Qi, Y., & Fu, X. (2018). Hydrodynamic responses and efficiency analyses of a heaving-buoy wave energy converter with pto damping in regular and irregular waves. *Renewable Energy*, *116*, 527–542.

[127] Zhang, Y. & Wan, D. (2018). Mps-fem coupled method for sloshing flows in an elastic tank. *Ocean engineering*, *152*, 416–427.

[128] Zhu, G., Graham, D., Zheng, S., Hughes, J., & Greaves, D. (2020). Hydrodynamics of onshore oscillating water column devices: A numerical study using smoothed particle hydrodynamics. *Ocean Engineering*, *218*, 108226.

[129] Zienkiewicz, O. C., Taylor, R. L., Nithiarasu, P., & Zhu, J. (1977). *The finite element method*, volume 3. McGraw-hill London.